Electron Temperature Enhancement Effects on Plasma Irregularities Associated with Charged Dust in the Earth's Mesosphere

Chen Chen

Dissertation submitted to the faculty of the Virginia Polytechnic Institute and State University in partial fulfillment of the requirements for the degree of

Doctor of Philosophy
in
Electrical Engineering

Wayne A. Scales, Chair
Gary S. Brown
Joseph J. Wang
Adrian Sandu
Mark Jones

November 26, 2007
Blacksburg, Virginia

Keywords: PMSE, Noctilucent Cloud, Dusty Plasma, Plasma Simulation

Electron Temperature Enhancement Effects on Plasma Irregularities Associated with Charged Dust in the Earth's Mesosphere

Chen Chen

(ABSTRACT)

Recently, experimental observations have shown that Polar Mesospheric Summer Echoes PMSE may be modulated by radio wave heating the irregularity source region with a ground-based ionospheric heating facilities. It is clear from these past investigations that the temporal behavior of PMSE during ionospheric heating shows promise as a diagnostic for the associated dust layer. To investigate the temporal behavior of plasma irregularities thought to produce PMSE, this work describes a new model that incorporates both finite diffusion time effects as well as dust charging. The hybrid model utilizes fluid ions described by continuity and momentum equations, electrons whose behavior is determined from quasi-neutrality, and charged dust described by the standard Particle-In-Cell PIC method. The model has been used to investigate the temporal behavior of charged dust associated electron irregularities during electron temperature enhancement associated with radio wave heating. The model predicts that the temporal behavior of the irregularities depends on the ratio of the electron-ion ambipolar diffusion time to the dust particle charging time $\tau_{\mathrm{d}}/\tau_{\mathrm{c}}$. The results indicate that typically for $\tau_{\mathrm{d}}/\tau_{\mathrm{c}} << 1$, an enhancement in electron irregularity amplitude occurs for a period after turn-off of the radio wave heating. The work also predicts that for $\tau_{\mathrm{d}}/\tau_{\mathrm{c}} >> 1$, an enhancement in electron irregularity amplitude occurs for a time period after the turn-on of the radio wave heating. Due to the dependence of τ_{d} on irregularity scale-size, these results have important implications for observations of PMSE modification at different radar frequencies. Both continuous and discrete charging model were embedded into this computational model, the results were compared and analyzed.

It is evident that significant diagnostic information may be available about the dust layer from the temporal behavior of the electron irregularities during the heating process which modifies the background electron temperature. Particularly interesting and important periods of the temporal behavior are during the turn-on and turn-off of the radio wave heating. Although a number of past theoretical and experimental investigations have considered both these on and off period, this dissertation considers further possibilities for diagnostic information available as well as the underlying physical processes. Approximate analytical models are developed and compared with a more accurate full computational model as a reference. Then, from the temporal behavior of the electron irregularities during the turn-on and turn-off of the radio wave heating, the analytical models are used to obtain possible diagnostic information for various charged dust and background plasma quantities.

Finally, two experiment campaigns have been performed at HAARP, Gakona, Alaska. Preliminary observation results look promising for the existence of PMSE turn-on overshoot. However, more careful experiments need to be done before firm conclusions can be drawn. The new designed Echotek digital receiver is ready for use now. It will be much superior to the experimental setup used for measurements in the previous campaign.Therefore, future experimental campaigns are planning next year to support the theoretical research.

I dedicate this dissertation to Mom, Dad, and Wei

Acknowledgments

Many people have inspired, guided, helped me during the four and half years I spent at Virginia Tech, and I would like to thank them all for a great graduate school experience. I first want to thank Professor Wayne A. Scales, my advisor, who not only guided my research but also served as a role model for my future research and career. I sincerely appreciate his enthusiasm and patience in guiding me during this research work. His insight, kindness, and genuine concern for his students made working with him a truly memorable experience.

The newly founded Center for Space Science and Engineering Research at Virginia Tech has been a fine research environment. Professors, Joseph J. Wang, Scott Bailey, and Robert Clauer were always willing to share their knowledge of space physics and life. I received insightful and helpful input on my research from Professors Gary Brown, Charles Bostian, and Timothy Pratt. Further thanks to Professors Adrian Sandu and Mark Jones for their time spent serving on my advisory committee.

Many thanks to Dr. Paul Bernhardt from NRL for his kind support and help. I am particularly grateful to Dr. Lars Dyrud of the CRS Inc., I had a wonderful summer with you during my internship. Grateful acknowledgement goes also to Todd Parris, Dr. Bill Bristow and Dr. Roger Smith, of GI, UAF; Kim Nielsen, Dr. Michael Taylor of USU; Dr. Ove Havnes of EISCAT, Dr. Ed. Kennedy, Dr. Keith Grove of AFRL for helping me setup my experiments at HAARP.

The students in space science and engineering group were an interesting and enjoyable group of people with whom to work and I am particularly grateful to Michael Wu, Scott Kowalchuk, Sophia Yi, Hong Xi, Dianhong Lu, Rick Wilder, Lyndell Hockersmith, Cissi Lin, Justin Carstens, thank you all for your valuable input and help with research.

I need to thank those friends who made my time at Virginia Tech so enjoyable: Paul Piccione, Liaosa Xu, Jeremy Marks, Jiang Wu, Min Liu, Jin Zhang, Ran Miao, Hang Wang, Qing Tong, Jun Zheng, Lin Dong, Bin Sheng, Zhiyuan Lin, and many others. Many thanks to my roommates Wenjie Zheng, Xiaoyan Yu, Wen Yin, Joohong Lee, Tingting Meng and Chen Zhang. Also, my cousin, Qing Chen, Yue Jiang, and life time friends Yaling Liu, Li Wen, Lu Gan, Pan Zhang, made my time here far more enjoyable. Special thanks to Virginia Tech and Virginia Tech football team, it is so proud to be a Hokie.

I owe a huge debt of gratitude to my parents for their love, support, and humor throughout not only the course of my Ph.D. studies, but throughout my entire life.

Thanks Mom and Dad.

Finally, I would like to thank my companion, fiance, and friend, Wei Jin, who encouraged, supported and cajoled me through the many ups and downs of the last three years. Her love and support is unfailing and her patience and understanding was unselfish and appreciated more than she knows.

Contents

List of Figures

List of Tables

Chapter 1

Introduction

Polar Mesospheric Summer Echoes PMSE are strong radar echoes that have been observed typically in the 50 MHz to 1.3 GHz frequency range in the summer polar mesosphere [*Ecklund and Balsley,* 1981; *Cho et al.,* 1993, 1997 and references therein]. The radar echoes are believed to be produced by Bragg scatter from electron density irregularities at half the radar wavelength. Therefore, the implied wavelengths of the irregularities from past experimental observations are roughly in the range from 10 meters down to 10 centimeters. The electron irregularities believed to produce PMSE result from the electron charging on subvisible dust that exists in the mesosphere. These particles are in the 10 nm size range and produced from ice since the 85 km altitude range of PMSE generation is the coldest in the atmosphere. It has been only relatively recently that the existence of these dust particles has been clearly established [*Havnes et al.,* 1996]. It should be noted that the larger dust particles of 50 nm size or larger are often observed below the PMSE generation region. When they are observed from the ground, they are called noctilucent clouds NLCs and when they are observed from above by spacecraft, they are considered Polar Mesospheric Clouds PMCs. From recent comprehensive numerical simulation work [*Lie-Svenson et al.,* 2003] it is believed that the charging of the mesospheric electrons onto irregular dust density leaves electron density 'fingerprints' in the form of the electron irregularities that produce PMSE.

PMSE primarily has been studied at 50 MHz. The first observations were made using the Poker Flat radar [*Ecklund and Balsley*, 1981]; many other observations followed with smaller radars. Other research groups have observed PMSE at 224 MHz [*Rottger et al.,*, 1988] and very recently at 500 MHz [*Hall and Rottger,* 2001]. Moreover, echoes have also been recorded at even the higher frequencies of 933 MHz [*Rottger et al.,* 1990] and 1290 MHz [*Cho et al.,* 1992]. However, there are few experiments that have been done at HF frequencies until very recently like at HAARP, AK at 4.9 MHz[*Kelley, et. al.*, 2002].

Recently, experiments have also shown that PMSE can be weakened artificially by radio wave heating from a ground-based ionospheric heating facilities [*Chilson et al.,* 2000, *Belova et al.*, 2001; 2003]. This weakening of PMSE has been observed at 224 MHz with the EISCAT facility in Tromso, Norway. Therefore, the wavelength of the irregularities investigated were about 0.67 meters. These observations indicated disappearance of PMSE within a second or so after the radio wave heating is turned on. The PMSE typically reappeared to approximately the initial value in a similar time-scale when the heating is turned off [*Belova et al.,* 2003]. Such modulation may allow PMSE to become an even more powerful remote sensing diagnostic for the mesosphere. [*Dimant and Milikh,* 2004].

Also, in more recent work [*Havnes et al.,* 2003; *Havnes,* 2004], it was observed that when the artificial electron heating is turned off, the increase in electron gradients in the dusty plasma and also the value of dust charge density to electron density, will lead to a stronger PMSE, described as 'PMSE overshoot'. This work adopted the Time-Dependent Dust Cloud Charge Model [*Havnes et al.,* 1984; 1990] which uses Boltzmann electron and ion physics. Also, quasi-neutrality and standard orbit-limited motion OLM equations are applied to describe the dust particle charging. The electrostatic potential and dust floating potential are obtained from the model and plasma and dust charge densities may be derived. This model successfully predicts the overshoot effect during turn-off of radio wave heating in experiments and was the first major step in utilizing PMSE modification as a diagnostic tool. It is important to note, however, that the Boltzmann electron and ion approximation neglects finite diffusion time effects, which will bring limitations for both lower radar frequencies as well as larger dust sizes. The original model also neglected reduction in plasma density due to dust charging. This brings limitations for higher dust densities as well as the larger dust sizes. Therefore a new model is needed for further detailed study of the temporal evolution of PMSE during radio wave heating. It has been noted in early modelling work [*Rapp and Lubken,* 2003;*Dimant and Milikh,* 2004] that both the effects of dust charging and diffusion are expected to play crucial roles in PMSE modulation during radio wave heating. Therefore, new theory could be proposed based on this model.

Also, an approximate analytical models should also be considered so that it may shed light on the physical processes during the initial perturbation of the irregularities. In addition, more careful experiments should be performed in order to verify the theocratical predictions.

It is clear from past work that the temporal evolution during the initial perturbation of mesospheric dust associated electron irregularities has been exploited to the fullest. Potential exists for diagnostics of the dust layer and interpretation of physical processes associated with PSMEs which are considered a forefront issue in upper atmospheric space science. In this dissertation, both computational and analytical models are developed that may shed light on the physical processes during the initial perturbation of the irregularities. These may lead to diagnostic capabilities. Furthermore, two first ever experiment campaigns were performed in the passing two summers. The observations were analyzed to verify the result followed the theocratical and computational results. The dissertation is organized as follows. The next chapter list the background knowledge for this study. And then chapter 3 describes the computational model used to investigate the enhanced electron temperature effects on the irregularities. Results obtained with the model are discussed as well. Emphasis is placed on interpreting the relative importance of diffusion and charging effects on the reduction and recovery of the electron irregularities. Chapter 4 introduced the analytical model to emphasis on the initial perturbation of irregularities. The analytical models are used to obtain possible diagnostic information for various charged dust and background plasma quantities. Experimental observations were described next in Chapter 5. The experiment system setup is covered. Two experimental campaigns were discussed as well. In the last chapter, conclusions and future works were drawn at the end.

Chapter 2

Background

2.1 The Structure of the Neutral Atmosphere and the Ionosphere

The earth is surrounded by a blanket of air, which we call the atmosphere. It reaches over 560 kilometers (348 miles) from the surface of the earth, so we are only able to see what occurs fairly close to the ground. Early attempts at studying the nature of the atmosphere used clues from the weather, the beautiful multi-colored sunsets and sunrises, and the twinkling of stars. With the use of sensitive instruments from space, we are able to get a better view of the functioning of our atmosphere.

There are several ways to classify the earth's atmosphere. Based on the thermal characteristics (temperature changes), four distinct layers have been identified:

The troposphere starts at the earth's surface and extends 8 to 14.5 kilometers high (5 to 9 miles). This part of the atmosphere is the most dense. As you climb higher in this layer, the temperature drops from about 17 to -52 degrees Celsius. Almost all weather is in this region. The tropopause separates the troposphere from the next layer. The tropopause and the troposphere are known as the lower atmosphere.

The stratosphere starts just above the troposphere and extends to 50 kilometers (31 miles) high. Compared to the troposphere, this part of the atmosphere is dry and less dense. The temperature in this region increases gradually to -3 degrees Celsius, due to the absorbtion of ultraviolet radiation. The ozone layer, which absorbs and scatters the solar ultraviolet radiation, is in this layer. Ninety-nine percent of ”air” is located in the troposphere and stratosphere. The stratopause separates the stratosphere from the next layer.

Mesosphere The mesosphere starts just above the stratosphere and extends to 85 kilometers (53 miles) high. In this region, the temperatures again fall as low as -93 degrees Celsius as you increase in altitude. The chemicals are in an excited state, as they absorb energy from the sun. The mesopause separates the mesosphere from the thermosphere.

The regions of the stratosphere and the mesosphere, along with the stratopause and mesopause, are called the middle atmosphere by scientists.

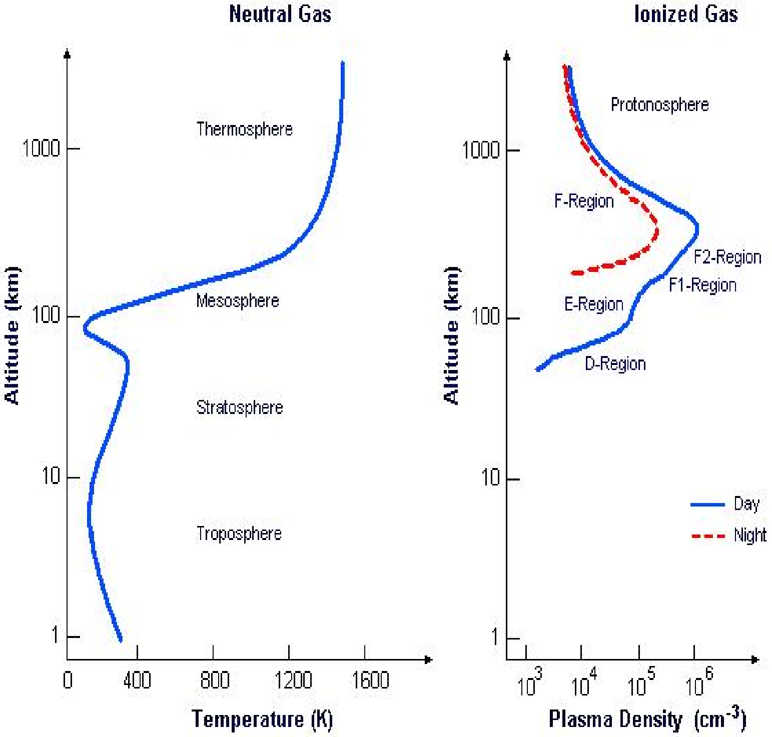

Figure 2.1: Typical profiles of neutral atmospheric temperature with the various layers designated, and ionospheric plasma density for both Day time and night time. ([*Kelley,* 1989], Copyright Elsevier) [1]

The thermosphere starts just above the mesosphere and extends to 600 kilometers (372 miles) high. The temperatures go up as you increase in altitude due to the sun's energy. Temperatures in this region can go as high as 1,727 degrees Celsius. Chemical reactions occur much faster here than on the surface of the earth. This layer is known

---

[1] This article was published in *The earth's ionosphere*, Vol 43, M.C.Kelley, Page 5-6, *International Geophysics Series* Copyright Elsevier (1989).

as the upper atmosphere.

Besides the identification of earth's atmosphere structure by the temperature behavior, it could also be defined by the number of free electrons and other charged particles. Based on this classification, the atmosphere is divided into three layers, ionosphere, plasma sphere, and magnetosphere. For the work we are working on, we focus on the ionosphere.

The discovery of the earth's ionosphere has an interesting history. It came from the observation of reflected radio waves, whose properties could only be explained by the presence of a reflecting layer in the earth's atmosphere composed of electrons and positive ions. The earth's ionosphere is divided into several regions designated by the letters D,E, and F (see Figure 2.1). F region is then subdivided into F1 and F2. Historically, the division arose from the successive plateaus of electron density (N_e) observed on records of the time delay (i.e., virtual height) of radio reflections as the transmitted signal was swept through frequency. (The critical frequency at which reflection occurs varies as Ne vary. Thus higher frequencies penetrate farther into the ionosphere and are reflected by higher Ne. The E "layer" was the first to be detected and was so labelled as being the atmospheric layer reflecting the E vector of the radio signal. Later the lower D and higher F layers were discovered. Distinct ionospheric regions develop because (a) the solar spectrum deposits its energy at various heights depending on the absorption characteristics of the atmosphere, (b) the physics of recombination depends on the density, and (c) the composition of the atmosphere changes with height. Thus the four main ionospheric regions can be associated with different governing physical processes, and this physics (rather than simple height differentiation) is the basis for labelling an ionospheric region on another planet as a D, E, F1, or F2 region.

The ionosphere, being a plasma and a conducting medium, both propagates and reflects radio waves, depending on their frequencies; thus, allowing for long distance radio communication.

The E and F layers are the most important layers for radio communications in the frequency range of 3 to 30 MHz. Electromagnetic waves with a frequency above 40 MHz is able to penetrate through the ionosphere. In the D region, only waves of 2 MHz and below are reflected. This is because the D region has a much lower electron density than the other layers. The D region also has a much larger collision frequency, due to a high neutral density.

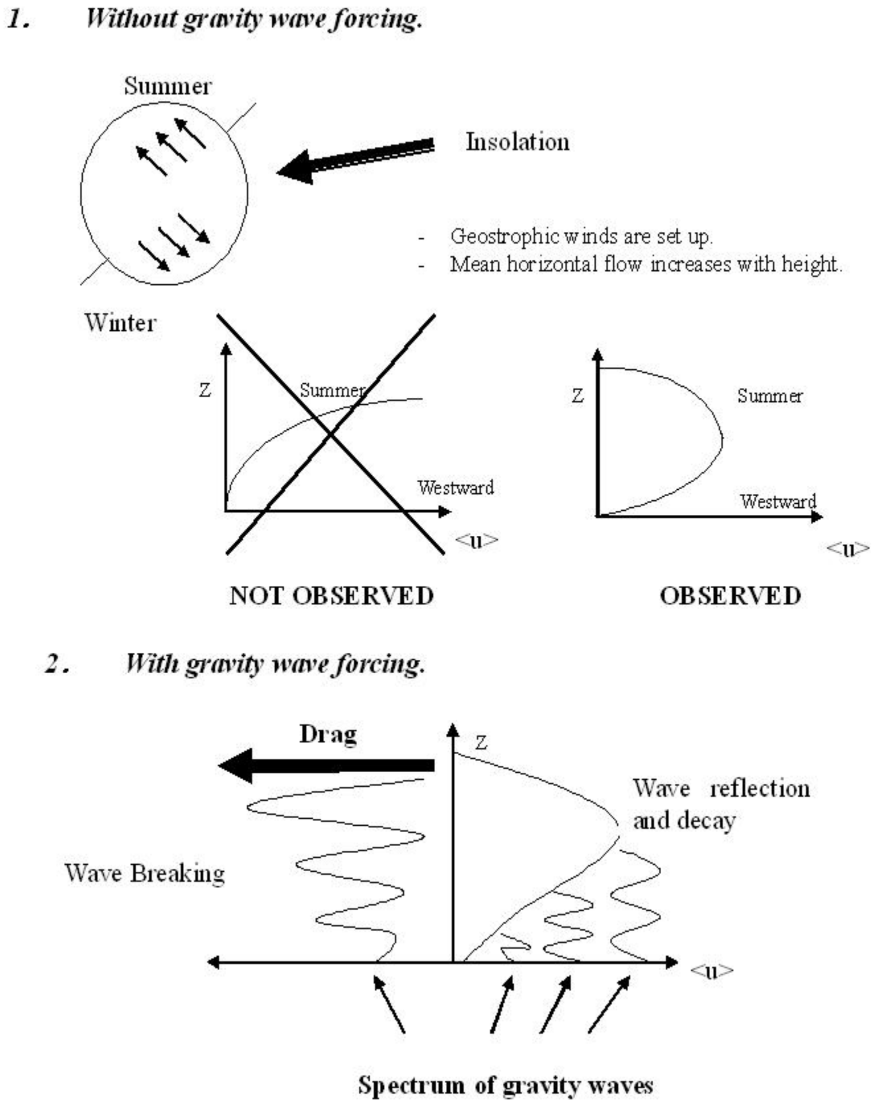

Figure 2.2: An illustration of the relationship between gravity waves and the temperature profile in summer polar mesosphere

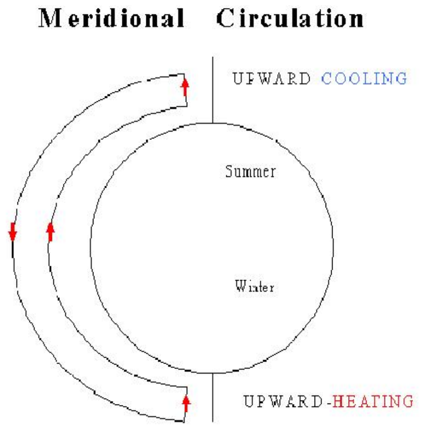

Figure 2.3: A diagram showing atmosphere circulation

2.2 The Earth's Mesosphere

The mesosphere (literally middle sphere) is the third highest layer in our atmosphere, occupying the region 50 km to 80 km above the surface of the earth, above the troposphere and stratosphere, and below the thermosphere. It is separated from the stratosphere by the stratopause and from the thermosphere by the mesopause.

Temperatures in the mesosphere drop with increasing altitude to about -100 C. The mesosphere is the coldest of the atmospheric layers. In fact it is colder then Antarctica's lowest recorded temperature. It is cold enough to freeze water vapor into ice clouds. You can see these clouds if sunlight hits them after sunset. They are called Noctilucent Clouds (NLC). NLCs are most readily visible when the sun is from 4 to 16 degrees below the horizon.

The mesosphere is also the layer in which a lot of meteors burn up while entering the earth's atmosphere. From the earth they are seen as shooting stars.

The reason the mesosphere is so cold can be explained as follows. From the temperature variation with atmosphere structure in Figure 2.1, Stratosphere warmed because of ozone layer. Thermosphere warmed by atoms being accelerated by sunlight. Mesosphere is sandwiched between two warmer layers. The mesosphere region connects geospace - where the atmospheres of the sun and earth converge to the lower atmosphere. This is a complex region of opposites where great surges of energy meet, carried downward by particles energized by the solar wind which create dramatic auroral displays, and upward from the troposphere and stratosphere by atmospheric tides and waves, creating the earth's coldest environment at 85 km altitude in the mesopause.

This work is studying about the summer polar mesosphere. Therefore, besides knowing that mesosphere is surprisingly coldest in all year around, we need to explore deeper about the summer polar mesosphere region. There are two main issues need to be considered, first is the behavior of summer mesosphere comparing with other seasons; second is the polar mesosphere behavior in the summer time comparing with other locations.

The summer mesosphere is a very cold place for the ice cloud to form. The reason has been developed by [*Lindzen, 1981*], and modelled by [*Holton,* 1983], the attenuation of vertically propagating gravity waves (or buoyancy waves; these are not the waves of gravity field the astronomers are trying to discover). These waves are mainly caused by jet streams, thunder clouds and mountains. Vertically propagating waves transfer a lot of momentum from the lower atmosphere upwards. The transfer of momentum takes place when waves attenuate; this can happen by radiative cooling or convective overturning (if waves are unstable). It turns out that gravity waves are the only waves that can propagate upwards to the summer mesosphere, and not even all kinds of gravity waves but only those that have strong east-moving phase velocity. As they propagate higher their amplitude increases, until they eventually become statically unstable and break up, transferring their eastward momentum to the mean flow. In the atmosphere, winds and temperature gradients are interconnected; thus the introduction of momentum also changes the local temperature field.

Figure 2.2 shows the relationship between gravity wave and the temperature behavior in summer polar mesosphere. This mechanism cools the summer polar mesopause so strongly that the region is actually the coldest place in Earth's atmosphere, with temperatures typically around 130 K; about 60 K lower than in the winter polar mesopause where the solar heating is absent.

This extraordinary temperature distribution can be explained by strong vertical motions, driven by the attenuation of vertically propagating gravity waves. The input of momentum in the summer polar mesosphere decreases the westward flow that should occur if the mesosphere were in radiative balance and turns it eastward. Accordingly, the coriolis effect turns the flow toward the equator, forcing a strong upward motion and associated adiabatic cooling in the summer hemisphere polar mesosphere, and compensating downward motion and adiabatic heating in winter-side polar mesosphere.

Figure 2.3 describes the atmospherical circulation. This circulation depends also on stratospheric conditions, as they largely determine the kind of vertically propagating waves that reach the mesosphere. Thus, changes in stratospheric winds, for example due to changes in uv-absorption, can significantly change the conditions in the mesosphere also. This middle-atmosphere circulation system is quite complex, depending on radiation, chemistry and fluid dynamics, and full of feedback mechanisms that make the whole system strongly nonlinear.

In addition to providing the the low temperature, vertically propagating gravity waves also provide the continuous supply of water vapor from the stratosphere with the forced upward motion. Thus, the gravity waves are essential for the noctilucent cloud formation. They also give the clouds their usual shapes.

There is also another water vapor source with approximately equal importance with the transport, namely the photo dissociation of methane in the mesosphere. This process produces water vapor for noctilucent cloud formation, it doesn't have to be transported to the place of formation. This is an advantage, as water vapor is also photo dissociated above 65 km altitude. In the mesopause, the average lifetime of a water molecule is only 3-10 days.

2.3 Noctilucent Clouds

From the above section, we know the mesopause is very cold and also moist. These two are essential for the formation of Noctilucent Clouds in the polar summer mesosphere.

Noctilucent Clouds (NLC) are thin clouds which are formed the mesopause (about 83 km). They are seen from the ground when the sun is just below the horizon, they are then lit from underneath and the light reflected at a low angle picks out the many waves which cross the cloud layer. NLC appear as a thin but distinct cloud layer well above the visible part of the atmosphere. They appear to be about twice the distance from the horizon than the visible thickness of the atmosphere. To the eye, they look like a thin shell of glowing wisps suspended above our atmosphere in the blackness of space. The NLC picture could be easily found from internet.

In the past 30 years, there has been a steady increase in the occurrence of noctilucent clouds (NLC). Since 120 years ago no evidence of this phenomenon existed. The rise may be due to lower temperatures and more moisture created through increased carbon dioxide and methane in lower altitudes. Noctilucent clouds could prove very sensitive indicators of human activity on earth and in space.

The conditions of mesopause are suitable for ice particle formation and growth only during summer months, both for the temperature and the humidity, as only the summer stratosphere allows the right kind of vertical waves to propagate to the mesosphere and provide the necessary influx of eastward momentum. During winter the zonal winds in the stratosphere have the opposite direction, so the eastward propagating waves cannot propagate to the mesosphere. The upward motions associated with the influx of eastward momentum near the mesopause only occur at high latitudes of summer hemisphere, confining the formation of clouds there. From the pole-side, the latitude region of ground observations is limited by sun-elevation angle too high during the summer months, but satellites have frequently observed clouds covering the whole polar region (these clouds are called polar mesospheric clouds and NLC's are considered only their ragged edges). The sufficient conditions (low temperature and high humidity) are only reached in a shallow layer in the mesopause, so the vertical extent of the clouds is always small. The altitude of the mesopause varies little, and so does the altitude of NLC's. Thus, the ice theory is very successful in explaining the noctilucent cloud observations.

2.4 Polar Mesosphere Summer Echoes

Polar Mesosphere Summer Echoes (PMSE) are the very strong radar echoes appearing in the summer polar mesosphere between about May and August. Figure 5.4 and 5.6 shows how the echoes look like. They are most persistent in June and July and more sporadic in May and August. They are caused by highly structured plasma density fluctuations concentrated in thin layers, sometimes, but not always, together with corresponding structure in the neutral density. It is not known how the plasma structuring is produced - breaking of gravity waves propagating up from below and aerosols, such as sub-visual cloud particles, are most likely be involved.

Polar Mesosphere Summer Echoes (PMSE) occurs about the same season as the Noctilucent Clouds. Noctilucent clouds seem to be increasing in occurrence (Gadsden, 1990) and some scientists believe this may be due to increased greenhouse gases in the atmosphere. The clouds also show an 11-year variation roughly opposite in phase to the sun's activity cycle, for example, they are less often seen at solar maximum. It is not yet known how closely PMSE are related to noctilucent clouds (sometimes they have been seen together, sometimes not) , nor whether PMSE also vary with the solar cycle nor whether they are increasing on a longer time scale.

These PMSE are not caused by the conventional incoherent or turbulence scatter process, but by some irregularity structure in the electron density profile, which may be related to steep electron density gradients, heavy positive ions, dressed aerosols, gravity waves and turbulence or other yet unknown mechanisms. These echoes frequently exhibit dramatic height and intensity variations as well as large variations in Doppler shift, i.e. vertical velocity. Some of the morphology of Polar Mesosphere Summer Echoes (observed also on other radar frequencies between 2 MHz and 1300 MHz) is quite similar to that of Noctilucent Clouds.

Polar Mesosphere Summer Echoes have been studied for over 25 years beginning with the pioneering work described by [*Ecklund and Balsley*,1981]. These researchers published two consecutive years of 50-MHz radar data, i.e. 1979-1980, taken at the Poker Flat Research Range in Alaska. The surprising result was that with their relatively modest sized radar they detected remarkably strong echoes centered near 85 km during the summer. At other times of the year sporadic and weaker mesospheric echoes were detected but only below 80 km. Since that time numerous radar studies have taken place, mostly at frequencies at or above the 50 MHz used by Ecklund and Balsley. Mesospheric echoes have been reported at 224 MHz [*Rottger et al.,* 1988], 500 MHz [*Hall and Rottger,* 2001], 933 MHz [*Rottger et al.,* 1990], and 1290 MHz [*Cho et al.,* 1992]. Strong radar echoes in the VHF and UHF frequency bands are unexpected since the corresponding Bragg wavelengths are deep within the viscous subrange of the neutral turbulence. This turbulence leads to variations in the index of refraction which in turn are responsible for atmospheric echoes.

Below the mesosphere the index of refraction is controlled by the pressure and temperature of the atmosphere. In the mesosphere the atmospheric medium is so tenuous that variations in pressure and temperature are insufficient to lead to radar echoes. However, during the day the increase in electron density in the D-region of the ionosphere, which is collocated with the mesosphere, can lead to detectable echoes at all seasons for large VHF radars such as the Jicamarca radar in Peru and the MU (Middle and Upper atmosphere) radar in Japan. These electrons behave as a passive scalar mixed by the neutral turbulence. Simultaneous radar and rocket data taken in Peru showed a quantitative agreement between the observed spectrum of electron fluctuations in the mesosphere and the Jicamarca 50-MHz echoes [*Royrvik and Smith,* 1984]. Their data clearly show that the electron fluctuation spectrum has an inner scale determined by the Kolmogorov microscale of neutral turbulence and displays a break to a k.7 spectral form at 40 m, as expected for the mesosphere [*Hocking,* 1987]. Similar radar and rocket concurrent observations in the polar summer showed that the electron fluctuation spectrum extends to much smaller scales than does the neutral turbulence [*Ulwick et al.,* 1988; *Kelley and Ulwick*, 1988]. This has been explained as a reduction of the electron diffusion coefficient due to massive charged ice particles associated with Noctilucent Clouds (NLC) and a corresponding increase in the Schmidt number (Kelley et al., 1987; Cho and Kelley, 1993). The latter is defined as the ratio of the atmospheric viscosity coefficient to the electron diffusion coefficient, i.e. $S_c = \mu/v$. For a high Schmidt number [*Batchelor* 1959] has shown that the spectrum of a passive scalar such as the electrons will extend beyond the inner scale of turbulence. In addition to the interesting radio physics, the strong scattering cross section of PMSE provides a mechanism for remote sensing of NLC without the need for special lighting conditions. Cho and Kelley [1993] predicted volume scattering cross section (η) as a function of radar Bragg wavenumber (k) for mesospheric conditions and several Schmidt numbers. Such calculation shows that η increases as

$\lambda^{11/3}$, where λ is the radar operating wavelength, which in turn suggests that radars operating at frequencies less than VHF would have correspondingly stronger echoes.

2.5 Ground-Based Ionospheric Heating Facilities

Mesopause is one of the most difficult locations in Earth's atmosphere to observe. Satellites, lidars, and radars, for example, can be used to do remote sensing measurements, but *In situ* measurements can only be carried out using expensive rockets. Remote sensing methods cannot provide direct measurements, and a rocket provide data with very limited spatial or temporal resolution (they penetrate the thin NLC layer with high speed in a few seconds, and only in two highly localized points, once on their way up and once on their way down).

As mesopause is inside the ionosphere, the radar is used for the observation, and the ground based heating facilities are used at the same time to stimulate the atmosphere for the more obvious physical reactions. Also, because of the nonlinear relationship between ionospheric conductivities and electron temperature, the high power HF source can produce modification of the ionospheric conductivities and consequently of the dynamo current system. These modifications are very helpful for the study in ionosphere. In this case, this work simulate radar backscatter observations associated with the ground-based heating facilities. Figure 2.7 shows the HAARP (HF Active Auroral Research Program)ground-based ionospheric heating facilities in Gakona, Alaska, US. HAARP now is the main research site for the ionospheric study in US.

The HAARP heating transmitter as shown in figure 2.4 is what is known as a phased array transmitter. It is designed to transmit a narrow beam of high power radio signals in the 2.8 to 10 MHz frequency range. There are to be 180 towers, 72' in height mounted on thermopiles spaced 80' apart in a 12 x 15 rectangular grid, each of which supports near its top, two pairs of crossed dipole antennas, one for the low band (2.8 to 8.3 MHz), the other for the high band (7 to 10 MHz). The antenna system is surrounded by an exclusion fence to prevent possible damage to the antenna towers or harm to large animals. An elevated ground screen, attached to the towers at the 15' level, acts as a reflector for the antenna array while allowing vehicular access underneath to 30 environmentally-controlled transmitter shelters spaced throughout the array. Each shelter will contain 6 pairs of 10 kW transmitters, for a total of 6 x 30 x 2 x 10 kW = 3600 kW available for transmission. The transmitters can be switched to drive either the low or high band antennas.

During active ionospheric research, the signal generated by the transmitter system is delivered to the antenna array, transmitted in an upward direction, and is partially

Figure 2.4: The High Frequency Transmitter and Antenna Array in HAARP, Gakona, AK

absorbed, at an altitude between 100 to 350 km (depending on operating frequency), in a small volume a few hundred meters thick and a few tens of kilometers in diameter over the site. The intensity of the HF signal in the ionosphere is less than 3 microwatts per cm2, tens of thousands of times less than the Sun's natural electromagnetic radiation reaching the earth and hundreds of times less than even the normal random variations in intensity of the Sun's natural ultraviolet (UV) energy which creates the ionosphere. The small effects that are produced, however, can be observed with the sensitive scientific instruments installed at the HAARP facility and these observations can provide new information about the dynamics of plasmas and new insight into the processes of solar-terrestrial interactions.

Ionospheric research facilities have been in continuous use since the 1950's to investigate fundamental physical principles which govern the earth's ionosphere, so that present and future transmission technologies may take into account the complexities of the ionosphere. At the present time the US operates two another ionospheric research sites besides HAARP, one in Puerto Rico, near the Arecibo Observatory, and the other (known as HIPAS) in Alaska near Fairbanks. Both of them employ active and passive radio instrumentation similar to that being built at HAARP. Interest in the ionosphere is not limited to the US: a five-country consortium operates the European Incoherent Scatter Radar site (EISCAT), a premier world-class ionospheric research facility located in northern Norway near Tromso. Facilities also are located at Jicamarca, Peru; near Moscow, Nizhny Novgorod (”SURA”) and Apatity, Russia; near Kharkov, Ukraine and in Dushanbe, Tadzhikistan. All of these installations have as their primary purpose the study of the ionosphere, and most employ the capability of stimulating to a varying degree small, localized regions of the ionosphere in order to study methodically, and in a detailed manner what nature produces randomly and regularly on a much larger scale.

2.6 PMSE Observations Associated with Ground-Based Ionospheric Heating Facilities

It has recently been discovered that the radar phenomenon PMSE (Polar Mesospheric Summer Echoes, [*Cho and Rottger,* 1997]), which occur in the summer mesosphere between about 80 and 90 km, can be weakened if it is affected by artificial electron heating. This weakening of PMSE has been observed with the EISCAT VHF radar at 224 MHz [*Chilson et al.,* 2000; *Belova et al.,* 2003], and the EISCAT UHF radar at 933 MHz [*La Hoz et al.,* 2003]. The EISCAT heating facilities [*Rietveld et al.,* 1993] used in these experiments was run in equal and short on and off intervals (from 10 to 20 sec) and it was found in many cases, but not all, that the PMSE strength was rapidly weakened when the heater was turned on, and that it also returned rapidly [*Belova et al.,* 2003] to approximately the pre-heater value when the heater was turned off again.

The experiment demonstrated ionospheric heating could influence the VHF radar back scatter associated with PMSE. Artificially increase electron temperature within the PMSE layer will reduce the echo power. And it could be predicted that the reduction of PMSE power is related to an enhancement of the electron diffusivity during the heating.

As this weakening of PMSE was observed at 224 MHz, the wavelength of the irregularities investigated were about 0.67 meters. These observations indicated disappearance of PMSE within a second or so after the radio wave heating is turned on. The PMSE typically reappeared to approximately the initial value in a similar time-scale when the heating is turned off [*Belova et al.,* 2003]. Such modulation may allow PMSE to become an even more powerful remote sensing diagnostic for the mesosphere. It is clear that the behavior of PMSE with radio wave heating may be used as a diagnostic for plasma parameters but also new possibilities exist diagnosing mesospheric dust parameters [*Dimant and Milikh,* 2004].

2.7 PMSE Overshoot Effect Associated with Ionospheric Heating Experiments

The recent experiments and theory studies [*Havnes et al.* 2003,2004]find, the PMSE can be affected by artificial electron heating. Besides this, if the heater is run in a cycle with equal, and comparatively short off and on periods, the PMSE strength is observed to weaken when the heater is on, and recover to approximately the same strength when the heater is switched off [*Chilson, Belova, et al.* 2000]. First artificially induced modulation of PMSE using the EISCAT heating facilities. Also, the physical analysis were given also for this experiment[*Havnes et al.,* 2003, 2004].

[*Rapp and Lubken,* 2000] showed that a strongly increased electron temperature will lead to a rapid change of the electron density structure within a dust cloud. The electron density profile will be flattened out and the electron density gradients will subsequently become very much smaller than before. This decrease in the electron density gradient will lead to a decrease in PMSE power. As the heater is turned off, the electron temperature returns to the lower pre-heater value, the charged dust will quickly force electrons out of the dust cloud to form an electron depletion within the cloud again. [*Havnes et al.* 2004] predicted that by modifying the heater cycling one could extract a substantial amount of information from the time sequence of the PMSE signal. The prediction was that one should be able to obtain a characteristic curve in the PMSE time sequence with a reduction of the PMSE signal when the heater is turned on, some recovery of the signal during the heater-on period and an "overshoot" after the heater is switched off again. After that relaxation to the undisturbed value should take place. This was looked for and found in a campaign with the EISCAT radars and heating facilities in Tromoso, Norway during the summer of 2003 and 2004. The experiment results are shown in the following figure 2.8 and figure 2.9.

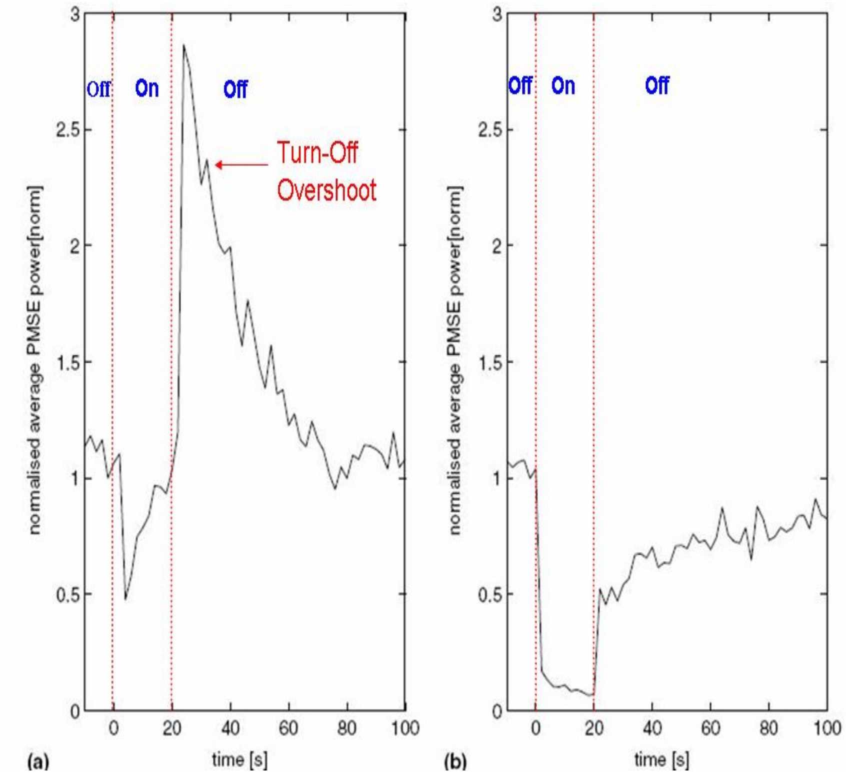

Figure 2.5: Two experimental Overshoot Characteristic Curves from summer 2004. The curves have been obtained by averaging the PMSE backscatter power over 1 h of measurement. Case (a), year 04 month 7 day 12 h 9, height range 84-84,3 km: Common case of the overshoot effect Case (b), year 04 month 7 day 5 h 10, height range 85,5-85,8 km: A variation of the overshoot effect. ([*Biebricher, et al.,* 2005], Copyright Elsevier)[2]

Figure 2.5 shows observational examples of the overshoot effect. For the overshoot to be clearly observable, a long relaxation time after the heater is switched off is necessary to get the dust charges back to those of dust unaffected by the heated electrons

---

[2] Copy Right Granted by ELsevier: Reprinted from *Advances in Space Research*, Volume 38, Issue 11, Biebricher A., Havnes O., Hartquist T.W. and LaHoz C., *On the influence of plasma absorption by dust on the PMSE overshoot effect*, Pages 2541-2550 Copyright (2006), with permission from Elsevier.

or, to bring unaffected PMSE dusty plasma into the radar beams by horizontal wind transport. The overshoot characteristic curve (OCC) contain a substantial amount of information on the conditions during PMSE and must lead to new possibilities in the study of PMSE and the conditions close to the summer mesopause.

A theoretical model was also developed to explain the physics of this Overshoot effect. [*Havnes et al., 1984, 1990*]. It adopted the Time-Dependent Dust Cloud Charge Model which uses Boltzmann electron and ion physics.

$$n_\alpha = n_{\alpha 0} \exp(-e\phi/kT_\alpha), \alpha = i, e. \tag{2.1}$$

Here $n_{\alpha 0}$ is equilibrium density of ions (i) or electrons (e), ϕ is the electrostatic potential, T_α is the temperature of ions (i) or electrons (e), while k is the Boltzmann constant. Quasi-neutrality is used in this model:

$$n_i = n_e + Z_d n_d \tag{2.2}$$

The dust particle charging calculation is done by the following way:

$$dZ_d/dt = (I_e + I_i)/e \tag{2.3}$$

Here, standard orbit-limited motion OLM equations are applied:

$$I_{\mathrm{e}} = -\pi r_{\mathrm{d}}^2 q_{\mathrm{e}} n_{\mathrm{e}} v_{\mathrm{te}} \exp(-q_{\mathrm{e}}\phi_{\mathrm{d}}/KT_{\mathrm{e}}), \tag{2.4}$$

$$I_{\mathrm{i}} = -\pi r_{\mathrm{d}}^2 q_{\mathrm{i}} n_{\mathrm{i}} v_{\mathrm{ti}} (1 - q_{\mathrm{i}}\phi_{\mathrm{d}}/KT_{\mathrm{i}}), \tag{2.5}$$

The electron charge number Z_{d} is defined as:

$$Z_{\mathrm{d}} = 4\pi\varepsilon_0 r_{\mathrm{d}} \phi_d / q_e, \tag{2.6}$$

Here the two unknowns ϕ, which is the electrostatic potential; and ϕ_d, which is the dust floating potential could be obtained from the above model.

This model successfully predicts the overshoot effect during turn-off of radio wave heating in experiments and was the first major step in utilizing PMSE modification as a diagnostic tool. It is important to note, however, that the Boltzmann electron and ion approximation neglects finite diffusion time effects, which will bring limitations for both lower radar frequencies as well as larger dust sizes. The original model also neglected reduction in plasma density due to dust charging. This brings limitations for higher dust densities as well as the larger dust sizes. Therefore a new model is needed for further detailed study of the temporal evolution of PMSE during radio wave heating. It has been noted in early modeling work [*Rapp and Lubken,* 2003;*Dimant and Milikh,* 2004] that both the effects of dust charging and diffusion are expected to play crucial roles in PMSE modulation during radio wave heating.

One of the major objective of this work is to consider a new time dependent model to investigate the temporal evolution of electron irregularities believed to produce PMSE during radio wave heating.

2.8 Conclusion

Noctilucent Clouds were first observed in 1880s. Over the past more than one hundred years, it has been explored and become a popular research topic in the recent years due to its relationship to the global change. Polar mesosphere summer echoes was first found at 1984, it has received intense experimental and theoretical investigation for more than two decades. Recent experiments show that PMSE can be weakened artificially by radio-wave heating form a ground-based ionospheric heating facility. This weakening of PMSE has been observed at 224MHz with the EISCAT facility in Tromso, Norway. Therefore the wavelength of the irregularities investigated were about 0.67m. These observations indicated disappearance of PMSE within a second or so after the radio wave heating is turned on. The PMSE typically reappeared to approximately the initial value in a similar timescale when the heating is turned off.

Also, in more recent work, it was observed that when the artificial electron heating is turned off, the increase in electron gradients in the dusty plasma and also the value of dust charge density to electron density, will lead to a stronger PMSE, described as ”PSME overshoot”. However, this work adopted Boltzmann electrons and ions approximation, which neglects finite diffusion time effects. This will bring limitations for higher dust densities as well as the larger dust sizes. Also, it has been noted in early modelling work that both the effects of dust charging and diffusion are expected to play crucial roles in PMSE modulation during radio wave heating. Therefore a new model is needed for further detailed study of the temporal evolution of PMSE during radio wave heating.

The objective of this work is to consider a new time-dependent model to investigate the temporal evolution of electron irregularities belied to produce PMSE during radio wave heating. Analytical model and experimental observation studies will be provided in the later chapters as well.

Chapter 3

Computational Model

As stated in the previous chapters, the PMSE overshoot during turn-off has been successfully predicted by the Time Dependent Dust Cloud Charging Model [*Havnes et al.*, 2003; 2004]. However, incorporation of Boltzmann electrons and ions in this model neglects finite diffusion time effects. The model presently described relaxes this assumption. It is shown that the relative importance of charging to diffusion effects may vary greatly depending on parameter regime. The relative importance of these two physical effects may cause fundamentally different behavior in PMSE temporal evolution during radio wave heating.

3.1 Mesospheric Irregularity Model

A one-dimensional hybrid model is used to study the effects of ionospheric heating by radio waves on plasma irregularities associated with charged mesospheric dust clouds. The model includes electrons, ions and dust. The evolution for times much less than the dust diffusion time is considered presently although the model is not restricted to this time-scale. Therefore, in the results to be presented, the dust can be considered to be immobile. Future investigations will consider applications in which dust motion is important. It should be noted that the model described here is essentially an extension of the model of [*Hill,* 1978] which has been used by other investigators in studying irregularities associated with PMSE. In the case here, chemistry and charging processes as well as diffusion have been included which have not been used extensively until very recently [*Lie-Svenson et al.,* 2003]. Preliminary results using the present model have been reported on elsewhere [*Scales*, 2004]. The spatial dimension is considered to be altitude in the model. For the polar mesosphere region, the geomagnetic field is near vertical and, therefore, nearly aligned with the spatial dimension. It is assumed that the component of the irregularities across the geomagnetic field in such a configuration is small. Therefore, as an approximation, magnetic field effects on the temporal evolution of the irregularities during heating are neglected here.

The ions in the model are described by plasma fluid equations. The ion density is described by the continuity equation

$$\frac{\partial n_{\mathrm{i}}}{\partial t}+\frac{\partial}{\partial x}(n_{\mathrm{i}}v_{\mathrm{i}})=P_{\mathrm{i}}+L_{\mathrm{i}}+\frac{\mathrm{d}n_{\mathrm{i}}}{\mathrm{dt}}|_{\mathrm{charging}}. \tag{3.1}$$

Here P_{i} denotes the production of ions by photoionization and L_{i} denotes the ion loss due to dissociative recombination. This loss term is described by $L_{\mathrm{i}}=\alpha n_{\mathrm{e}}n_{\mathrm{i}}$ where α is the recombination coefficient and n_{e} is the electron density. The term $\mathrm{dn_i/dt}|_{\mathrm{charging}}$ denotes the ion loss due to the ion flux onto the dust. Neglecting inertial effects, the ion velocity is given by the momentum equation as

$$v_{\mathrm{i}}=\frac{1}{\nu_{\mathrm{in}}}\left(\frac{q_{\mathrm{i}}}{m_{\mathrm{i}}}E-\frac{KT_{\mathrm{i}}}{m_{\mathrm{i}}}\frac{\partial}{\partial x}(\log(n_{\mathrm{i}}))\right) \tag{3.2}$$

where q_{i}, m_{i} and T_{i} are the ion charge, mass and temperature, and ν_{in} is the ion-neutral collision frequency. Also, K is Boltzmann's constant. The electrostatic field is denoted by E.

The dust is modelled with the standard Particle-In-Cell PIC method [*Birdsall and Langdon,* 1991]. Each dust particle is taken to have time-varying charge $Q_{\mathrm{d}}(t)$. A distribution of dust masses (or equivalently dust radii) is also allowed. The dust charge is determined from the standard continuous charging model [e.g. *Shukla and Mamun,* 2002] which is given by

$$\frac{dQ_{\mathrm{d}}}{dt}=I_{\mathrm{e}}+I_{\mathrm{i}}+I_{\mathrm{p}} \tag{3.3}$$

where I_{e} and I_{i} are the currents onto each individual dust particle by electron and ion flux and I_{p} is the photoemission current. For negatively charged dust, which will primarily be considered, these currents are given by

$$I_{\mathrm{e}}=\sqrt{8\pi}r_{\mathrm{d}}^2q_{\mathrm{e}}n_{\mathrm{e}}v_{\mathrm{te}}\exp(-q_{\mathrm{e}}\phi_{\mathrm{d}}/KT_{\mathrm{e}}), \tag{3.4}$$

$$I_{\mathrm{i}}=\sqrt{8\pi}r_{\mathrm{d}}^2q_{\mathrm{i}}n_{\mathrm{i}}v_{\mathrm{ti}}(1-q_{\mathrm{i}}\phi_{\mathrm{d}}/KT_{\mathrm{i}}), \tag{3.5}$$

and

$$I_{\mathrm{p}}=-\pi r_{\mathrm{d}}^2q_{\mathrm{e}}J_{\mathrm{p}}Q_{\mathrm{ab}}Y_{\mathrm{p}}\exp(q_{\mathrm{e}}\phi_{\mathrm{d}}/KT_{\mathrm{p}}). \tag{3.6}$$

Here, r_{d} is the dust radius, $v_{\mathrm{te,i}}$ is the electron (ion) thermal velocity and ϕ_{d} is the dust floating potential. This potential may be related to the number of charges on the dust Z_{d} as well as the dust radius r_{d} by

$$Z_{\mathrm{d}}=\frac{4\pi\epsilon_0r_{\mathrm{d}}\phi_{\mathrm{d}}}{q_{\mathrm{e}}} \tag{3.7}$$

where ϵ_0 is the free space permittivity. Also, J_p, Q_ab, Y_p, and T_p are the photon flux, photon absorption efficiency, photoelectron yield, and average photoelectron temperature. The charging model adopted here is the continuous Orbital-Motion-Limited OML approach [*Bernstein and Rabinowitz,* 1959] and the same as used in earlier work on modelling the overshoot response of dust associated electron irregularities during radio wave heating [*Havnes et al.*, 2003; 2004]. It should be noted that due to the relatively small size of the dust grains ($r_\mathrm{d} \sim 10$ nm), they are expected to carry no more than a few charges and the use of a continuous charging model may certainly be brought into question. Several past modelling investigations on mesospheric dust charging applications [e.g. *Cui and Goree,* 1994; *Rapp and Lubken,* 2001; *Lie-Svenson et al.,* 2003; *Dimant and Milikh,* 2004] have utilized discrete charging models based on the work of [*Natanson,* 1960]. An important difference between the discrete charging model and the continuous charging model, assuming low charge state, is that the discrete charging model predicts weak sensitivity to dust radius r_d in contrast to the continuous charging model [*Dimant and Milikh*, 2004]. It may be important to bear in mind these differences in ultimately interpreting the results that follow. Discrete charging can be implemented within the framework of the present model in a straightforward manner and this will be discussed in the following sections.

The collision of charged dust with neutrals is implemented by using a Langevin method [*Winske and Rosenberg,* 1998] and the dust-neutral collision frequency is denoted by ν_dn. The motionless initially uncharged dust is taken to have density given by

$$n_\mathrm{d}(x) = n_\mathrm{d0}\left(1 + \frac{\delta n_\mathrm{d0}}{n_\mathrm{d0}}\sin(2\pi m x/\ell)\right) \tag{3.8}$$

where n_d0 is the undisturbed dust density, δn_d0 is the dust irregularity amplitude, m is the mode number, and ℓ is the system length of the model. The dust irregularity wavelength is $\lambda = \ell/m$. In the current model, the plasma irregularities ultimately result from charging of the electrons and ions onto this irregular dust density. The mechanism for the generation of the dust irregularities is beyond the scope of the present work. This is still a vigorously debated outstanding issue in the study of PMSE. Two primary mechanisms currently being investigated are neutral air turbulence [*Rapp and Lubken*, 2003] and plasma instabilities involving the charged dust [e.g. *D'Angelo* 2005].

The electron density is determined from quasi-neutrality

$$n_\mathrm{e}(x) = n_\mathrm{i}(x) + \rho_\mathrm{d}(x)/e \tag{3.9}$$

where ρ_d is the dust charge density and e is the unit charge. The electron velocity is described by the momentum equation

$$v_\mathrm{e} = \frac{1}{\nu_\mathrm{en}}\left(\frac{q_\mathrm{e}}{m_\mathrm{e}}E - \frac{KT_\mathrm{e}}{m_\mathrm{e}}\frac{\partial}{\partial x}(\log(n_\mathrm{e}))\right) \tag{3.10}$$

where all quantities are analogous to those for the ions. The electrostatic field is calculated from the condition of zero currents often used in ionospheric plasmas [*Hill*, 1978].

$$J_{\mathrm{T}} = q_{\mathrm{e}} n_{\mathrm{e}} \mathbf{v}_{\mathrm{e}} + q_{\mathrm{i}} n_{\mathrm{i}} \mathbf{v}_{\mathrm{i}} + J_{\mathrm{d}} = 0 \tag{3.11}$$

where J_{T} is the total current density of ions, electrons and dust and J_{d} is the dust current density calculated from the simulation dust particles. Substituting the previous expressions for the electron and ion velocities into equation (3.11), the electrostatic field can be calculated as

$$E = \frac{\left(\frac{q_{\mathrm{e}} K T_{\mathrm{e}}}{m_{\mathrm{e}} \nu_{\mathrm{en}}} \frac{\partial n_{\mathrm{e}}}{\partial x} + \frac{q_{\mathrm{i}} K T_{\mathrm{i}}}{m_{\mathrm{i}} \nu_{\mathrm{in}}} \frac{\partial n_{\mathrm{i}}}{\partial x} - J_{\mathrm{d}} \right)}{\left(\frac{q_{\mathrm{e}}^2}{m_{\mathrm{e}} \nu_{\mathrm{en}}} n_{\mathrm{e}} + \frac{q_{\mathrm{i}}^2}{m_{\mathrm{i}} \nu_{\mathrm{in}}} n_{\mathrm{i}} \right)}. \tag{3.12}$$

It should be noted that since $m_{\mathrm{d}} \gg m_{\mathrm{i}} \gg m_{\mathrm{e}}$, to a good approximation,

$$E \approx \frac{K T_{\mathrm{e}}}{q_{\mathrm{e}}} \frac{\partial}{\partial x} \log(n_{\mathrm{e}}). \tag{3.13}$$

This is essentially a description of Boltzmann behavior for the electrons. To reiterate, for the time regimes under consideration in this work, the dust particles do not move during the simulation period and, therefore, $J_{\mathrm{d}} = 0$.

It is useful to consider the temperature dependence of important quantities in the above model that will affect the irregularities through electron temperature variations during heating [*Banks and Kockarts*, 1973]. The electron neutral collision frequency ν_{en} varies with temperature and its variation is taken as $\nu_{\mathrm{en}} \sim T_{\mathrm{e}}^{1/2}$ here, however, it may be argued that a somewhat more accurate dependence is $\nu_{\mathrm{en}} \sim T_{\mathrm{e}}^{5/6}$ [*Gurevich*, 1978]. The recombination coefficient also varies with electron temperature and its variation is taken to be $\alpha \sim T_{\mathrm{e}}^{-1/2}$. This, of course, indicates the well known fact that heating of the ionosphere can increase plasma density through reduction in α [*Gurevich,* 1978]. Another important process that will be affected by electron heating is the dust charging which can clearly be seen from equation (3.4). A larger flux of electrons onto the dust particles will exist. This will produce a corresponding decrease in electron density and an increase in the dust charge density.

It should be noted that the electron irregularities are ultimately observed as backscattered radar signals. The relationship between the irregularities and the radar reflectivity is given by the expression [*Royrvik and Smith* 1984]

$$\eta(k) = -n \frac{\pi}{8} k^2 \frac{\omega_{\mathrm{pe}}^4}{4\omega^4} \frac{S_{\mathrm{n_e}}(k)}{n_{\mathrm{e}}^2} \tag{3.14}$$

where $k = 2\pi/\lambda$ and ω are the wave number and radian frequency of the radio wave, ω_{pe} is the electron plasma frequency, n is the exponent of the electron power spectral density and $S_{n_e}(k)$ is the one dimensional power spectrum of the electron irregularities. For the sinusoidal perturbations used in this work to model the irregularities, $\eta(k) \sim \delta n_e^2$ where δn_e is the electron irregularity amplitude.

3.2 Charging and Diffusion Timescales

There are several important timescales that must be considered to interpret the temporal behavior of the model just described.

Neglecting photoemission effects in the present work, from (3.3) the dust charge number Z_d will vary in time according to

$$\frac{d(Z_d e)}{dt} = I_e + I_i. \tag{3.15}$$

From equations (3.4) and (3.5), the dust charging period is defined in the present work as

$$\tau_c = \frac{e}{|\langle I_e + I_i \rangle|} \geq \frac{1}{\sqrt{8\pi} n_e v_{te} \langle r_d^2 \rangle} \equiv \tau_{c0}. \tag{3.16}$$

Note that $\langle \cdot \rangle$ indicates the average over all the dust particles in the simulation. It is useful to consider plasma parameters typical of the mesosphere to estimate the charging time relative to other timescales. The PMSE irregularity generation region exists in the altitude range around 85 km. At this altitude region the plasma density $n_e = n_i \equiv n_0 \sim 10^{10}$ m^{-3}. The plasma temperature is typically $T_e = T_i = 150$°K, therefore, the electron thermal velocity is $v_{te} \sim 10^5$ m/s. The ion mass $m_i \approx 50 m_p$ where m_p is the proton mass. The ions are highly collisional with $\nu_{in} \sim 10^5$ s^{-1}. Also, subvisible mesospheric dust associated with PMSEs is believed to typically be $r_d \sim 10$ nm. For such plasma parameters, the minimum charging time, defined as τ_{c0} in (3.16), is determined by the electron current to the uncharged dust and $\tau_{c0} \sim 1$ s. Of course, the charging time varies significantly during the heating cycle. The charging time decreases significantly during the turn-on and turn-off of the radio wave as will be discussed in more detail shortly. Approximate analytical expressions will be provided as well.

The next important time-scale is the diffusion time. As T_e is increased by radio wave heating, the diffusion of electrons is enhanced and this will tend to destroy the irregularity [*Rapp and Lubken,* 2000]. As the electrons diffuse to 'fill in' the irregularity, the ions are dragged along into the region of reduced electron density by ambipolar diffusion. It has been observed in previous numerical simulation work

[*Lie-Svenson et al.,* 2003] that for irregularities of meter scales or less, this may lead to an enhancement in ion density in regions of electron density reduction. This 'anticorrelation' in the electron and ion density perturbations has been observed in past in-situ sounding rocket observations of irregularities in the PMSE generation region. The time-scale for this ambipolar diffusion can be roughly approximated for the model used here as [e.g. [*Chen,* 1985]

$$\tau_{\mathrm{d}} \approx \left(\frac{\lambda}{2\pi}\right)^2 \frac{1}{D_{\mathrm{a}}}. \tag{3.17}$$

Here the sinusoidal irregularity wavelength in the simulation model is denoted by λ and the ambipolar diffusion coefficient can be approximated by [e.g. *Hill*, 1978]

$$D_{\mathrm{a}} \approx \frac{KT_{\mathrm{i}}}{m_{\mathrm{i}}\nu_{\mathrm{in}}}\left(1+\frac{T_{\mathrm{e}}}{T_{\mathrm{i}}}\right)\left(1+\frac{Z_{\mathrm{d0}}n_{\mathrm{d0}}}{n_{\mathrm{e0}}}\right) \tag{3.18}$$

where $Z_{\mathrm{d0}}, n_{\mathrm{d0}}$, and n_{e0} are background values of the dust charge number, dust number density, and electron number density which may vary in time due to dust charging. As described by *Hill* [1978], this diffusion coefficient is derived from linearized diffusion equations, however, it typically is found to have quite reasonable agreement with the electron flux to electron density gradient ratio, $-n_{\mathrm{e}}v_{\mathrm{e}}/(\partial n_{\mathrm{e}}/\partial x)$, in simulations of the numerical model just described which incorporates nonlinear effects.

As an example, considering a radar frequency of 50MHz, the equivalent Bragg scattering wavelength is approximately 3 meters. Also, assuming $\nu_{\mathrm{in}} \sim 10^5$ Hz and $T_{\mathrm{e}} = T_{\mathrm{i}}$ the time-scale for diffusion is of the order of 1 second. When the radio wave heating is turned on, this diffusion time decreases, also, from (3.17), the diffusion time varies sensitively with λ. Therefore depending on the parameters, τ_{d} can be smaller or larger than τ_c. This is expected to lead to fundamental changes in the temporal evolution of the irregularities. From the previous estimates stated, prior to radio wave heating, $\tau_{\mathrm{d}}/\tau_c \sim 1$ for irregularities observed in the 50 MHz range and therefore charging effects are expected to become more important near and below this observing radar frequency for 10nm dust.

Two other time-scales of importance are the electron-ion photoionization production time and the charging time associated with ion attachment on the dust. The time for ion charging of dust is much larger than that of electron charging by the ratio of electron to ion thermal velocity $v_{\mathrm{te}}/v_{\mathrm{ti}} = \sqrt{T_{\mathrm{e}}m_{\mathrm{i}}/T_{\mathrm{i}}m_{\mathrm{e}}} \gg 1$ as can be seen from equations (3.4) and (3.5). Therefore, the ion charging time onto the uncharged dust grains is of the order of 100 seconds. This indicates that ion charging is of much less importance during the turn-on of the radio wave heating, however, as has been noted earlier [*Havnes et al.*, 2004] and will be discussed in more detail shortly, ion charging dominates during 'turn-off'. Electrons and ions are produced by photoionization as the electron density is reduced by charging. This can be seen from the continuity equation (3.1) since there is an imbalance in P_i and L_i in this case. Also, the reduction of the recombination rate α due to increase in T_e causes a production of electrons and ions as well. From the equilibrium relationship $P_\mathrm{i} = \alpha n_0^2$, the production time can be written as $t_\mathrm{p} = 1/\alpha n_0$. For typical mesospheric parameters, $\alpha \sim 10^{-12}$ m^{3}s^{-1} and the production rate is of the order of 100 seconds which is comparable to the ion charging time. Therefore, both the ion charging time and electron-ion production rate are roughly of the same order.

3.3 Scale Size Effects on Irregularity Evolution

The increase in the electron temperature T_e by radio wave heating can be described by the well known relationship obtained from energy balance [*Gurevich,* 1978; *Milikh,* 1994]

$$\frac{dT_\mathrm{e}}{dt} = -\frac{2}{3} e v_\mathrm{e} E - \delta \nu_\mathrm{e}(T_\mathrm{e} - T). \tag{3.19}$$

The first term on the right side of (3.19) is the contribution from ohmic heating and the second term is the collisional loss. The effective fractional energy loss during a collision is δ and the effective electron-neutral collision frequency is ν_e. T denotes the effective temperature of the background species and E is the electric field of the radio wave. It should be noted that in general $\delta \ll 1$ and both δ and ν_e will have nontrivial temperature dependencies [*Gurevich,* 1978]. The time-scales for this heating is milliseconds and therefore in the simulation model, this can be essentially considered as an instantaneous temperature change when the heater is turned 'on' or 'off' since this is much faster than any other important time-scale described in the previous section.

The effects of ionospheric radio wave heating on electron irregularities believed to produce PMSEs was investigated with the model just described in the previous section. In this model, the dust remains motionless during the time scales of the simulation, therefore, the neutral dust density is constant with time. The electron and ion densities are initialized with equal density $n_{\mathrm{e}0} = n_{\mathrm{i}0} = n_0$. In the mesosphere, the relative dust density to background plasma density may cover a wide range, therefore the ratio $n_{\mathrm{d}0}/n_0$ may vary considerably. For the present results, this ratio is taken to be $n_{\mathrm{d}0}/n_0 = 0.05$ and the dust is set to have constant radius (or mass). The effects of varying the dust density and varying the dust radius distribution will be discussed subsequently. Also, photoemission currents are neglected here. The simulation system length is taken to be $\ell = 4096\lambda_\mathrm{D}$ where λ_D is the Debye length in the undisturbed plasma. For the mesosphere λ_D is of the order of 1 centimeter and, therefore, $\lambda_\mathrm{D} \approx 1$ cm is assumed in the results that follow.

After initialization, the dust is allowed to charge until an equilibrium state is reached. Subvisible mesospheric dust associated with PMSEs is believed to typically be of 10 nm size. This corresponds to the dust having an equilibrium charge of about 1 electron prior to heating. Therefore, the equilibrium charge is taken to be $Z_{\mathrm{eq}} = 1$ which from equation (3.7) is consistent with $r_{\mathrm{d}} \approx 10$ nm. For the parameter regimes considered in this work, typically equilibrium in the plasma irregularities is reached near $t = 25\tau_{\mathrm{c0}}$. The time to reach equilibrium does vary somewhat within the parameter regimes as can be seen in the results that follow. However, allowing the the system to run longer than $t = 25\tau_{\mathrm{c0}}$ does not significantly alter the temporal behavior during the simulated turn-on of the radio wave heating. Therefore, to conserve computational time, in all results that follow, the system is allowed to run until $t = 25\tau_{\mathrm{c0}}$ before the temperature enhancement is applied.

After the initial equilibrium state is reached, the electron temperature is increased from its initial value T_{e0} the final value T_{e}. For reasonable consistency with past experimental estimates [*Chilson et al.,* 2000], this value is taken to be $T_{\mathrm{e}}/T_{\mathrm{e0}} = 10$ in the present discussion. The effects of varying the degree of temperature enhancement $T_{\mathrm{e}}/T_{\mathrm{e0}}$ will be discussed later. After the system reaches a quasi-steady state again with the enhanced $T_{\mathrm{e}}/T_{\mathrm{e0}}$ ratio, this ratio is then reduced back to $T_{\mathrm{e}}/T_{\mathrm{e0}} = 1$. The ion temperature T_{i} is held constant during the simulation.

Figure 3.1 shows the time evolution of the electron, ion, and dust charge irregularity amplitudes during the heating process. In this case, $\lambda/\lambda_{\mathrm{D}}$=128, corresponding to a radar frequency approximately in the range of 120 MHz, which is of similar order compared to previous observations [*Havnes et al.,* 2003; *Havnes,* 2004]. In the simulation, the dust is allowed to charge from a neutral charge state until $t/\tau_{\mathrm{c0}} = 25$. Note again, $\tau_{\mathrm{c0}} \sim 1$ s denotes the initial charging time for electrons onto uncharged dust. At time $t/\tau_{\mathrm{c0}} = 25$, the system has reached an equilibrium at temperature $T_{\mathrm{e}} = T_{\mathrm{i}} = 150$°K. The heating is then turned on, resulting in a rapid electron temperature increase. The temperature increase reduces the electron density irregularities through diffusion [*Rapp and Lubken*, 2000]. It is noted that the irregularity amplitude is initially suppressed with slow recovery as the heating continues. Eventually another equilibrium state is reached. When the heating is turned off at $t/\tau_{\mathrm{c0}} = 125$ an immediate enhancement is observed in the electron irregularity amplitude. This is the 'PMSE overshoot' effect predicted and observed in previous work [*Havnes et al*, 2003; 2004]. By the end of the simulation at $t/\tau_{\mathrm{c0}} = 300$, the irregularity amplitudes have returned to the initial equilibrium. It can be noted that the ion irregularities are enhanced during the heating due to the ambipolar diffusion as the electron irregularities flatten out, also, the dust charge irregularities are enhanced due to dust charging. It should be noted that at turn-off, $t/\tau_{\mathrm{c0}} = 125$, there is rapid reduction in the ion irregularity amplitude that coincides with the rapid increase in electron irregularity amplitude. As will be discussed shortly, this is due to the diffusion process.

Figure 3.2 shows the time evolution for an irregularity of larger spatial scale taken to be $\lambda/\lambda_{\mathrm{D}}$=2048. The corresponding radar frequency would be in the range of 8

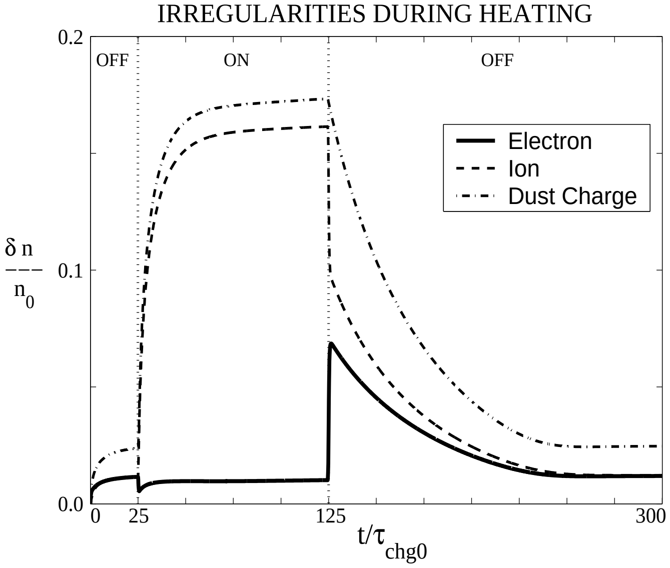

Figure 3.1: Time evolution of electron, ion, and dust charge irregularities before (OFF), during (ON), and after (OFF) radio wave heating. In this case T_e/T_{e0}=10 during heating. Also, λ/λ_D=128. In this case, "Turn-Off" overshoot is evident.

MHz in this case. It can be seen that the temporal evolution of the electron irregularities is considerably different in this regime. After turn-on at $t/\tau_{c0} = 25$, there is a significant initial enhancement in the electron irregularity amplitude and subsequent relaxation to lower, but still enhanced, amplitude. When the heating is turned off at $t/\tau_{c0} = 125$, there is a very subtle increase in amplitude consistent with the overshoot observed in the previous Figure. The irregularities then relax to their initial values. For the purposes of this work, the electron irregularity amplitude overshoot such as observed during heating turn-off in Figure 3.1 will be termed 'turn-off overshoot' and the overshoot in electron irregularity amplitude as observed in Figure 3.2 is termed 'turn-on overshoot'.

Increasing the irregularity scale size to λ/λ_D=4096, which corresponds to a lower radar frequency in the range of 4 MHz is considered next. Figure 3.3 indicates that the amplitude of the electron density irregularities in this case are enhanced throughout the heating with no overshoot effects during turn-on or turn-off. It is also observed that in the case of Figure 3.3, the ion irregularities tend to have a significantly smaller amplitude than the electron irregularities throughout the heating. Comparing Figures 3.1, 3.2, and 3.3, it can be noted that the ion fluctuation amplitude relative to the electron fluctuation amplitude decreases as the irregularity scale size increases. This is due to the decreased role of diffusion [e.g. *Lie-Svenson et al.,* 2003]. It should

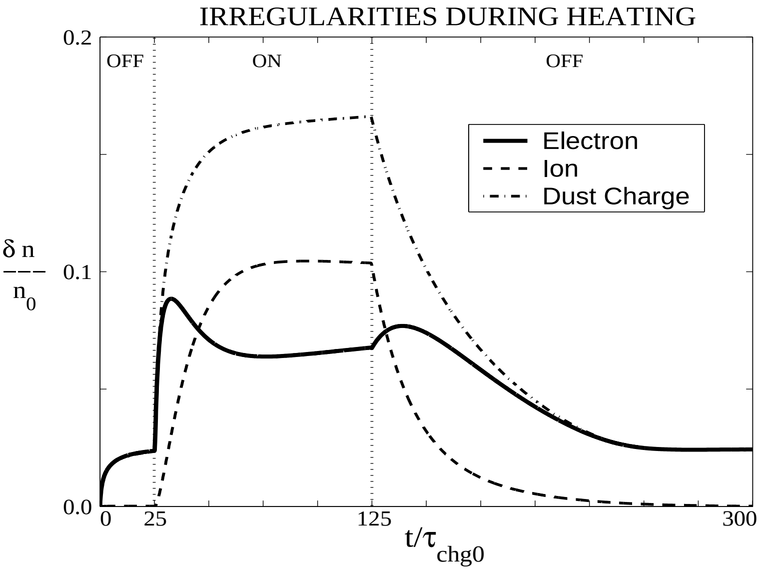

Figure 3.2: Time evolution of electron, ion, and dust charge irregularities before (OFF), during (ON), and after (OFF) radio wave heating. In this case T_e/T_{e0}=10 during heating. Also, λ/λ_D=2048. In this case, "Turn-On" overshoot is evident.

be noted that in this case, the diffusion time is significantly longer than the heating period of $100\tau_{c0}$.

Figure 3.4 compares the effects of irregularity scale-size on the evolution during heating in more detail. Figure 3.4 shows the relative electron irregularity evolution for a variation in scale-size for λ/λ_D = 128, 256, 512, 1024, and 2048. For λ_D typical of the mesosphere at 85 km, these cases correspond to irregularities in the range of roughly 1 to 20 meters. Approximate corresponding radar frequencies are also shown. It can be seen that the shorter scale irregularities exhibit more prominent turn-off overshoot effects whereas longer scale irregularities tend to exhibit more prominent turn-on overshoot effects during heating. As the scale-size is increased there is a transition between prominent turn-off to turn-on overshoot effects. It is observed that the longer scale irregularities take longer to reach a maximum overshoot during turn-off. Also the overshoot persists for longer periods of time during turn-on for the longer scale irregularities.

It should be noted that Figures 3.1 to 3.4 show results for a single scale size of irregularity as described by equation (3.8). It is useful to consider a case with multiple scales sizes for further interpretation of the results. Figure 3.5 shows 10 time snapshots of the electron density irregularity amplitude $\delta n_e/n_{e0}$ during a simulation. For clarity,

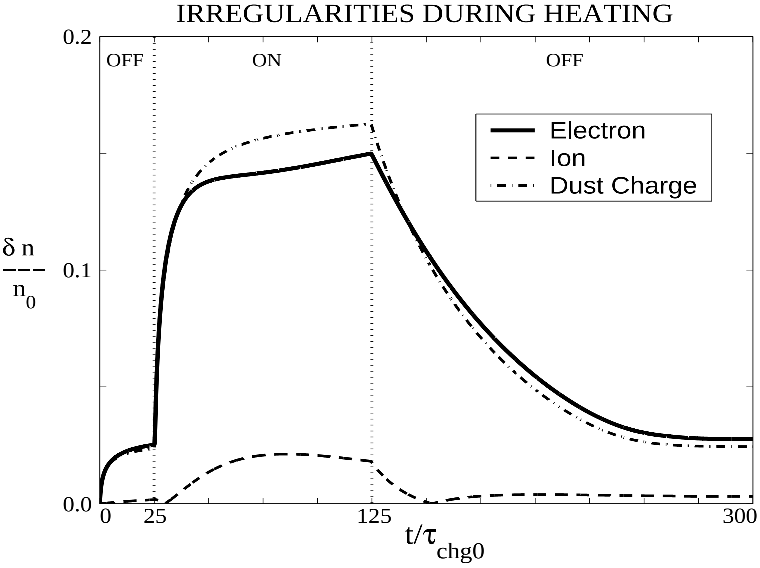

Figure 3.3: Time evolution of electron, ion, and dust charge irregularities before (OFF), during (ON), and after (OFF) radio wave heating. In this case $T_\mathrm{e}/T_\mathrm{e0}$=10 during heating. Also, $\lambda/\lambda_\mathrm{D}$=4096. In this case, irregularity enhancement is evident throughout the heating.

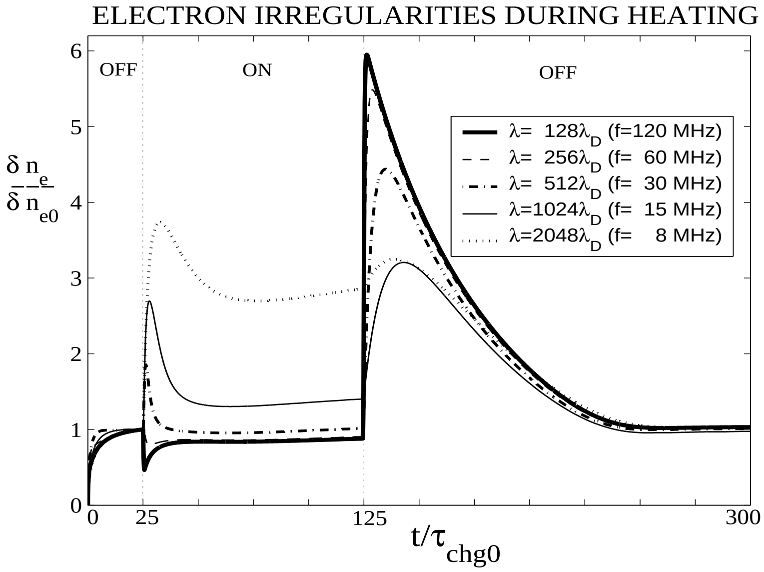

Figure 3.4: The time evolution of electron irregularities during radio wave heating with varying irregularity scale size (and radar frequency).

only half of the simulation box is shown which is the region $0 < x < 2048\lambda_{\mathrm{D}}$. The neutral dust density in (3.8) is extended to include a superposition of several scale sizes and this density is given by

$$n_{\mathrm{d}}(x) = n_{\mathrm{d0}}\left(1 + \sum_{l=1}^{6} \frac{\delta n_{\mathrm{d0}}}{n_{\mathrm{d0}}} \sin(2\pi m_{\mathrm{l}} x/\ell)\right). \tag{3.20}$$

Six modes are included which correspond to scales sizes of $\lambda = 64\lambda_{\mathrm{D}}$, $128\lambda_{\mathrm{D}}$, $256\lambda_{\mathrm{D}}$, $512\lambda_{\mathrm{D}}$, $1024\lambda_{\mathrm{D}}$, and $048\lambda_{\mathrm{D}}$.

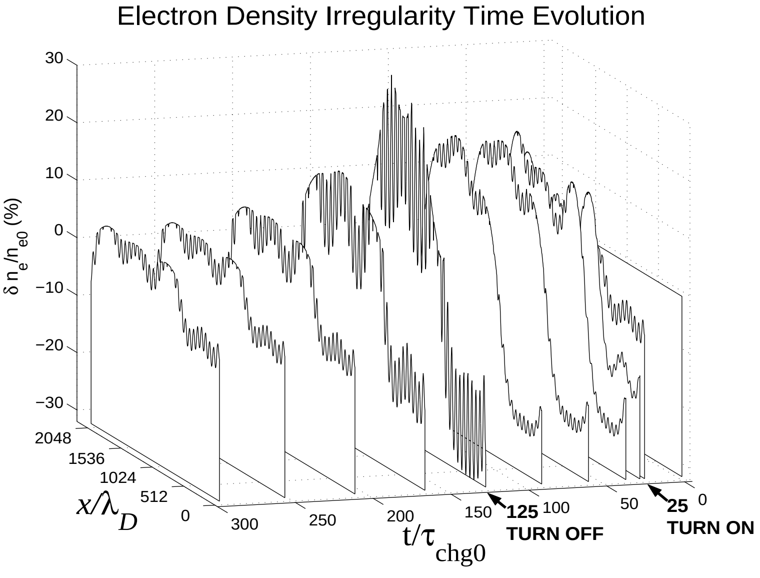

Figure 3.5: Electron density fluctuation evolution before, during, and after radio wave heating.

As in the previous simulations, the dust is allowed to charge from a neutral charge state until $t/\tau_{\mathrm{c0}} = 25$. The heating is turned on at this time (again $T_{\mathrm{e}}/T_{\mathrm{e0}} = 10$) and turned off at $t/\tau_{\mathrm{c0}} = 125$. It can be seen that when the heating is turned-on, there is suppression of the smaller scale irregularities (primarily due to diffusion) and enhancement of the larger scale irregularities which corresponds to the turn-on overshoot. Some recovery of the small scale irregularities can be observed during continued heating. During turn-off, a dramatic increase in the small scale irregularities can be observed. Ultimately, there is a relaxation of the irregularities back to the initial equilibrium values by $t/\tau_{\mathrm{c0}} = 300$.

From the results just described, it is clear that the scale size of the irregularity is a very important factor in the temporal evolution of the irregularities during heating.

This of course is an indication that the temporal evolution may be significantly different depending on the observing radar frequency.

The difference in temporal behavior during heating with irregularity scale size may be explained by the change in different fundamental timescales discussed in section 3.3. As the irregularity scale size is increased, the effects of diffusion become less important and the effects of charging become more important. The relative importance is described by the relative size of the charging time τ_c compared to the diffusion time τ_{d}. A condition for irregularity amplitude overshoot during turn-on is expected to be $\tau_{\mathrm{d}}/\tau_c \gg 1$. In this case, after turn-on, rapid charging will lead to a rapid reduction in electron density in regions of dust density enhancements before diffusion effects can smooth out the electron irregularities. This will result in an initial enhancement of the electron irregularities before diffusion effects act to reduce the electron density gradients. If the diffusion effects are significantly slow to act during the heating period, the electron irregularities may be enhanced throughout the entire heating period which is the case in Figure 3.3. A condition for the turn-off overshoot is expected to be $\tau_{\mathrm{d}}/\tau_c \ll 1$. During heating, the electron irregularity amplitude has been suppressed by diffusion, however, this amplitude is still enhanced in comparison to the irregularity amplitude if no charging had occurred. If $\tau_{\mathrm{d}}/\tau_c \ll 1$ during turn-off, diffusion acts rapidly to return the electron (and ion) density gradients to the values prior to heating before any effects of dust discharging can occur. Therefore, as the density gradients return to the values prior to heating, the electron irregularities actually become larger than the values prior to heating which is the turn-off overshoot. After the overshoot, the electron irregularity amplitude relaxes to the value prior to heating on a slower timescale due to a combination of ion charging, recombination, and diffusion.

Figure 3.6 shows the electron diffusion and charging time ratio τ_{d}/τ_c during radio wave heating with varying irregularity wavelengths from 128 λ_{D} to 2048 λ_{D}. The parameters used are the same as Figures 3.1 through 3.4. Approximate observing radar frequencies are also shown. It can be seen that during turn-on and turn-off there is a significant increase in this ratio. Considering the two shorter scale sizes first ($\lambda/\lambda_{\mathrm{D}} = 128$ and 256), it can be seen that $\tau_{\mathrm{d}}/\tau_c \ll 1$ during turn-on and turn-off. This should indicate no turn-on overshoot but a turn-off overshoot may exist. This is consistent with Figure 3.4. For the scale size $\lambda_{\mathrm{D}} = 512$, τ_{d}/τ_c is marginally larger than 1 during turn-on and a small turn-on overshoot is observed in Figure 3.4 During turn-off $\tau_{\mathrm{d}}/\tau_c < 1$ and a turn-off overshoot is observed in Figure 3.4 as predicted. Considering the next two largest scale size cases, $\lambda_{\mathrm{D}} = 1024$ and 2048, it can be seen that $\tau_{\mathrm{d}}/\tau_c > 1$ during turn-on in both cases which predicts a turn-on overshoot as can be seen Figure 3.4. For the case $\lambda_{\mathrm{D}} = 2048$, $\tau_{\mathrm{d}}/\tau_c \gg 1$ during turn-off which indicates a significantly diminished turn-off overshoot is predicted. This is consistent with Figure 3.4. For the case $\lambda_{\mathrm{D}} = 1024$, $\tau_{\mathrm{d}}/\tau_c \sim 1$ during turn-off and in a intermediate regime. A turn-off overshoot is observed, however, it has a similar amplitude to the turn-on overshoot. Therefore in general, it can be argued that conditions for the existence of turn-on and turn-off overshoots in the electron irregularity amplitudes during heating are described by the relative size of the diffusion to charging times as shown in Figure 3.6.

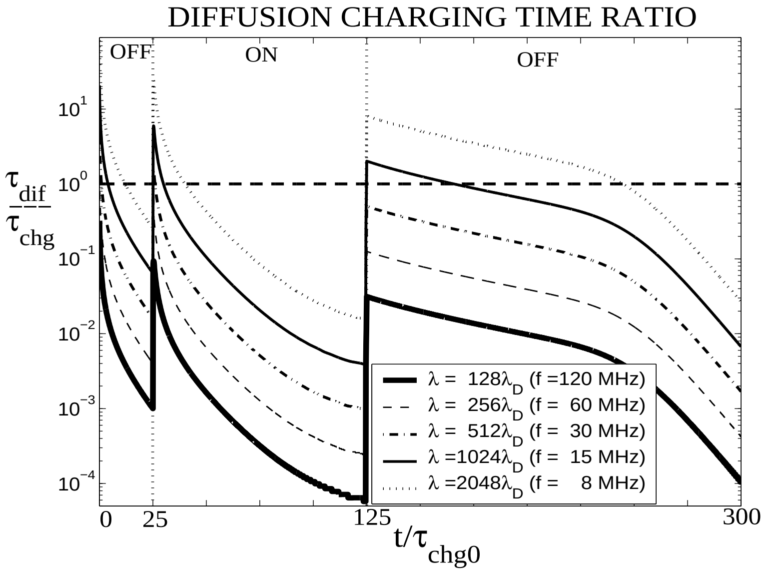

Figure 3.6: The electron diffusion to dust charging time ratio during radio wave heating with varying irregularity scale size (and radar frequency).

3.4 Dust Density Effects on Irregularity Evolution

The dust density is an important factor in the temporal evolution of electron irregularities during heating. As long as $Z_{\mathrm{d}}n_{\mathrm{d}}/n_{\mathrm{e}} < 1$, the effect of increasing dust density has relatively weak effects on the two important timescales τ_c and τ_{d} in equations (3.16) and (3.17). However, the primary effect of increasing the dust density is to significantly reduce the background electron and ion densities. This effect of reducing the background plasma density will be dominant over the charging and diffusion processes that ultimately produce the overshoot effects which have just been described. Therefore, higher dust densities are expected to significantly weaken the electron irregularities and essentially mask the overshoot effects. Figure 3.7 shows the temporal evolution of the electron irregularity amplitude for several values of dust density $n_{\mathrm{d0}}/n_0 = 5\%, 10\%, 25\%$ and 50%. In this case, the irregularity scale size $\lambda/\lambda_{\mathrm{D}} = 512$ with the other parameters the same as in the cases considered in the previous sections. For the low dust density case, $n_{\mathrm{d0}}/n_0 = 5\%$, both turn-on and turn-off overshoots exist with similar physical behavior as described in the previous sections. Increasing to $n_{\mathrm{d0}}/n_0 = 10\%$ is seen to reduce both the overshoots. Also, during heating a significant reduction in the irregularities during heating can be seen in comparison to the low dust density case. Increasing to 25% dust density greatly reduces the presence of both overshoots and also almost completely suppresses the irregularities (and background plasma density) during the heating period. A weak overshoot is observed at $t/\tau_{\mathrm{c0}} = 150$ during the recovery of the irregularities during turn-off for this case but the electron irregularities have been suppressed so much that this overshoot still has a smaller amplitude than the equilibrium irregularity amplitude. For the case of 50% dust density, the electron irregularities essentially exhibit no overshoots with the density being reduced during turn-on and recovering during turn-off. It should be noted that the temporal behavior of the diffusion charging time ratio τ_{d}/τ_c (not shown) predicts both turn-on and turn-off overshoots for all four dust density cases. This indicates that the overshoot effects are masked by the large reduction in background plasma density as the relative dust density is increased. This also indicates that the prediction of overshoot effects using the ratio τ_{d}/τ_c is most likely limited to the case of relatively low dust densities $Z_{\mathrm{d}}n_{\mathrm{d}}/n_{\mathrm{e}} \ll 1$.

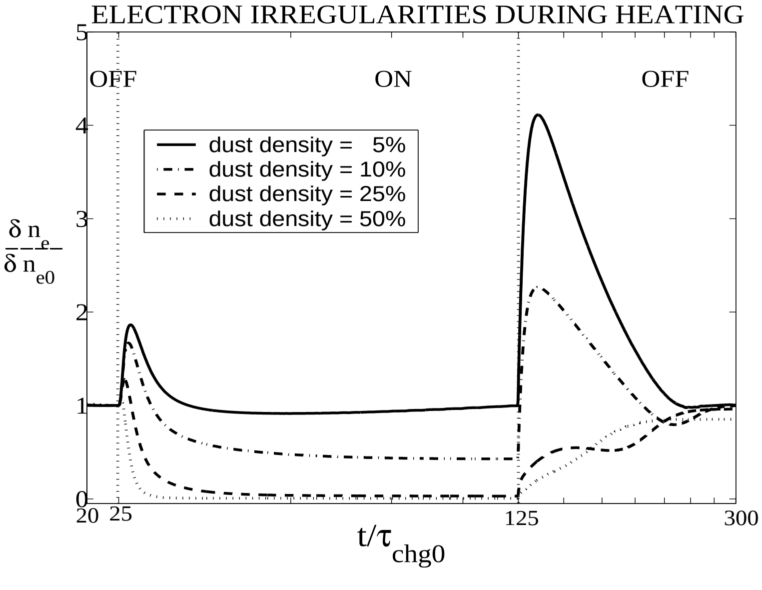

Figure 3.7: The time evolution of electron irregularities during radio wave heating with varying dust density. Here $\lambda/\lambda_{\mathrm{D}}$=512.

3.5 Dust Size Effects on Irregularity Evolution

For relatively low dust densities, section 2.2 predicts that the dust radius has a more significant effect on the charging time than the diffusion time. An increase in r_d decreases the dust charging time. Therefore, an increase in dust radius will increase the ratio τ_d/τ_c. Ultimately, this is expected to enhance the turn-on overshoot relative to the turn-off overshoot. Figure 3.8. shows the relative variation of the electron irregularities during heating with increasing r_d. In this case, the dust density is 1% of the initial plasma density, i.e. $n_\mathrm{d0}/n_0 = 0.01$ and the wavelength is $\lambda = 512\lambda_\mathrm{D}$. It can be seen with $r_\mathrm{d} = 10$ nm, a relatively weak turn-on overshoot is observed and a prominent turn-off overshoot exists. As r_d is increased to 20, 30, and 40, nm, the turn-off overshoot is reduced relative to the turn-on overshoot as expected. Also, the turn-on overshoot is enhanced. For the case $r_\mathrm{d} = 40$ nm, the turn-on overshoot has a larger amplitude than the turn-off overshoot. Due to larger r_d, more significant suppression of the electron irregularities can be observed during heating since more electrons are attached to the larger dust grains. Figure 3.9. shows the ratio τ_d/τ_c for the cases shown in Figure 3.8. It can be seen that for $r_\mathrm{d} = 10$ nm, τ_d/τ_c is slightly larger than 1 at turn-on and a turn-on overshoot exists. The ratio increases to be larger than 1 as r_d is increased and the turn-on overshoot can be seen to become stronger. At turn-off, the ratio is slightly smaller than 1 and the turn-off overshoot exists. As r_d is increased, the ratio increases to be larger than 1 and the turn-off overshoot is significantly reduced relative to the turn-on overshoot.

So far only the case of constant radius dust has been considered. Typically a range of dust radii would be expected to exist. The model of section 2 has been used to consider the effects of dust radius distributions. For relatively small dust density, the primary effect of r_d would be expected to be on the dust charging. This variation for a distribution of radii would be inversely proportional to $\langle r_\mathrm{d}^2 \rangle$ from (3.16). Therefore, dust radii distributions with the same root mean square RMS dust radii, $\sqrt{\langle r_\mathrm{d}^2 \rangle}$, would be expected to have very similar electron irregularity temporal behavior during heating. A useful dust radius distribution may be inferred from numerical simulations of mesospheric ice particle growth by *Berger and Zahn* [2002]. The results of this model indicate a Gaussian normal form of the dust radius distribution is expected for mesospheric applications [*Dimant and Milikh*, 2004]. Therefore, a dust radius distribution of the form

$$f(r_\mathrm{d}) = \frac{1}{\sigma_{r_\mathrm{d}}\sqrt{2\pi}} e^{-(r_\mathrm{d}-r_\mathrm{d0})^2/2\sigma_{r_\mathrm{d}}} \tag{3.21}$$

is considered where r_d0 is the mean dust radius and σ_{r_d} is the standard deviation in the dust radius. It is assumed that $\sigma_{r_\mathrm{d}} = r_\mathrm{d0}/2.5$ for reasonable consistency with the results of *Berger and Zahn* [2002]. Figure 3.10 shows the temporal evolution of the electron irregularities during radio wave heating for a constant dust radius of 10nm and also for a Gaussian dust radius distribution described by (3.21) with an RMS dust radius of 10nm. For reference, the results are also shown for a uniform dust radius distribution with RMS dust radius of 10nm. For each case $n_{\mathrm{d}0}/n_0 = 0.05$, i.e. the dust density is 5% of the background density. The wavelength $\lambda = 512\lambda_{\mathrm{D}}$. The other parameters are the same as in the previous sections. Results show that there are minor differences in the electron irregularity behavior for the dust radius distributions and the constant 10nm radius case. There are also only minor differences in the temporal behavior of the ratio τ_{d}/τ_c for the three cases (not shown).

3.6 Temperature Effects on Irregularity Evolution

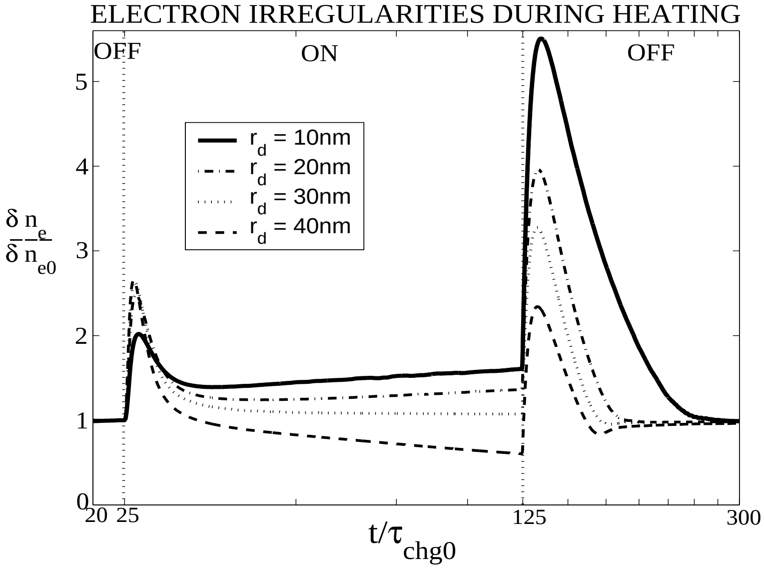

Figure 3.8: The time evolution of electron irregularities during radio wave heating with varying dust radius. Here $n_{\mathrm{d}0}/n_0$=0.01 and $\lambda/\lambda_{\mathrm{D}} = 512$.

The degree of electron temperature enhancement during radio wave heating is expected to affect the electron irregularity temporal evolution. Increasing the degree of electron temperature enhancement is expected to increase the dust charging which ultimately results in increased electron irregularity amplitudes as well as increased dust charge density irregularity amplitudes. Increasing the degree of electron temperature enhancement is also expected to alter the charging and diffusion timescales as can be seen from equations (3.16) and (3.17). However, the relative change between these two timescales through the ratio τ_{d}/τ_c will ultimately determine any effects on the relative importance of overshoot features. A number of simulations were performed to access these effects. In all previous results presented in this section, the

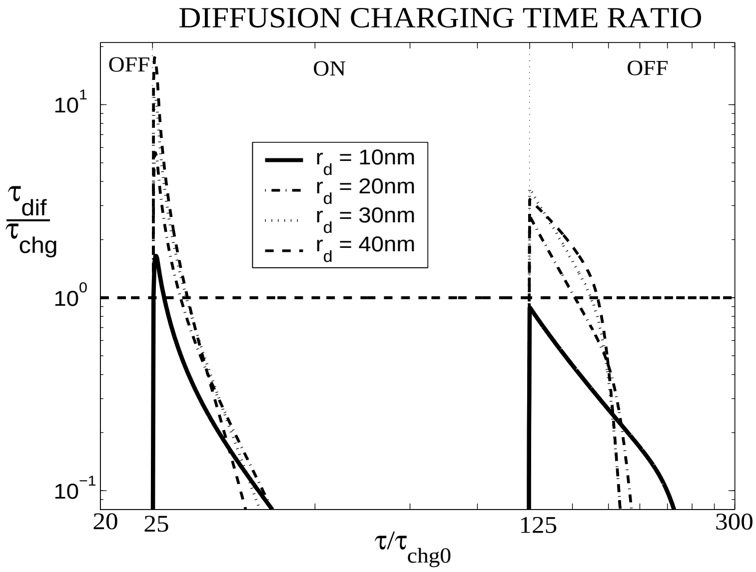

Figure 3.9: The electron diffusion to dust charging ratio during radio wave heating with varying dust radius for the previous figure.

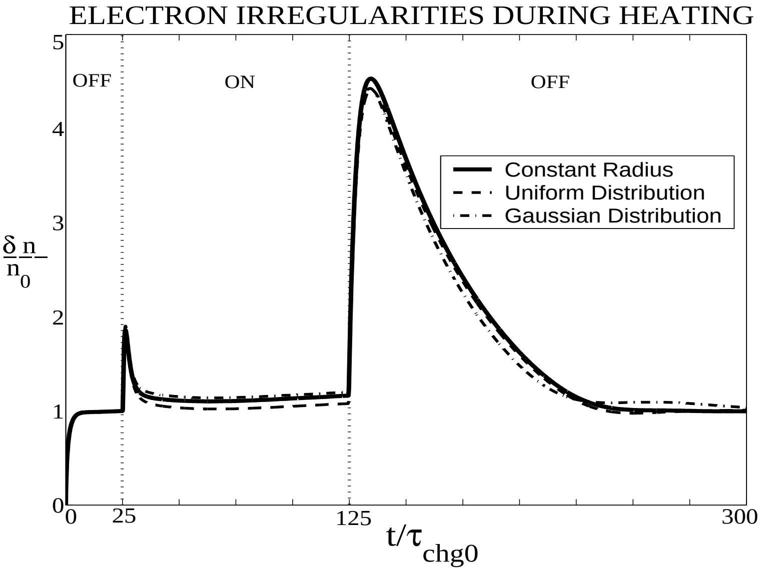

Figure 3.10: The time evolution of electron irregularities during radio wave heating with varying dust radius distributions with the same RMS dust radius of 10nm.

degree of electron temperature enhancement was taken to be a factor of 10, i.e. the initial to final electron temperature ratio $T_\mathrm{e}/T_\mathrm{e0} = 10$. Recall that the initial electron temperature prior to heating is equal to the ion temperature $T_\mathrm{e0} = T_\mathrm{i}$. Figure 3.11. shows the electron irregularity temporal evolution for three values of temperature enhancement, $T_\mathrm{e}/T_\mathrm{e0} = 4$, 10, and 20. In each case $n_\mathrm{d0}/n_\mathrm{e0} = 0.01$ (i.e. 1%) and $\lambda/\lambda_\mathrm{D} = 1024$. For this wavelength case, both the turn-on and turn-off overshoots are observed to exist during the radio wave heating. It can be seen that increasing the degree of temperature enhancement in general increases the amplitude of both of the overshoot features. This same general result is observed for both longer and shorter wavelength irregularities in the range from $128\lambda_\mathrm{D}$ to $4028\lambda_\mathrm{D}$. Also varying the dust density shows similar results. In all cases, relatively small changes are observed in the ratio τ_d/τ_c as $T_\mathrm{e}/T_\mathrm{e0}$ is varied in the range from $4 < T_\mathrm{e}/T_\mathrm{e0} < 20$. Therefore, the primary effect of increasing the degree of electron temperature enhancement in the parameter regime considered here is an increase in the overshoot amplitudes rather than any significant change in the relative strength of the two overshoot features such as is the case for the variations in dust size and irregularity wavelength described earlier.

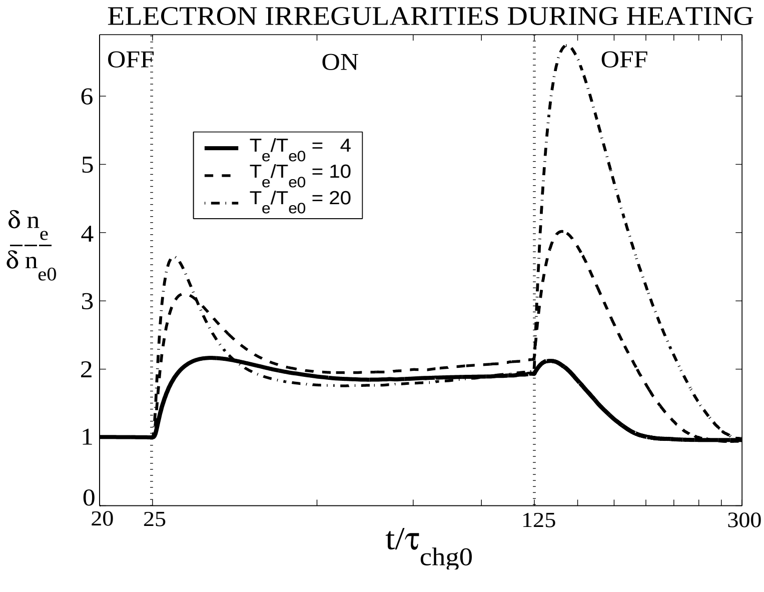

Figure 3.11: The time evolution of electron irregularities during radio wave heating with varying heating temperatures.

3.7 Discrete Charging Effects On Irregularity Evolution

A fundamental characteristic of the plasma is its ability to shield out electric potentials that are applied to it for the majority of the plasma. A measure of the plasma shielding is called the Debye length $\lambda_D = \sqrt{\frac{\epsilon_0 K T_e}{n q_e^2}}$, which is a measure of the shielding distance. Here, the background plasma is called quasineutral gas which means that its neutral enough to assume $n_i = n_e = n$ where n is the plasma density. Assume the electron density at PMSE layer $n_e = 10^{10}\ 1/m^3$ and electron temperature $T_e = 150$ k, then the Debye length $\lambda_D \approx 1$ cm.

Using the OML discrete charging models mentioned in previous sections, assume the electron irregularity wavelength equal to 4 m (f = 30 MHz), the dust radius equal to 10 nm, then, for 10% dust particles, we could get the dust charging rate $f_c \approx 5.1113 * 10^{-5}$ 1/s at the equilibrium and $f_c \approx 1$ 1/s at the initialization of the dust charging. Applying the typical electron thermal velocity $v_{te} = 10^5$ m/s, then the charging mean free path can be calculated as $L_c = v_{te}/f_c \approx 2 \times 10^9$ m at the equilibrium and 10^5 m at the initialization. For 5% dust density, the charging rate is $f_c = 3.6 * 10^{-5}$ 1/s at the equilibrium, and the corresponding mean free path is 2.8×10^9 m. Additionally, the electron-neutral collision frequency could be calculated as: $\nu_{en} = 5.4 \times 10^{-10} n_n {T_e}^{1/2} = 3.85$ 1/s, therefore, the collision mean free path will be around 1.3×10^5 m.

The dust floating potential at equilibrium ${\phi_d}^{eq}$ can be calculated from $I_e + I_i = 0$ as discussed earlier. Also, it is mentioned in the previous sections, (e.g. Section 2.6) the electron charge number Z_d is defined as $Z_\mathrm{d} = 4\pi\varepsilon_0 r_\mathrm{d} {\phi_d}^{eq}/q_e \approx 1$. This indicates that typically, there is only one electron charged on a single 10 nm radii dust particle. This is also proved from the simulation results (See Figure 8.2 in Appendix C.). Assume the electron irregularity wavelength equals to 4 m (f = 30 MHz), the dust radius equal to 10 nm, then, for 10% dust particles, the simulation results show that the average charged electron numbers on the dust particles are 1.1945 at the equilibrium. For 5% dust density, the charge number will be 1.3455.

Since there is only one electron charged on the dust particle, the use of a continuous charging model may certainly be brought into question. In this work, we proposed a new discrete charging model, the results will be compared with the previous continuous model to verify the validation of the theories which is based on continuous model.

3.7.1 Discrete Charging Model

When a dust particle is immersed in a plasma, it will gradually charge up by collecting electron and ion currents. In previous work [*Chen and Scales* 2005; *Scales,* 2004], the dust charge is determined from the standard continuous charging model which is given by [*Shukla and Manun,* 2002]

$$\frac{dQ_{\mathrm{d}}}{dt} = I_{\mathrm{e}} + I_{\mathrm{i}} \tag{3.22}$$

where I_{e} and I_{i} are the currents onto each individual dust particle by electron and ion flux. Note photoemission and other charging currents have been neglected[*Havnes et al.,* 2003].

The temporal evolution of the charge $Q_{\mathrm{d}}(t)$ can be found by integrating (3.22), using suitable expressions for the currents I_α, where $\alpha =$ e or i. The charging current expression adopted here is the Orbital-Motion-Limited (OML) approach [*Bernstein and Rabinowitz,* 1959]. For negatively charged dust, which will primarily be considered, these currents are given by

$$I_{\mathrm{e}} = \sqrt{8\pi} r_{\mathrm{d}}^2 q_{\mathrm{e}} n_{\mathrm{e}} v_{\mathrm{te}} \exp(-q_{\mathrm{e}}\phi_{\mathrm{d}}/KT_{\mathrm{e}}) \tag{3.23}$$

$$I_{\mathrm{i}} = \sqrt{8\pi} r_{\mathrm{d}}^2 q_{\mathrm{i}} n_{\mathrm{i}} v_{\mathrm{ti}} (1 - q_{\mathrm{i}}\phi_{\mathrm{d}}/KT_{\mathrm{i}}). \tag{3.24}$$

However, this process neglects the fact that the electron and ion currents collected by the grain actually consist of individual electrons and ions.

Due to the relatively small size of the dust grains ($r_{\mathrm{d}} \sim 10$ nm) in the PMSE generation layer, they are expected to carry no more than a few charges. The natural physical charging process is discrete and statistical. Therefore, based on previous works [*Cui and Goree* 1994; *Scales* 2004], a more accurate approach that includes the effect of discrete charges is now developed.

The probabilities of ion and electron attachments will be a key aspect of the collection of discrete plasma particles (ions and electrons) that are identified and incorporated into the model. The attachment of either ions or electrons will not be random, they obey probabilities that depend on the dust grain potential ϕ_{d}

Define $p_{\mathrm{e}}(\phi_{\mathrm{d}})$ and $p_{\mathrm{i}}(\phi_{\mathrm{d}})$ as the electron or ion attachment rates respectively. p_{i} will decrease with ϕ_{d}, and p_{e} will increase. $p_{\mathrm{e}}(\phi_{\mathrm{d}})$ and $p_{\mathrm{i}}(\phi_{\mathrm{d}})$ are calculated from the OML currents $I_{\mathrm{e}}(\phi_{\mathrm{d}})$ and $I_{\mathrm{i}}(\phi_{\mathrm{d}})$ in (3.23) and (3.24) as

$$p_\alpha = I_\alpha / q_\alpha \tag{3.25}$$

This equation converts the OML currents (3.23), (3.24) into attachment rates, furthermore, it will relate the discrete charging model with its probabilities to the continuous charging model with its current. It is the key to developing the discrete charging model. Both $p_{\rm e}(\phi_{\rm d})$ and $p_{\rm i}(\phi_{\rm d})$ will be calculated each time step during the simulation. They will be used to calculate the probabilities of both ion and electron attachments for a given time interval dt:

$$P_\alpha = 1 - \exp(-dt \cdot p_\alpha) \tag{3.26}$$

The probability P_α will then decide the attachments of ions or electrons to one dust grain at the corresponding time. It is noted that there are other charing models other than OML charging model. This will be covered in Appendix.

For each dust grain, during each time step of the simulation, there will be two uniform random numbers generated, $R_{\rm i}$ and $R_{\rm e}$, where $0 < R_\alpha < 1$, (α = e or i). They are compared with the ion and electron attachments probabilities. If $R_\alpha < P_\alpha$, then the plasma species will be collected by the dust grain and the corresponding dust charge number will be changed.

It should be noted that the PIC method is used in this model, therefore, the above algorithm is easily embedded into the model. Also, it is useful to consider other possible expressions for the ion and electron attachment rates [*Natanson,* 1960; *Draine et al.,* 1987]. Those have been tested and show very similar results. Details of the comparisons will be the subject of a future work.

3.7.2 Discrete Charging Effects Analysis

During the turn-on of the radio wave, the physics is primarily driven by the electron diffusion and charging behavior. During turn-off of the radio wave, the physics is primarily driven by the ion diffusion and charging behavior. The charging time scale τ_c is:

$$\tau_c = \frac{e}{|\langle I_{\rm e} + I_{\rm i}\rangle|} \geq \frac{1}{\sqrt{8\pi} n_{\rm e} v_{\rm te} \langle r_{\rm d}^2\rangle} \sim 1 \text{ sec.} \tag{3.27}$$

where $\langle\cdot\rangle$ indicates the average over all the dust particles in the simulation. Of course, the charging time varies significantly during the heating cycle.

$\tau_{\rm df}$, the ambipolar diffusion time scale, is given by

$$\tau_{\rm d} \approx \left(\frac{\lambda}{2\pi}\right)^2 \left(\frac{KT_{\rm i}}{m_{\rm i}\nu_{\rm in}}\left(1 + \frac{T_{\rm e}}{T_{\rm i}}\right)\left(1 + \frac{Z_{\rm d0}n_{\rm d0}}{n_{\rm e0}}\right)\right)^{-1} \tag{3.28}$$

where $Z_{\rm d0}, n_{\rm d0}$, and $n_{\rm e0}$ are background values of the dust charge number, dust number density, and electron number density which may vary in time due to dust charging. As an example, considering a radar frequency of 50MHz, the equivalent Bragg scattering wavelength is approximately 3 meters, and $\tau_{\rm d} \approx 1$ sec.. This means at this frequency, the charging time and diffusion time are approximately equal to each other.

The scale size of the electron irregularities in the PMSE generation layer (and therefore the observing radar frequency) is of course an important factor in determining the temporal behavior since the irregularity scale size is intimately related to the diffusion rate. For smaller scale irregularities (higher radar frequencies) diffusion effects are dominant over charging. For larger scale irregularities (lower radar frequencies) charging is dominant over diffusion effects. Previous work predicted that the temporal behavior of the irregularities depends on the ratio of the electron-ion ambipolar diffusion time to the dust particle charging time τ_d/τ_c[*Chen and Scales* 2005]. The ratio depends on irregularity scale-size, which is half of the radar wavelength. Thus, the discrete charging on different scale-size irregularities during heating will be studied first.

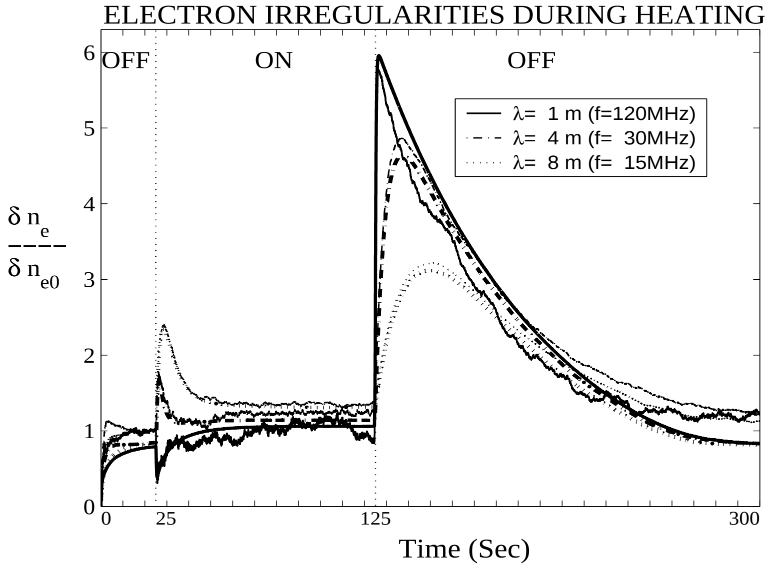

Figure 3.12: The time evolution of electron irregularities during radio wave heating with varying electron irregularity scale size (and radar frequency). Both discrete and continuous model results are shown.

Figure 3.12 compares the relative electron irregularity evolution for a variation in scale-size for $\lambda = 1$, 4, and 8 meters. The approximate corresponding radar frequencies are also shown. The whole simulation lasts 300 seconds. Both continuous and discrete charging model results are plotted. Note the discrete charging model results tend to fluctuate about the smooth curves. The irregularities can be seen to grow from zero amplitude to a steady state equilibrium by time = 25 seconds when the heating is turned 'on'. At 25 seconds, $T_\mathrm{e}/T_\mathrm{i}$ is increased from 1 to 10 in a time much less than 1 second. The electron temperature is held at this constant value until time =125. At this time, the system has reached an approximate equilibrium state again. At 125 seconds, $T_{\mathrm{e}}/T_{\mathrm{i}}$ is reduced back to 1 in a time much less than one second and the system approaches its initial state. The simulation is terminated at time = 300 seconds. There are several interesting facts about the differences between these two models for varying radar frequencies. Firstly, the discrete model shows very similar behavior with the continuous models during the whole simulation. They are quite close for both of the turn-on and turn-off overshoot. Furthermore, Figure 3.12. shows that before and after the heater is on, the discrete model's irregularity amplitude is higher than the continuous one. The two models are very close during the heating. In another words, the difference between the two models are smaller during the heating period. This is easy to understand. When the electron temperature is higher, the dust particles will be charged more, which increases the validity of continuous charging model. Moreover, all discrete model curves are less smooth during the heating. Since the electron temperature is higher during the heating, the attachment of electrons and ions are more random, therefore, there are more fluctuations in the electron irregularity. However, Figure 3.12. still shows that these models show reasonably similar behavior for both 'turn-on' and 'turn-off' overshoot effects. So the theory about the overshoot effects is still valid.

The difference between the discrete charging model and the continuous charging model is expected to be sensitive to the dust radii r_{d}. The continuous model is more valid for larger dust radii and therefore the models are expected to be in closer agreement for larger dust radii. How sensitive it will be is studied by comparing these two models using 4 different dust radii from 10 nm to 40 nm. The comparison of the time evolution of the irregularity amplitude for different dust radii is shown in Figure 3.13. Figure 3.13 shows that the difference between the models is more significant for the smaller dust particles, and also the discrete model exhibits more fluctuations. When the dusty plasma reaches equilibrium before heating at 100 second, $\frac{\delta n_{\mathrm{e}}}{\delta n_{\mathrm{e0}}}$ is about 30% larger for the discrete model compared to the continuous model for the case dust radius $r_{\mathrm{d}} = 10$ nm , where it is only about 5% for the case of $r_{\mathrm{d}} = 40$ nm. Note that for large dust radii, the turn-off overshoot effect is suppressed as expected [*Chen and Scales* 2005].

Another factor that should be considered is the dust density. Intuitively, higher dust density will decrease the difference between the models. This is because when dust density is larger, more electrons will be attached to dust and this will lead to a smaller charging current. Smaller charging currents will suppress the fluctuations. Figure 3.14 shows the comparison of temporal evolution of the electron irregularities for varying dust densities 1%, 10% and 50%. Very similar behavior is shown between the two models for all different dust densities. The higher dust density cases do show smaller differences and less fluctuation. However, the 'Turn-On'and 'Turn-Off' overshoots still exist. Noted that when the dust density is large, 50% for example, where

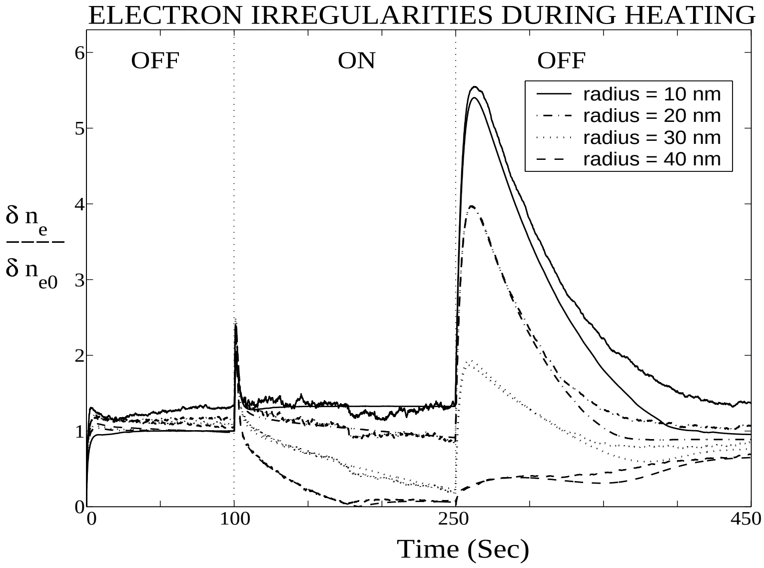

Figure 3.13: The time evolution of electron irregularities during radio wave heating with varying dust sizes. Both discrete and continuous model results are shown.

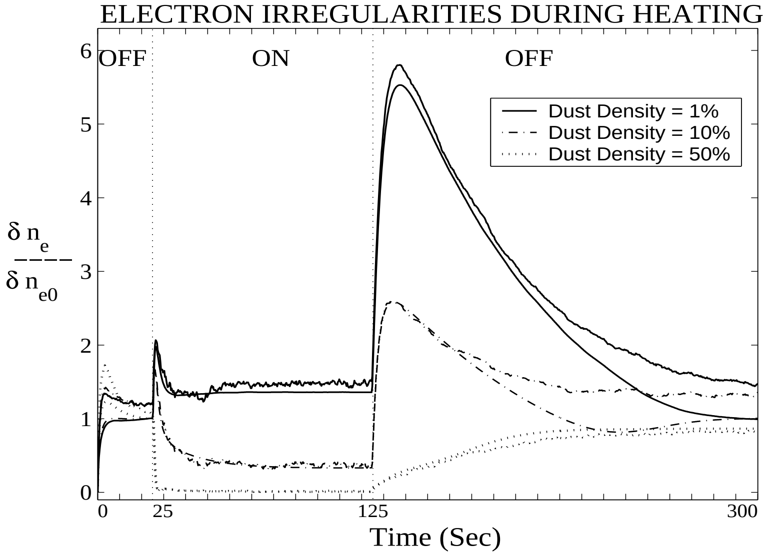

Figure 3.14: The time evolution of electron irregularities during radio wave heating with varying dust densities. Both discrete and continuous model results are shown.

will be neither turn-on nor turn-off overshoots. This is because the high dust density depletes most of the electrons [*Chen and Scales* 2005].

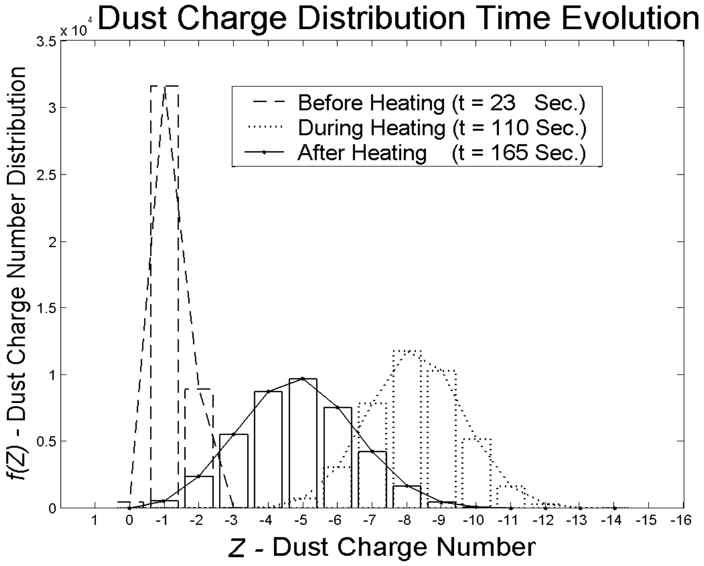

Figure 3.15: Time evolution of dust charge number distributions for Fig. 3.14 1% dust density case.

The difference between the discrete model and continuous model comes from the distribution of the dust charges. Figure 3.15 shows the evolution of the dust charge number distribution in the form of a histogram for three different times during the simulation of Figure 3.14 with 1% dust density. The envelop is also shown. The dashed lines represents the equilibrium dust charge number distribution in the equilibrium state before the heating (t = 23 seconds), primarily with each dust grain carrying one electron. Note some dust grains have 2 electrons. The dotted lines furthest to the right represent the charge distributions during the heating (t = 110 seconds). The electron temperature increases rapidly during this period of time, therefore, more electrons will attach on to the dust particles. The envelop is a Gaussian-like shape distribution, and the mean is about 8 electrons. Then, after turning the heater off, the distributions recover back to the original state. The solid curves show this transition (t = 165 seconds). The χ^2 tests were used to examine how close these charge distribution curves behaved like Gaussian distributions. The tests show that the χ^2 value is smaller during the heating, and larger before and after the heating. This implies the charge number distribution is more Gaussian during the heating, when the electron temperature is higher. It is observed that when the dust charge number distributions are more close to Gaussian distribution, the smaller differences between the discrete model and the continuous model. The χ^2 tests also show that for larger dust radius or higher dust densities, the χ^2 value is smaller, which implies more Gaussian-like behavior. This is consistent with what is observed in Figure 3.13 and Figure 3.14, where the difference between the two models is more significant for small dust radii and lower dust density.

3.8 Conclusion

This Chapter provided a physical model for the exploration of temporal behavior of the Earth's summer mesosphere electron irregularities during powerful radio wave heating. The work here investigated the relative importance of dust charging and diffusing processes during the heating. A "Turn-on Overshoot" has been predicted during PMSE modification here and the phenomenon should be more pronounced at lower observing radar frequencies. (Near or below 50 MHz) and/or for larger dust sizes. On the other hand, the "turn-off overshoot" which has been predicted and observed previously, should be more pronounced at higher observing radar frequencies and/or for smaller dust radii. Under certain conditions, the turn-on overshoot could be as prominent as the turn-off overshoot. Both overshoot phenomena are expected to provide useful information about the dust layer. Therefore the temporal evolution of the electron irregularities during radio wave heating may allow opportunity for more efficient testing of dust charging models in this case.

Chapter 4

Analytical Model

It is clear from past work that the temporal evolution during the initial perturbation of mesospheric dust associated electron irregularities has not been exploited to the fullest. Potential exists for diagnostics of the dust layer and interpretation of physical processes associated with PMSEs which are considered a forefront issue in upper atmospheric space science. The objective of this work is to consider development of approximate analytical models that may shed light on the physical processes during the initial perturbation of the irregularities. These may lead to diagnostic capabilities. Past computational work will be used as a reference.

Similar as Figure 3.4, Figure 4.1 shows the temporal evolution of electron irregularities during radio wave heating predicted by the model. Parameters are typical of the mesosphere at 85km as described in Chapter 3 with $n_{\mathrm{e}} \sim 10^{10}$ m^{-3} and $T_{\mathrm{e}} \approx 150°$ K. The ions are approximately fifty proton mass units and $\nu_{\mathrm{in}} \sim 10^{5}$ s^{-1}. The dust density is 5% of the background plasma density and the dust radius is of order 10 nm to allow an equilibrium dust charge of one electron, $Z_{\mathrm{eq}} = 1$, before heating. The irregularity amplitude in the neutral dust density $\delta n_{\mathrm{d0}}/n_{\mathrm{d0}} = 0.2$. The radio wave heating is 'turned on' at t=25 seconds as an instantaneous increase in the electron temperature. The electron temperature is increased by a factor of 5. The electron temperature is 'turned off' at time t=125 seconds. The temporal evolution is shown for varying irregularity scale sizes which correspond to varying observing radar frequencies assuming an appropriate Bragg scattering wavelength. It is observed that at smaller irregularity spatial scales (higher radar frequencies) a significant enhancement of the electron irregularity amplitude occurs when the radio wave is turned off at 125 seconds. The corresponding enhancement in radar echo is known as 'PMSE overshoot'. The overshoot ultimately results since ambipolar diffusion is more rapid than discharging during the turn-off of the radio wave. This phenomenon has been theoretically predicted as well as experimentally observed and studied in a number of past works (eg.[*Havnes* 2003,2004; *Biebricher et al.,* 2005]). Also, it has been shown that diagnostic information can be obtained from this unique temporal behavior. It can also be seen in Figure 4.1 that during the turn-on of the radio wave

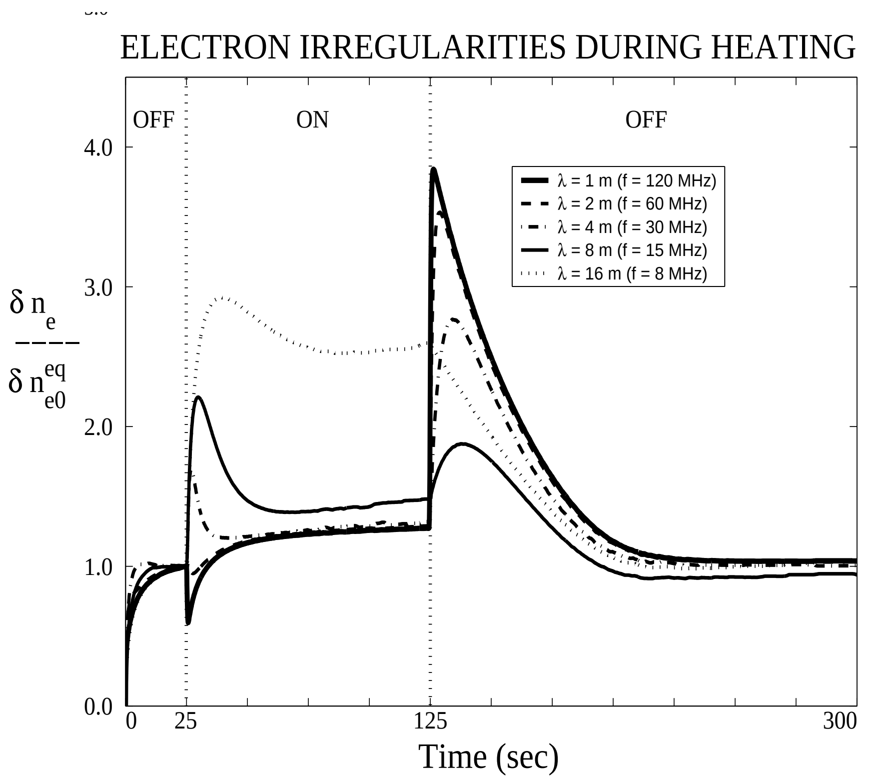

Figure 4.1: The time evolution of electron irregularities during radio wave heating with varying irregularity scale size (and radar frequency) utilizing the computational model. The heating is turned on at 25 s and off at 125 s.

for longer irregularity spatial scales (lower radar frequencies), an enhancement can also be observed during the turn-on of the radio wave. This effect was first predicted by the earlier work of [*Scales* 2004] as well as [*Chen and Scales* 2005]. The relative importance of the turn-on and turn-off overshoots was described in the later work as being related to the ratio of the ambipolar diffusion time to the dust charging time $\tau_\mathrm{d}/\tau_\mathrm{c}$. For $\tau_\mathrm{d}/\tau_\mathrm{c} \ll 1$ the turn-off overshoot is generally expected to be present and for $\tau_\mathrm{d}/\tau_\mathrm{c} \gg 1$ the turn-on overshoot is generally expected to be present.

It should be noted that parameters besides frequency that also have important effects on the temporal evolution as shown in Figure 4.1 include the dust density relative to the background plasma density and the degree of temperature enhancement during heating [*Chen and Scales* 2005]. Both of the overshoot effects are suppressed with high dust densities approaching 50% or more of the background plasma frequency. Such high dust densities may produce so-called 'bite-outs' which are large reductions in the background electron density. The associated rapid charging and low electron densities inhibit the overshoots from developing. Reducing the temperature enhancement to be less than 5 as used in Figure 4.1, reduces the amplitude of the overshoots and ultimately makes them less prominent. Varying the amplitude of the dust irregularities so $0.1 < \delta n_{d0}/n_\mathrm{d0} < 0.5$ does not significantly alter the temporal evolution of the normalized electron irregularity amplitude as shown in Figure 4.1. However, larger dust irregularity amplitudes result in larger electron irregularity amplitudes and therefore the absolute values are appropriately scaled.

4.1 Analytical Model for Turn-On Overshoot

In general, the temporal behavior of the electron irregularities during the turn-on of the radio wave has not been exploited to the fullest potential to obtain information about the dust layer. Utilizing the previous computational model, approximate analytical models will now be developed to consider possible diagnostic information during the turn-on of the radio wave and initial heating by the radio wave.

During the initial turn-on of the radio wave, the electron density can be approximately modelled as a diffusion equation with a term that corresponds to reduction of the electron density due to dust charging. This expression is given by

$$\frac{\partial n_\mathrm{e}}{\partial t} + D_\mathrm{a}\frac{\partial^2 n_\mathrm{e}}{\partial x^2} = -k n_\mathrm{d} n_\mathrm{e}. \tag{4.1}$$

Here $D_\mathrm{a} \approx KT_\mathrm{i}/m_\mathrm{i}\nu_\mathrm{in}\left(1 + T_\mathrm{e}/T_\mathrm{i}\right)\left(1 + Z_\mathrm{d0}n_\mathrm{d0}/n_\mathrm{e0}\right)$ is the ambipolar diffusion coefficient with Z_d0 the undisturbed number of charges on the dust grains. The rate coefficient for attachment of electrons onto the dust at the initial turn-on of the radio wave is approximated with the electron charging current in equation (3.4) as

$k \approx I_\mathrm{e}/(en_\mathrm{e}) = \sqrt{8\pi} r_\mathrm{d}^2 v_\mathrm{te0} \sqrt{r_\mathrm{h}} \exp(-4.1/r_\mathrm{h})$. Here r_h is the ratio of the electron temperature during and before the radio wave heating is turned on. The constant -4.1 provides a description of the equilibrium normalized floating potential on the dust prior to the radio wave heating, i.e. $e\phi/KT_\mathrm{e0}$ [*Chen and Scales,* 2005].

The temporal variation of the electron density at a fixed spatial point (recalling the dust density is stationary) can be described by the solution

$$n_\mathrm{e}(t) = n_\mathrm{e0} e^{-kn_\mathrm{d}t} e^{-t/\tau_\mathrm{d}} \tag{4.2}$$

where $\tau_\mathrm{d} \approx (\lambda/2\pi)^2/D_\mathrm{a}$ is the ambipolar diffusion time and λ is the irregularity scale size.
From equation (4.2) the electron irregularity temporal evolution can then be written as

$$\delta n_\mathrm{e}(t) = (n_\mathrm{e0} + \delta n_\mathrm{e0}) e^{-k(n_\mathrm{d0} - \delta n_\mathrm{d0})t} e^{-t/\tau_\mathrm{d}} - n_\mathrm{e0} e^{-kn_\mathrm{d0}t} e^{-t/\tau_\mathrm{d}} \tag{4.3}$$

where both the initial electron and dust densities have been written of the form $n_0 + \delta n_0$ which represents the background and perturbation components respectively. The preceding form can be simplified to

$$\widetilde{\delta n}_\mathrm{e}(t) = e^{-(1/\tau_\mathrm{r} + 1/\tau_\mathrm{d})t} [e^{\widetilde{\delta n}_\mathrm{d0} t/\tau_\mathrm{r}} (1 + \widetilde{\delta n}_\mathrm{e0}) - 1] \tag{4.4}$$

where in general $\widetilde{\delta n} = \delta n/n$ is the normalized irregularity amplitude. The reduction rate of the electron density due to the electron dust charging is denoted by $\tau_\mathrm{r} = 1/kn_\mathrm{d0}$. It is noted that this rate is related to the initial dust charging rate by $\tau_\mathrm{r} = \tau_\mathrm{c}(n_\mathrm{e}/n_\mathrm{d})$. Prior to radio wave heating, the charging time onto uncharged dust $\tau_\mathrm{c} \sim 1$ second for the parameters stated. Also, for irregularities observed in the 50 MHz range $\tau_\mathrm{d} \sim 1$ second. Of course these time scales may vary significantly during the radio wave heating and the ratio $\tau_\mathrm{c}/\tau_\mathrm{d}$, which is most important for determining the temporal evolution, may be greater or less than one.

The approximate analytical model can be used to investigate the behavior of the evolution of the dust associated electron irregularities at the initial turn-on of the radio waves. The condition for no enhancement of the electron irregularity after turn-on of the radio wave (i.e. no 'turn-on overshoot') can be obtained from the condition $\partial \widetilde{\delta n}_\mathrm{e}/\partial t < 0$ for all t which yields the condition

$$\frac{\tau_\mathrm{r}}{\tau_\mathrm{d}} > (1 + \frac{1}{\widetilde{\delta n}_\mathrm{e0}}) \widetilde{\delta n}_\mathrm{d0} - 1 \approx \frac{\widetilde{\delta n}_\mathrm{d0}}{\widetilde{\delta n}_\mathrm{e0}}. \tag{4.5}$$

The later approximation in (4.5) assumes relatively low dust density so $\widetilde{\delta n}_\mathrm{e0}/\widetilde{\delta n}_\mathrm{d0} \ll 1$. Note that this quantitative condition provides a lower diagnostic bound on the ratio of the electron density reduction to ambipolar diffusion rate ratio and is reminiscent of the more qualitative conditions discussed in previous work for the existence of the turn-on and turn-off overshoots [*Chen and Scales,* 2005]. This bound can be used to provide diagnostic information on such quantities as dust density, dust radius, and electron temperature increase through the functional dependencies of τ_{d} and τ_{r}, as well as the relative dust and electron irregularity levels.

Figure 4.2 shows comparisons of the computational model described in the previous subsection and the approximate analytical model of equation (4.4) for varying electron irregularity scale size. Note it is not the objective here to necessarily demonstrate close agreement between the two models but rather to use the much more accurate computational model to validate important qualitative temporal behavior predicted by the approximate analytical model. The analytical model in (4.4) is expected to have reasonable validity for a few tenths of seconds after the radio wave heating is turned on. For longer time periods, nonlinearities due to the temperature increase become important as can be seen in the full computational model. The plasma and dust parameters used for the comparisons are the same as used in Figure 4.1. The temporal evolution of the irregularity is shown right after the turn-on of the radio wave at 25 seconds. As described in the previous chapter, the computational model predicts enhancement in the electron irregularity for sufficiently large irregularity scale sizes. The results for the computational model are presented as the thin curves and the corresponding analytical model result is shown as the thick curves. It can be seen the agreement is quite reasonable with the approximate analytical model during the turn-on period. It can be seen that for the 4 meter irregularity case, there is an increase in the irregularity amplitude after the turn-on of the radio wave. Again this is the turn-on overshoot effect [*Chen and Scales,* 2005] which occurs when the charging process is sufficiently rapid in comparison to diffusion. The 2 and 1 meter irregularity cases produce a decrease in irregularity amplitude after the turn-on of the radio wave, i.e. no turn-on overshoot effect. It can be seen that equation (4.5) predicts this suppression of the turn-on overshoot quite well in the full computational model. For the cases $\lambda = 1,\ 2$, and 4 meters, $\widetilde{\delta n}_{\mathrm{e0}} \approx 0.0049,\ 0.0051$, and 0.0058, respectively, while $\widetilde{\delta n}_{\mathrm{d0}} = 0.2$. These values imply the right hand side of (4.5) to be approximately 41, 39, and 34, respectively. The calculated ratio $\tau_{\mathrm{r}}/\tau_{\mathrm{d}} \approx 221,\ 55$, and 13 compared to the right hand side of (4.5). It is observed that the 'turn-on' overshoot is suppressed for the 1 and 2 meter irregularity cases as expected while the 4 meter irregularity scale size does in fact exhibit this temporal behavior. Therefore it is seen that diagnostic information can be obtained from this signature in temporal behavior after the turn-on of the radio wave.

The temporal behavior of the electron irregularities after the initial turn-on and continued heating can also be used for diagnostic information. Assuming the condition holds for no initial enhancement of the electron irregularities in equation (4.5), there will be a rapid reduction in electron density after the radio wave heating is turned-on.

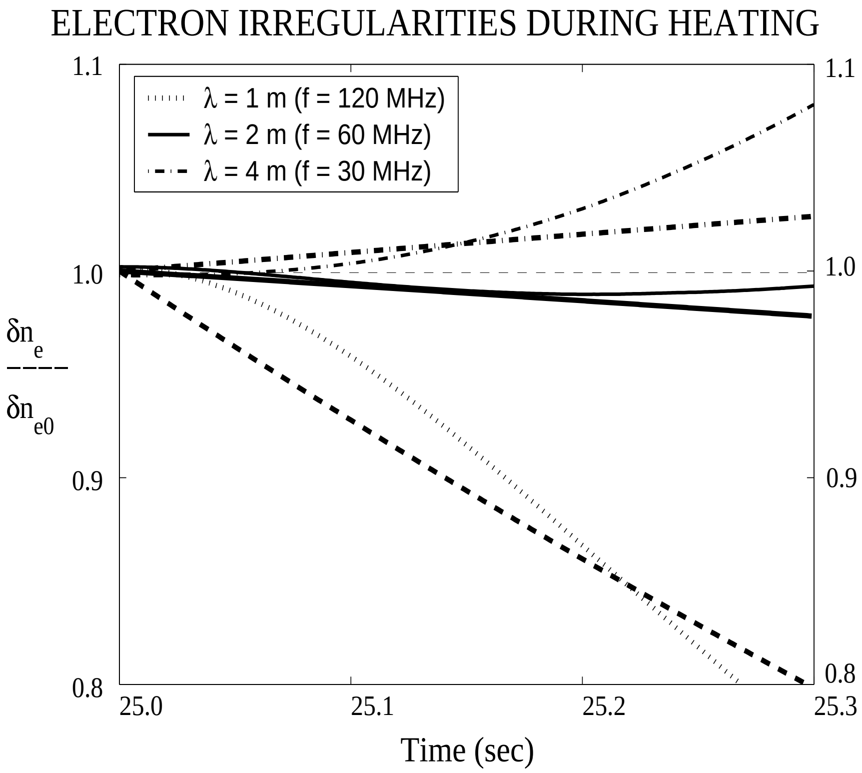

Figure 4.2: Comparison of computational (thin curves) and analytical (thick curves) models after the turn-on of radio wave heating (at $t = 25$ seconds) for varying electron irregularity scale size.

The subsequent temporal evolution can then be approximately described by equation

$$\frac{\partial n_\mathrm{e}}{\partial t} + k n_\mathrm{d} n_\mathrm{e} = 0 \tag{4.6}$$

since the diffusion processes have essentially ceased after the initial turn-on. The solution for the temporal evolution of the electron density can be written in a form similar to equation (4.) and the electron density irregularity in this case can be expressed as

$$\delta n_\mathrm{e}(t) = (n_\mathrm{e0} + \delta n_\mathrm{e0})(e^{-k(n_\mathrm{d0} - \delta n_\mathrm{d0})t} - e^{-k n_\mathrm{d0} t}). \tag{4.7}$$

Equation (4.7) can be written in terms of the electron density reduction rate τ_r in the following form

$$\widetilde{\delta n}_\mathrm{e}(t) = e^{-t/\tau_\mathrm{r}}(1 - (1 - \widetilde{\delta n}_\mathrm{e0}) e^{-\widetilde{\delta n}_\mathrm{d0} t/\tau_\mathrm{r}}). \tag{4.8}$$

From previous works [*Chen and Scales,* 2005; *Biebricher et al.,* 2005] it is observed in both experimental observations and computational models that after turn-on and for continued heating, the electron density irregularity amplitude (an corresponding radar echo strength) may increase in amplitude for certain dust density n_d and radii r_d ranges and it may decrease for certain dust radii ranges. This can be quantitatively described from the analytical model by considering where $\partial \widetilde{\delta n}_\mathrm{e}/\partial t = 0$. The condition for steady increase of the electron irregularities during continued heating is obtained as

$$t/\tau_\mathrm{r} < \frac{1}{\widetilde{\delta n}_\mathrm{d0}} \log[(1 + \widetilde{\delta n}_\mathrm{d0})(1 - \widetilde{\delta n}_\mathrm{e0})] \approx 1. \tag{4.9}$$

Physically this enhancement is due to the flux of electrons onto the dust which increases the electron irregularity amplitude. Note in this case an upper diagnostic bound can be placed on the dust density and radius since τ_r is dependent on these dust parameters. Relatively small dust densities and dust radii are required for this temporal behavior. Of course, the condition for steady decrease in electron irregularity amplitude during continued heating can be obtained as

$$t/\tau_\mathrm{r} > \frac{1}{\widetilde{\delta n}_\mathrm{d0}} \log[(1 + \widetilde{\delta n}_\mathrm{d0})(1 - \widetilde{\delta n}_\mathrm{e0})] \approx 1. \tag{4.10}$$

This places a lower diagnostic bound on the dust density and dust radius and indicates that relatively high dust densities and large dust radii are required for this temporal behavior. In this case the dust charging is so rapid that the electron irregularities are prohibited from growing.

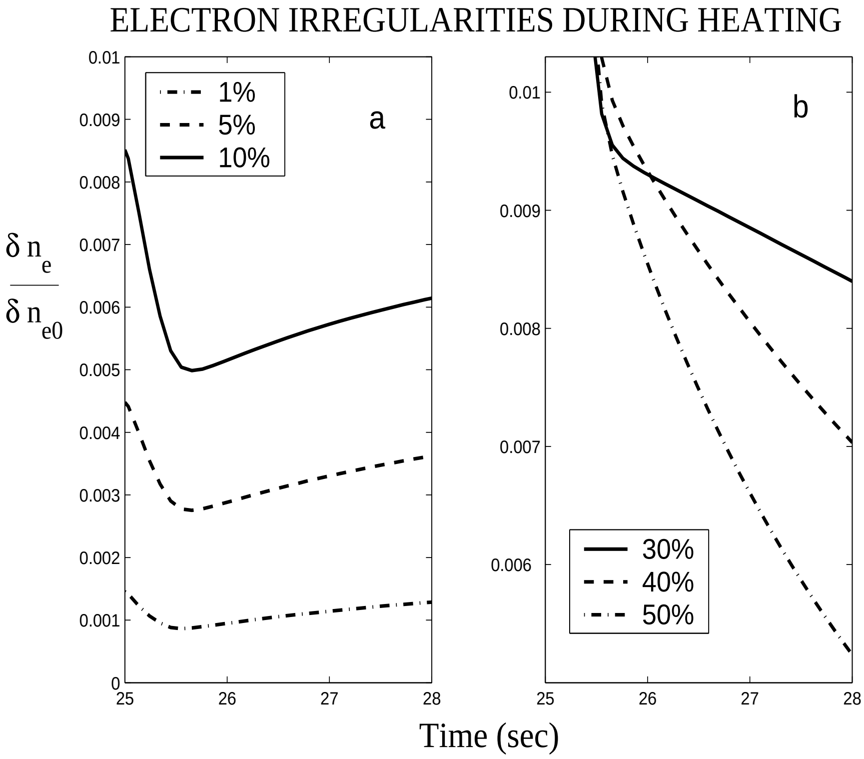

Figure 4.3: Time evolution of electron irregularities in the computational model for varying dust densities after the initial turn-on of the radio wave at $t = 25$ seconds. Note low density cases exhibit enhancement in irregularity amplitude upon continued heating and high density cases show a reduction in irregularity amplitude.

Figure 4.3 shows the results of the computational model for the temporal evolution of electron irregularities for varying dust densities. Figure 4.3a shows the case for lower dust densities 1%, 5% and 10%. In these three cases, it can be seen that after the initial reduction following the turn-on of the radio wave due to the rapid ambipolar diffusion as just described, there is a general recovery of the irregularity amplitude due to the charging. It can also be observed that there is generally a faster recovery for the higher (10%) density case for this set of parameters. Figure 4.3b shows relatively higher dust density cases with 30%, 40% and 50% dust density. It can be seen in these cases that there is a general decrease in the irregularity amplitude after the initial rapid decrease due to ambipolar diffusion which is near completion at approximately $t = 25.5$ seconds. This decrease in irregularity amplitude is more rapid for higher dust density.

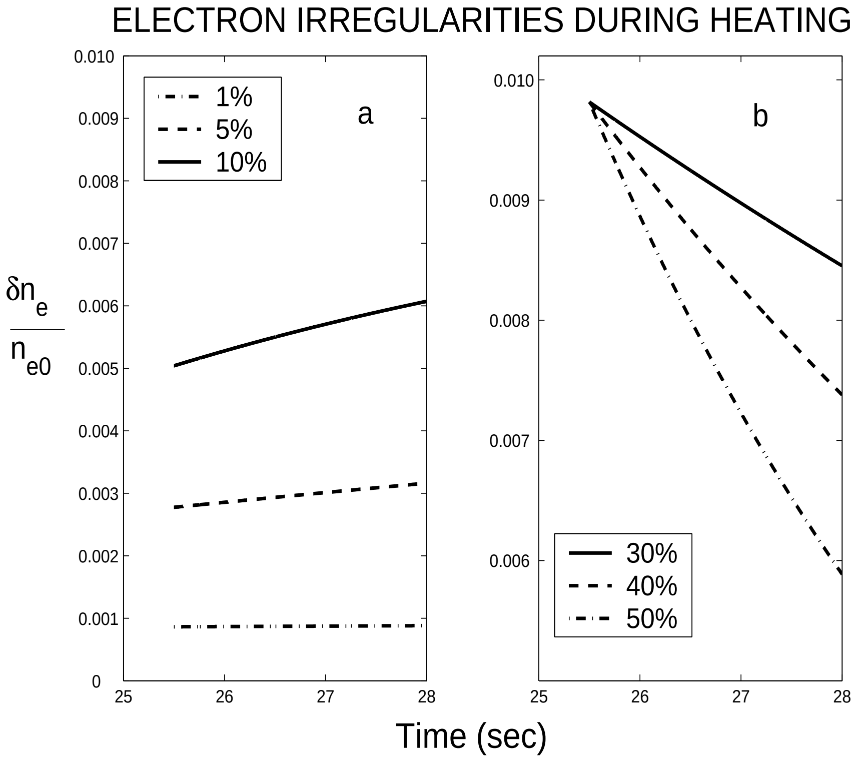

Figure 4.4: Corresponding analytical model calculations (equation (4.8)) for Figure 4.3 showing the temporal evolution of irregularities for varying dust density after turn-on of radio wave heating.

Figure 4.4 shows that the corresponding approximate analytical calculations give reasonable agreement with the full computational model results. The analytical calculations begin at $t \approx 25.5$ which is the time the ambipolar diffusion process in the computational results (Figure 4.3) are seen to have ceased. Figure 4.4a shows the low density cases. Figure 4.4b shows the high density cases. The delineation between the low and high density behavior with increase and decrease in irregularity amplitude is described by the expressions in equations (4.9) and (4.10) respectively. Therefore diagnostic information can be obtained by the temporal behavior during continued heating. It should be noted that the case shown in Figures 4.3 and 4.4 indicate how diagnostic information could be obtained on the variation in charged dust number density. Similar behavior may be expected with increasing dust radius r_{d}.

4.2 Analytical Model for Turn-Off Overshoot

The purpose of the present investigation is to consider further diagnostic information that may be obtained from the enhancement of the electron irregularities after the radio wave heating is turned off (i.e. turn-off overshoot). An understanding of the dominant physical processes that drive the irregularity temporal evolution during and after the heating process will ultimately allow greater possibilities for diagnostic information. Figure 4.5 shows the spatial variation of the irregularities in Figure 4.1 before radio wave heating (denoted equilibrium), just prior to turn off of the radio wave, and just after turn-off of the radio wave. Three different wavelengths, $\lambda = 1, 4$ and 16 meters, are shown. In each case, the irregularities are shown at $t = 24$ seconds which is the equilibrium state prior to heating. It can be seen that the ion and dust charge irregularities are out of phase with the electron irregularities in each case. For $\lambda = 1$ meter, it can be seen that after the irregularities achieve equilibrium during the heating prior to turn-off at $t = 124$ seconds, there is a large enhancement in the ion irregularity amplitude which ultimately results from ambipolar diffusion. The ion irregularity amplitude is significantly larger than the electron irregularity amplitude which also shows some enhancement due to the electron charging flux onto the dust. The dust charge irregularity is in turn enhanced due to the increased charge state of the dust grains from the electron charging. After the radio wave heating at $t = 126$ seconds, the electron irregularity amplitude is enhanced (i.e. turn-off overshoot) by approximately a factor of 3. There is a reduction in the ion irregularity amplitude as well, however, there is little change in the dust charge irregularity amplitude due to the relatively slow discharging due to the small ion flux onto the dust. It is ambipolar diffusion that reduces the large ion irregularity gradients and correspondingly enhances the gradients in the electron irregularities after turn-off of the radio wave. The case for $\lambda = 4$ meters shows relatively similar behavior to the case with $\lambda = 1$. The ambipolar diffusion is slower in this case due to the longer wavelength. It can be seen after the turn-off of the heating that the enhancement in the electron irregularities is smaller and roughly a factor of 2 as compared to 3 for $\lambda = 1$ meter. For the longest wavelength case, $\lambda = 16$ meters, there is a much smaller ion irregularity produced both prior and during heating due to the increased ambipolar diffusion time [*LieSvenson et al.,* 2003]. It is observed that there is little change in the ion irregularity amplitude after turn-off of the radio wave due to reduced ambipolar diffusion effects and consequently no enhancement in the electron irregularities after the turn-off of the radio wave.

The relationship between the electron, ion and dust irregularities can be described from a perturbation analysis [*Chen*, 1984]. For the case of shorter wavelength irregularities (1 and 4 meter) in Figure 4.5, ambipolar diffusion time is sufficiently small so the electrons and ions may be modelled with the Boltzmann approximation. This implies the normalized electron and ion irregularity amplitudes, $\tilde{\delta n}_{\mathrm{e}} = \delta n_{\mathrm{e}}/n_{\mathrm{e}}$ and $\tilde{\delta n}_{\mathrm{i}} = \delta n_{\mathrm{i}}/n_{\mathrm{i}}$, can be written in terms of the electrostatic potential irregularity

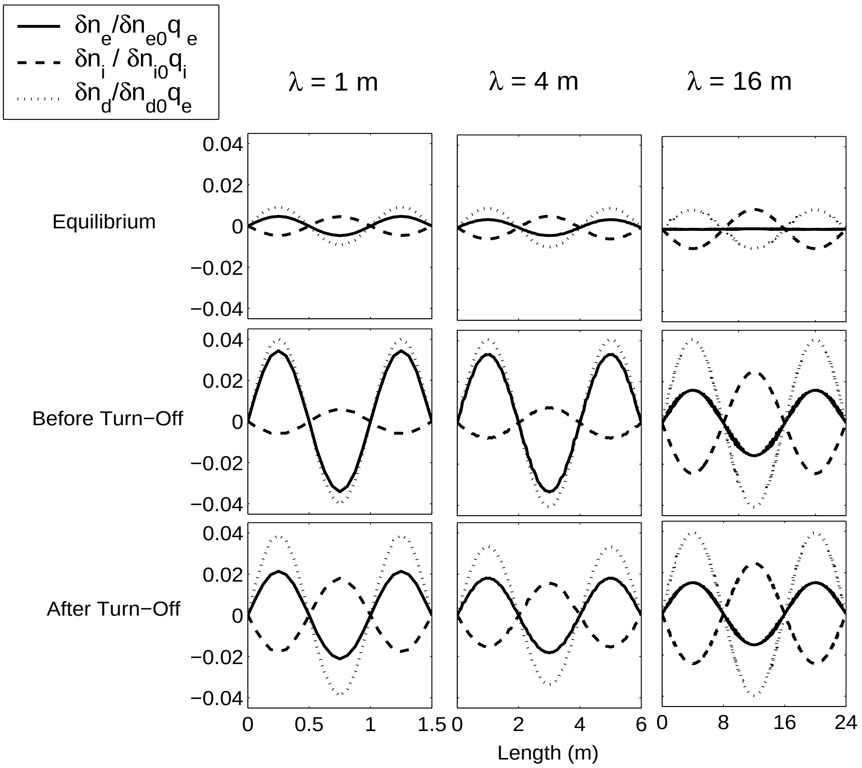

Figure 4.5: Spatial presentation of electron ($\delta\rho_\mathrm{e}/q_\mathrm{e}n_0$), ion ($\delta\rho_\mathrm{i}/q_\mathrm{i}n_0$), and dust ($\delta\rho_\mathrm{d}/q_\mathrm{e}n_0$) irregularities before, during, and after radio wave heating with varying irregularity scale size (1, 4 and 16 meters) as shown in Figure 4.1.

amplitude $\delta\phi$ as

$$\tilde{\delta n}_{\mathrm{e}} \approx -\frac{T_{\mathrm{i}}}{T_{\mathrm{e}}}\tilde{\delta n}_{\mathrm{i}} \approx \frac{e\delta\phi}{k_B T_{\mathrm{e}}}. \tag{4.11}$$

This expression indicates for sufficiently small irregularity wavelength, the electrons and ions are 180° out of phase or anti-correlated [*LieSvenson et al.,* 2003]. Also, during the radio wave heating phase, the ion irregularities are typically larger due to the electron temperature enhancement. The Poisson equation can be used to determine the relationship of the dust irregularity amplitude to the electron irregularity amplitude. In the Fourier spectral domain, the Poisson equation for the irregularities is

$$k^2\delta\phi \approx \frac{1}{\epsilon_0}(-e\delta n_{\mathrm{e}} + e\delta n_{\mathrm{i}} - eZ_{\mathrm{d}}\delta n_{\mathrm{d}}) \tag{4.12}$$

where the wavenumber is denoted by k. Note here that the dust is assumed to be negatively charged with charge number Z_{d}. This implies the relationship

$$\tilde{\delta n}_{\mathrm{e}} \approx -\frac{Z_{\mathrm{d}}n_{\mathrm{d}}}{n_{\mathrm{e}}}\frac{1}{1+\lambda_{\mathrm{De}}^2/\lambda_{\mathrm{Di}}^2+\lambda_{\mathrm{De}}^2k^2}\tilde{\delta n}_{\mathrm{d}} \tag{4.13}$$

where $\lambda_{\mathrm{De,i}}$ is the electron (ion) Debye length. Therefore the electron irregularities are also 180° out of phase with dust irregularities (which are in phase with the ion irregularities).

The previous results illuminate the relative importance of ambipolar diffusion and charging times in the temporal evolution of electron irregularities subsequent to radio wave heating. Utilizing these concepts from the previous computational results, a simplified analytical model will now be developed to consider possible diagnostic information during the turn-off of radio wave heating.

The electron density is determined from the ion and dust charge densities using quasi-neutrality. After turning off the radio wave heating, the dominant physical effects are ion density gradient driven ambipolar diffusion and discharging of the dust grains due to ion currents as described in Figure 4.5. Therefore, an analytical model for the electron density after turn-off of the radio wave heating can be written of the form [*Scales and Chen,* 2007(a)]

$$\begin{aligned} n_{\mathrm{e}}(t) &= n_{\mathrm{i}}(t) - Z_{\mathrm{d}}(t)n_{\mathrm{d}} \\ &= (n_{\mathrm{i0}} - n_{\mathrm{i0}}^{eq})e^{-k_{\mathrm{i}}n_{\mathrm{d0}}t}e^{-t/\tau_{\mathrm{d}}} + n_{\mathrm{i0}}^{eq} - [(Z_{\mathrm{d0}} - Z_{\mathrm{d0}}^{eq})e^{-k_{\mathrm{i}}n_{\mathrm{d0}}t} + Z_{\mathrm{d0}}^{eq}]n_{\mathrm{d0}} \end{aligned} \tag{4.14}$$

where now the turn-off of the radio wave is referenced to time $t = 0$. Here $\tau_{\mathrm{d}} \approx (\lambda/2\pi)^2/D_{\mathrm{a}}$ is the diffusion time which depends on the irregularity scale size λ and $D_{\mathrm{a}} \approx (KT_{\mathrm{i}}/m_{\mathrm{i}}\nu_{\mathrm{in}})\,(1+T_{\mathrm{e}}/T_{\mathrm{i}})\,(1+Z_{\mathrm{d0}}n_{\mathrm{d0}}/n_{\mathrm{e0}})$ which is the ambipolar diffusion coefficient. After the turn-off of the radio wave, the ion current onto the dust grains dominates the electron current and results in discharging of the dust grains as seen in Figure 4.5. The rate coefficient for attachment of ions onto the dust at the initial turn-off of the radio wave is approximated with the ion charging current in equation (3.5) as $k_{\mathrm{i}} \approx I_{\mathrm{i}}/(en_{\mathrm{i}}) = \sqrt{8\pi} r_{\mathrm{d}}^2 v_{\mathrm{ti0}}(1-x)$ where x is determined from the equilibrium $I_{\mathrm{e}} + I_{\mathrm{i}} = 0$ just prior to turn-off of the radio wave. It should be noted that x depends on the ratio of the electron temperature during and before the radio wave heating is turned on [*Chen and Scales,* 2005] denoted by $T_{\mathrm{e}}/T_{\mathrm{e0}}$. It is assumed in the above model that the electron irregularities have achieved steady state prior to the radio wave heating being turned off. Therefore in (4.14), n_{i0} and Z_{d0} are the steady state ion density and charge on the dust grains just prior to turning off the radio wave. The equilibrium values of the ion density and dust grain charge before heating are denoted by n_{i0}^{eq} and Z_{d0}^{eq}, respectively. Recall that the model assumes a dust density that is constant in time n_{d0} as described previously. The steady state ion density prior to turning off the radio wave can be written as $n_{\mathrm{i0}} = n_{\mathrm{e0}} + Z_{\mathrm{d0}}n_{\mathrm{d0}}$ while the equilibrium value before radio wave heating can be written as $n_{\mathrm{i0}}^{eq} = n_{\mathrm{e0}}^{eq} + Z_{\mathrm{d0}}^{eq}n_{\mathrm{d0}}$ assuming negatively charged dust. Therefore, the temporal evolution of the electron density can be rewritten as

$$n_{\mathrm{e}}(t) = e^{-k_{\mathrm{i}}n_{\mathrm{d0}}t}[(n_{\mathrm{e0}} - n_{\mathrm{e0}}^{eq})e^{-t/\tau_{\mathrm{d}}} - (Z_{\mathrm{d0}} - Z_{\mathrm{d0}}^{eq})n_{\mathrm{d0}}(1 - e^{-t/\tau_{\mathrm{d}}})] + n_{\mathrm{e0}}^{eq}. \tag{4.15}$$

Using (4.15) and noting the irregularity phases of Figure 4.5, the electron irregularity temporal evolution can then be written as

$$\begin{aligned}
\delta n_{\mathrm{e}}(t) \;&=\; e^{-k_{\mathrm{i}}n_{\mathrm{d0}}t}\Big[(n_{\mathrm{e0}} + \delta n_{\mathrm{e0}} - n_{\mathrm{e0}}^{eq} - \delta n_{\mathrm{e0}}^{eq})e^{-t/\tau_{\mathrm{d}}} \\
&-\; (Z_{\mathrm{d0}} - Z_{\mathrm{d0}}^{eq})(n_{\mathrm{d0}} - \delta n_{\mathrm{d0}}^{eq})(1 - e^{-t/\tau_{\mathrm{d}}})\Big] + n_{\mathrm{e0}}^{eq} + \delta n_{\mathrm{e0}}^{eq} \\
&-\; e^{-k_{\mathrm{i}}n_{\mathrm{d0}}t}\Big[(n_{\mathrm{e0}} - n_{\mathrm{e0}}^{eq})e^{-t/\tau_{\mathrm{d}}} - (Z_{\mathrm{d0}} - Z_{\mathrm{d0}}^{eq})n_{\mathrm{d0}}(1 - e^{-t/\tau_{\mathrm{d}}})\Big] - n_{\mathrm{e0}}^{eq}
\end{aligned} \tag{4.16}$$

where the electron and dust densities have been written of the form $n_0 + \delta n_0$ which represents the background and perturbation components, respectively. The preceding form can be simplified to

$$\Delta\tilde{\delta} n_{\mathrm{e}}(t) = e^{-t/\tau_{\mathrm{r}}}\left[e^{-t/\tau_{\mathrm{d}}} + \frac{\Delta Z_{\mathrm{d0}}\delta n_{\mathrm{d0}}}{\Delta\delta n_{\mathrm{e0}}}(1 - e^{-t/\tau_{\mathrm{d}}})\right] \tag{4.17}$$

where in $\Delta\delta n_{\rm e}(t) = \delta n_{\rm e}(t) - \delta n_{\rm e0}^{eq}$ is the difference in the electron irregularity amplitude from the equilibrium value and $\Delta\tilde{\delta} n_{\rm e}(t) = \Delta\delta n_{\rm e}(t)/\Delta\delta n_{\rm e0}$ is its value normalized to 1 at $t = 0$ where $\Delta\delta n_{\rm e0} = \delta n_{\rm e0} - \delta n_{\rm e0}^{eq}$. Also, $\Delta Z_{\rm d0} = Z_{\rm d0} - Z_{\rm d0}^{eq}$ is the net gain in electron charges during radio wave heating. The reduction time of the ion density due to the dust charging from ion flux is denoted by $\tau_{\rm r} = 1/k_{\rm i}n_{\rm d0}$. It is noted that $\tau_{\rm r}$ is related to the dust (dis)charging time after the radio wave heating is turned off by $\tau_{\rm r} = \tau_{\rm c}(n_{\rm i}/n_{\rm d})$.

The approximate analytical model in (4.17) can be used to investigate the temporal behavior of the dust associated electron irregularities subsequent to radio wave heating. The condition for an enhancement of the electron irregularities after turn-off of the radio wave (i.e. 'turn-off overshoot', (*Havnes et al.*, 2003; *Havnes*, 2004)) can be obtained from the condition $\partial(\Delta\tilde{\delta} n_{\rm e})/\partial t > 0$ for $t = 0$ which yields the condition

$$\frac{\tau_{\rm r}}{\tau_{\rm d}} > \frac{1}{\Delta Z_{\rm d0}\delta n_{\rm d0}/\Delta\delta n_{\rm e0} - 1}. \tag{4.18}$$

Note that this quantitative condition provides a lower diagnostic bound on the ratio of the ion density reduction to ambipolar diffusion time ratio and is a refined quantitative version of the more qualitative condition discussed in previous work for the existence of the turn-off overshoot [*Chen and Scales* 2005]. This bound can be used to provide diagnostic information on such quantities as dust density, dust radius, dust charge, and electron temperature increase, through the functional dependencies of $\tau_{\rm d}$ and $\tau_{\rm r}$ on these parameters as described in previous work.

The time at which the maximum amplitude is reached after the turn-off of the radio wave can be obtained from the condition $\partial(\Delta\tilde{\delta} n_{\rm e})/\partial t = 0$ as

$$\tau^{\max} \approx \tau_{\rm d} \log\left[\left(1 + \frac{\tau_{\rm r}}{\tau_{\rm d}}\right)\left(1 - \frac{\Delta\delta n_{\rm e0}}{\Delta Z_{\rm d0}\delta n_{\rm d0}}\right)\right]. \tag{4.19}$$

This expression can be used to approximate the maximum amplitude of the electron irregularities after the turn-off of the radio wave heating. Substituting (4.19) into (4.17) implies

$$\Delta\tilde{\delta} n_{\rm e}^{\max} \approx \frac{\Delta Z_{\rm d0}\delta n_{\rm d0}}{\Delta\delta n_{\rm e0}} \frac{1}{(1 + \tau_{\rm d}/\tau_{\rm r})\left[(1 + \tau_{\rm r}/\tau_{\rm d})\left(1 - \Delta\delta n_{\rm e0}/(\Delta Z_{\rm d0}\delta n_{\rm d0})\right)\right]^{\tau_{\rm d}/\tau_{\rm r}}}. \tag{4.20}$$

Assuming before heating, $T_{\rm e} \approx T_{\rm i}$, the Boltzmann approximation holds, and $k^2\lambda_{\rm De}^2 \ll 1$, then (4.13) leads to the useful approximation

$$\frac{Z_{\mathrm{d0}}\delta n_{\mathrm{d0}}}{\delta n_{\mathrm{e0}}} \approx 1 + \frac{T_{\mathrm{e}}}{T_{\mathrm{e0}}}. \tag{4.21}$$

Using the approximation in (4.21), the maximum amplitude after turn-off of the radio wave can be written in terms of the temperature enhancement $T_{\mathrm{e}}/T_{\mathrm{e0}}$ during heating as

$$\Delta\tilde{\delta n}_{\mathrm{e}}^{\max} \approx \frac{(T_{\mathrm{e}}/T_{\mathrm{e0}} + 1 - 2\tilde{\delta n}_{\mathrm{e0}}^{eq})/(1 - \tilde{\delta n}_{\mathrm{e0}}^{eq})}{(1 + \tau_{\mathrm{d}}/\tau_{\mathrm{r}})\left[(1 + \tau_{\mathrm{r}}/\tau_{\mathrm{d}})(T_{\mathrm{e}}/T_{\mathrm{e0}} - \tilde{\delta n}_{\mathrm{e0}}^{eq})/(T_{\mathrm{e}}/T_{\mathrm{e0}} + 1 - 2\tilde{\delta n}_{\mathrm{e0}}^{eq})\right]^{\tau_{\mathrm{d}}/\tau_{\mathrm{r}}}} \tag{4.22}$$

where $\tilde{\delta n}_{\mathrm{e0}}^{eq} = \delta n_{\mathrm{e0}}^{eq}/\delta n_{\mathrm{e0}}$. After the maximum value has been achieved (4.17), it can be seen that there is a decay in the amplitude of the electron irregularities. The approximate temporal behavior after the maximum is reached is given by

$$\tilde{\delta n}_{\mathrm{e}}(t) \approx \tilde{\delta n}_{\mathrm{e}}^{\max} e^{-t/\tau_{\mathrm{r}}}. \tag{4.23}$$

Therefore the timescale for the decay of the irregularities after the maximum is reached is the ion density reduction time τ_{r}. Therefore τ_{r} can also be interpreted as being related to the dust grain discharging time due to ion currents.

From the previous analysis, it can be seen that at least three characteristics of the irregularity temporal evolution after turn-off may be used for diagnostic information. They are the time at which maximum amplitude is reached, (4.19), the maximum amplitude achieved, (4.20) and (4.22), and the timescale for decay after the maximum amplitude has been reached, (4.23). It should be noted that (4.19) may also be written in terms of the temperature enhancement $T_{\mathrm{e}}/T_{\mathrm{e0}}$ using (4.21). Figure 4.6 shows a schematic of these characteristics after turn-off.

Figure 4.7 shows a comparison between the computational model of section 3.1 and the simplified analytical model (4.17). The same cases shown in Figure 4.1 are presented, however, the results are expressed in terms of $\Delta\tilde{\delta n}_{\mathrm{e}}$. It is observed that there is quite reasonable agreement between the two models considering the simplifying assumptions used and the approximations on the diffusion and charging timescales which in actuality vary in time. There is a tendency for the analytical model to slightly overestimate $\tau^{\max}$ in this regard. The suppression of the turn-off overshoot effect for $\lambda = 16$ meters is also well predicted in the analytical model from (4.18). From these results, confidence can be given for the simplified analytical model providing reasonable accuracy for diagnostic information.

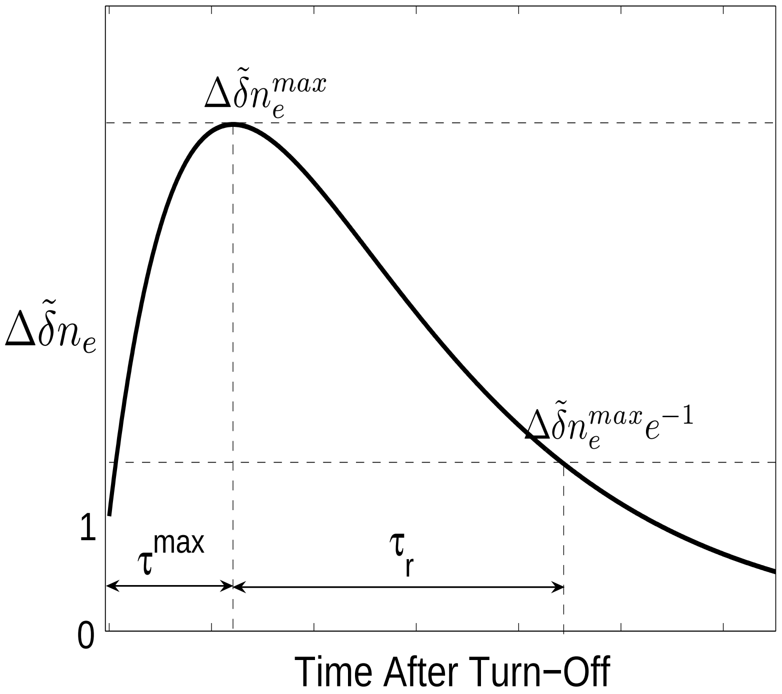

Figure 4.6: Schematic of electron irregularity behavior subsequent to radio wave heating.

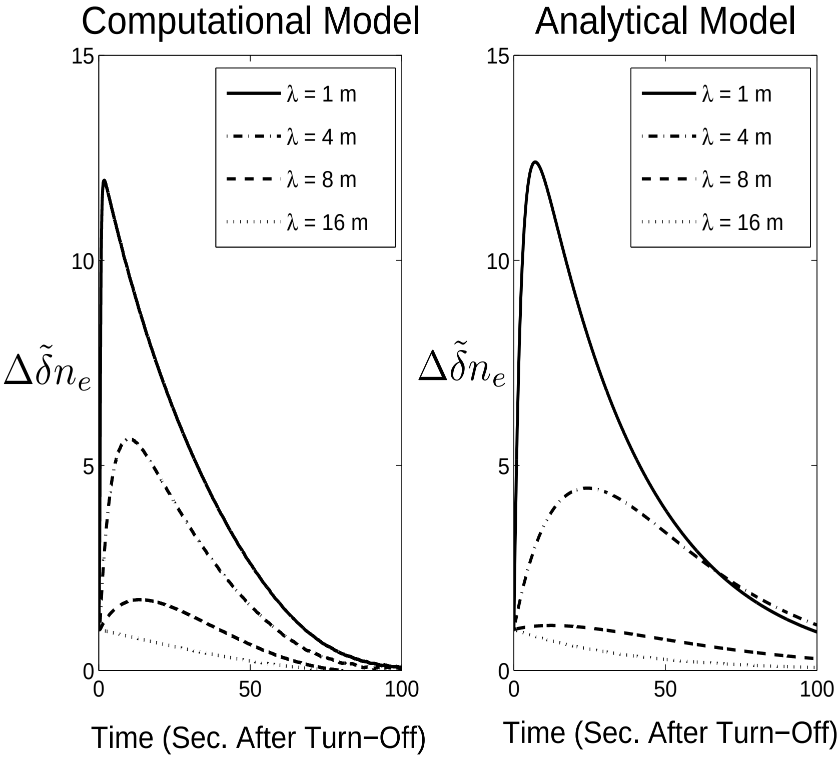

Figure 4.7: Comparison of the full computational model of section 3.1 with the analytical model (equation (4.17)) for the parameters of Figure 4.1. Note results represented in the form of $\Delta\tilde{\delta}n_\mathrm{e}$ which is the normalized electron irregularity amplitude difference from the equilibrium before heating.

4.3 Dust Diagnostics Using Overshoot Effects

Modification of PMSEs by radio wave heating is a relatively new and promising area of investigation in the earth's upper atmosphere. The overshoot effect described previously are expected to provide useful information about the dust layer in the mesopause.

It has been established in the previous sections that the ratio $\tau_{\mathrm{d}}/\tau_{\mathrm{r}}$ describes the existence of PMSE amplitude overshoot during turn-on and turn-off of radio wave heating. Diagnostics for the dust radius may be obtained from these conditions under the assumption of the validity of the continuous charging model. Since previous results indicate that dust radius distributions with the same RMS dust radius exhibit very similar electron irregularity temporal evolution during heating, the results here can be interpreted to apply to the RMS radius of the dust distribution. First it is useful to obtain approximate expressions for τ_{r} as it varies through the heating cycle. Note that $\tau_r = \tau_c(n_e/n_d)$ during the heater is on, and $\tau_r = \tau_c(n_i/n_d)$ during the heating is turning off. Since, normally, $n_e = n_i$, this diagnostics could also be represented using the ratio of τ_{d}/τ_c.

Equation 4.5 and 4.18 give the bounds of the existences of turn-on and turn-off overshoot effects respectively. Since $\tau_r = \tau_c(n_e/n_d)$ during the heater is on, a condition for obtaining turn-on overshoot in terms of τ_c will be:

$$\frac{\tau_{\mathrm{d}}}{\tau_{\mathrm{c}}} >> \frac{\widetilde{\delta n_{\mathrm{e0}}} n_{\mathrm{e0}}}{\widetilde{\delta n_{\mathrm{d0}}} n_{\mathrm{d0}}} \approx 1. \tag{4.24}$$

Similarly, because of $\tau_r = \tau_c(n_i/n_d)$ during the heating is turning off, a condition of turn-off overshoot effect in terms of τ_c could be derived as:

$$\frac{\tau_{\mathrm{d}}}{\tau_{\mathrm{c}}} << (\frac{\Delta Z_{\mathrm{d0}} \delta n_{\mathrm{d0}}}{\Delta \delta n_{\mathrm{e0}} - 1})(\frac{n_{\mathrm{i0}}}{n_{\mathrm{d0}}}) \approx 1. \tag{4.25}$$

These criteria are also consistent with the computation model described in Chapter 3.

Figure 4.8 shows the time evolution of normalized electron and ion charging currents during heating. The charging time is determined from the sum of these two currents as described in (3.16). All the parameters used for this figure are stated in section 2.2. Initially at $t = 0$ the electron currents represent the electron flux to the initially uncharged dust. As the dust floating potential decreases, the electron current decreases and the ion current increases until reaching an equilibrium with $|I_{\mathrm{e}}| \approx |I_{\mathrm{i}}|$. Then, as electron temperature increases rapidly due to the turn-on of the radio wave heating at $t/\tau_{\mathrm{c0}} = 25$, the electron current increases rapidly dominating the ion current during turn-on. Then, as the floating potential decreases during continued heating, the ion current increases and another equilibrium is reached again with $|I_\mathrm{e}| \approx |I_\mathrm{i}|$ by $t/\tau_\mathrm{c0} = 125$. When the heating is turned off, the electron temperature rapidly decreases and the electron current decreases sharply. The ion current remains near the equilibrium value, relaxing much slower as described earlier and dominates the electron current during turn-off. Eventually the electron current increases and the original equilibrium between the electron and ion currents is again reached by t/τ_c0=300.

In the earlier analysis, a condition for turn-on overshoot is $\tau_\mathrm{d}/\tau_c >> 1$. τ_c may be estimated during turn-on from Figure 3.16 as follows. Defining $x = q_\mathrm{i}\phi_\mathrm{d}/KT$ and v_te0 as the electron thermal velocity before heating, (3.4) and (3.5) may be written just prior to "turn-on" as

$$I_\mathrm{e} = \sqrt{8\pi} r_\mathrm{d}^2 q_\mathrm{e} n_\mathrm{e} v_\mathrm{te0} \exp(x), \tag{4.26}$$

$$I_\mathrm{i} = \sqrt{8\pi} r_\mathrm{d}^2 q_\mathrm{i} n_\mathrm{i} v_\mathrm{ti} (1 - x), \tag{4.27}$$

and x is calculated from the initial equilibrium $I_\mathrm{e} + I_\mathrm{i} = 0$ to be -4.1 for the electron to ion mass ratio used in this study. Since the electron current dominates during turn-on, the turn-on charging time is estimated to be

$$\tau_c \approx \frac{e}{|I_\mathrm{e}|} = \frac{1}{\sqrt{8\pi} r_\mathrm{d}^2 n_\mathrm{e} v_\mathrm{te0} \sqrt{r_\mathrm{h}} \exp(x/r_\mathrm{h})} \tag{4.28}$$

where $r_\mathrm{h} = T_\mathrm{e}/T_\mathrm{e0}$ is the ratio of electron temperature after and before the heating is turned on. Therefore using (3.17) and assuming relatively low dust charge densities ($Z_\mathrm{d} n_\mathrm{d}/n_\mathrm{e} \ll 1$), the condition $\tau_\mathrm{d}/\tau_c >> 1$ for a turn-on overshoot may be used to determine a lower bound on the dust radius. Therefore, the dust radius lower bound could be represented as

$$r_\mathrm{d} \gg \frac{4\pi \exp(2/r_\mathrm{h})}{\sqrt[4]{8\pi} c} \sqrt[4]{\frac{(1+r_\mathrm{h})^2}{r_\mathrm{h}}} \sqrt[4]{\frac{m_\mathrm{e}}{m_\mathrm{i}}} \sqrt{\frac{v_\mathrm{ti}}{n_\mathrm{e}\nu_\mathrm{in}}} f_\mathrm{radar} \tag{4.29}$$

where c is the speed of light in vacuum. Of course possibilities may exist for estimating the degree of the electron temperature enhancement (r_h) assuming and independent measurement of the dust radius.

Just prior to 'turn-off' the electron and ion currents in Figure 4.8 may be written as

$$I_\mathrm{e} = \sqrt{8\pi} r_\mathrm{d}^2 q_\mathrm{e} n_\mathrm{e} v_\mathrm{te0} \sqrt{r_\mathrm{h}} \exp(\frac{x}{r_\mathrm{h}}), \tag{4.30}$$

$$I_\mathrm{i} = \sqrt{8\pi} r_\mathrm{d}^2 q_\mathrm{i} n_\mathrm{i} v_\mathrm{ti} (1 - x), \tag{4.31}$$

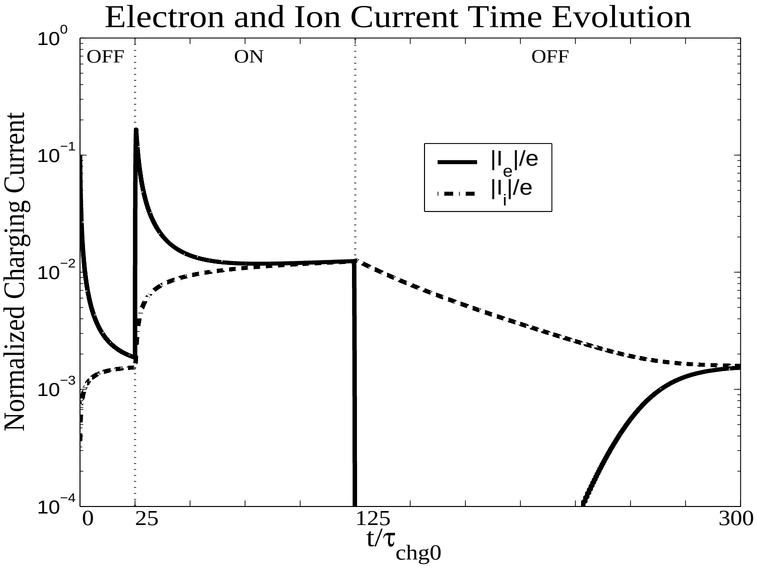

Figure 4.8: Electron and ion charging current time evolution during heating.

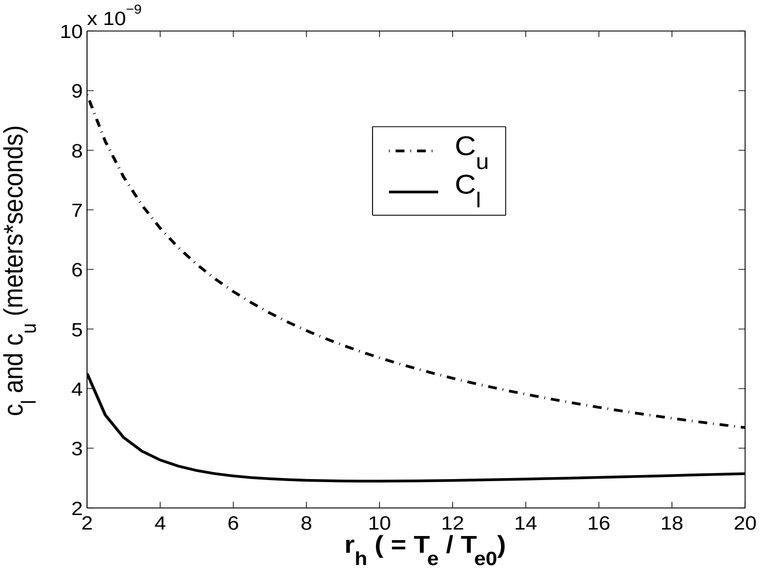

Figure 4.9: Plot of the constants in equations (4.27) and (4.31) dependence on $r_{\mathrm{h}}(= T_{\mathrm{e}}/T_{\mathrm{e0}})$.

where x is determined from the equilibrium $I_\mathrm{e} + I_\mathrm{i} = 0$ during heating. Note that here x depends on r_h. Since the ion current dominates during turn-off, the turn-off charging time is estimated to be

$$\tau_c \approx \frac{e}{|I_\mathrm{i}|} = \frac{1}{\sqrt{8\pi} r_\mathrm{d}^2 n_\mathrm{i} v_\mathrm{ti}(1-x)}. \tag{4.32}$$

Using $\tau_\mathrm{d}/\tau_c << 1$, as a condition for turn-off overshoot, an estimate of the upper bound for the dust radius could be derived. Therefore, the dust radius upper bound could be represented as

$$r_\mathrm{d} \ll \frac{4\pi}{\sqrt[4]{8\pi}c}\sqrt{\frac{2}{1-x}}\sqrt{\frac{v_\mathrm{ti}}{n_\mathrm{i}\nu_\mathrm{in}}} f_\mathrm{radar}. \tag{4.33}$$

In some cases, as predicted by the previous results, it may be possible for both a turn-on and turn-off overshoot to exist at a single frequency. Under these circumstances assuming $n_\mathrm{e} \approx n_\mathrm{i}$ and $T_\mathrm{e} \approx T_\mathrm{i}$, equation (3.32) and (3.36) yield the following bound on the dust radius

$$C_\mathrm{l}\sqrt{\frac{v_\mathrm{ti}}{n_\mathrm{e}\nu_\mathrm{in}}} f_\mathrm{radar} \ll r_\mathrm{d} \ll C_\mathrm{u}\sqrt{\frac{v_\mathrm{ti}}{n_\mathrm{e}\nu_\mathrm{in}}} f_\mathrm{radar}. \tag{4.34}$$

Here C_l and C_u are constants determined from equations (4.27) and (4.31) that depend on the relative temperature enhancement r_h. Using plasma parameters stated earlier, C_l and C_u are calculated to have the following dependence on r_h as shown in Figure 4.9. From Figure 4.9 it can be seen that equation (4.32) may possibly give fairly accurate bounds for r_d as r_h increases. Of course as predicted by the results of section 3.4, the overshoot effects become more prominent as r_h is increased.

4.4 Conclusions

It is clear that active perturbation of the source region of electron irregularities that produce PMSEs will provide a rich source of diagnostic information about the corresponding mesospheric dust layer as well as insight on the physical processes that produce PMSEs. Currently, considerable effort is directed at obtaining this diagnostic information at relatively high observing radar frequencies.

This work has attempted to provide further physical insight into the physical processes associated with temporal evolution of the electron irregularities during the turn-on and turn-off of the radio wave heating. At the turn-on period of the heater, the approximate analytical models provide reasonable agreement with the full computational model results and allow information about the dust layer to be readily obtained from the temporal evolution during the turn-on of the radio wave. Since dust charging dominate the physical process of the turn-on of the radio wave, the existence of turn-on overshoot could be simply decided by the radio of t/τ_r, where τ_r is the reduction rate. The electron density irregularly amplitude (an corresponding radar echo strength) for steady increase during the continued heating is obtained as $t/\tau_r < 1$, and a steady decrease occurs as $t/\tau_r > 1$. The evolution profile could be observed in the simplified equation 4.8. [*Scales and Chen*, 2007a] On the turn-off side, the simplified analytical models (Equation 4.17) also provide quite reasonable agreement with the full computational model results and allow information from the process of turn-off of the radio wave. If the condition of Equation 4.18 is satisfied, the turn-off overshoot will occur with maximum amplitude of $\Delta\tilde{\delta n}_{\mathrm{e}}^{\mathrm{max}}$ (Equation 4.22). The time at which maximum amplitude is reached is τ^{max} (Equation 4.19) and the time scale for decay after the maximum amplitude has reached could be represented as Equation 4.23. It should be noted that all these observable parameters information may be explored on the degree of the temperature enhancement. Also, at least three observable parameters, τ^{max}, $\Delta\tilde{\delta n}_{\mathrm{e}}^{\mathrm{max}}$, and τ_{r} may provide information on the dust layer such as dust density, dust radius, and charge state. [*Scales and Chen*, 2007b].

Extensive experiments are required at lower observing radar frequencies than are currently being carried out as can be seen in Figure 4.1 to effectively exploit all of the diagnostic information available during the turn-on of the radio wave heating. It is clear however, that this information should be of the same significance as that available at higher observing radar frequencies.

Chapter 5

Experimental Observation

PMSE primarily have been studied at 50 MHz. The first observations were made by Ecklund and Balsley [*Ecklund and Balsley,* 1981] using the Poker Flat radar; many other observations followed with smaller radars. Observations have also been made at 224 MHz [Rottger et al., 1988]. Echoes have also been recorded at even the higher frequencies of 933 MHz [*Rottger et al.,* 1990] and 1290 MHz [*Cho et al.,* 1992].

In order to verify the theoretical predictions of chapter 3 and 4, new physics is expected to be observed in lower observation frequency such as HF band. Previously, there were few sets of observations at frequencies in the HF band between 8 and 9 MHz. One used the SURA heating facility (56°N latitude) as a radar [*Karashtin et al.,* 1997]. The second used a dynasonde and was conducted in conjunction with the EISCAT VHF radar [*Lee et al.,* 2001]. Recently, HF observations were operated at HAARP between 3.1 to 8.1 MHz. [*Kelley et al.,* 2002]. It showed the observation results of initial proof-of-concept campaign which had a limited 18 hours observing time in the summer of 2000.

Experimental study of PMSE modification is a significant undertaking and currently many opportunities exist for ground breaking contributions to this new and what is expected to be a rapidly growing area of research. Past experimental work has primarily concentrated on modification of PMSE in the VHF range [e.g. *Havnes, et al.,* 2003, 2004, *Biebricher et al.,* 2005]. The predictions of the modeling work described in the previous sections (e.g. Figure 4.1) show, however, that important new physics is expected to be observed when modifying PMSE in the HF range. This new physics (the turn-on overshoot) is of fundamental importance because it is evidence of direct charging of dust in the PMSE source region by the heater wave which has not been studied or observed before. The goals of the experimental research plan are to study modification of PMSE in the HF frequency range to look for this new phenomenon.

There are two observation campaigns operated in the past two summers at HAARP, Gakona, AK. As shown in figure 5.1, HAARP will be operated as a heater to artificially vary the electron temperature in the PMSE layer. In the meantime, radars will operate for PMSE observation. Because of the nonlinear relationship between the electron temperature and other physical parameters in this layer, some fundamental physics could be explored. HAARP heater will work at 3.16 to 3.22 MHz which will heat up the dust layer most efficiently. A sub-array of HAARP will operate at 4.9 MHz as a HF transmitter, a spiral antenna nearby will work as a HF receiver. There are other diagnostic instruments at HAARP, including 28/50/139 HF/VHF MHz radars and 446 MHz UHF radar. They will operated the full time during the heater is operating as a reference and diagnostics.

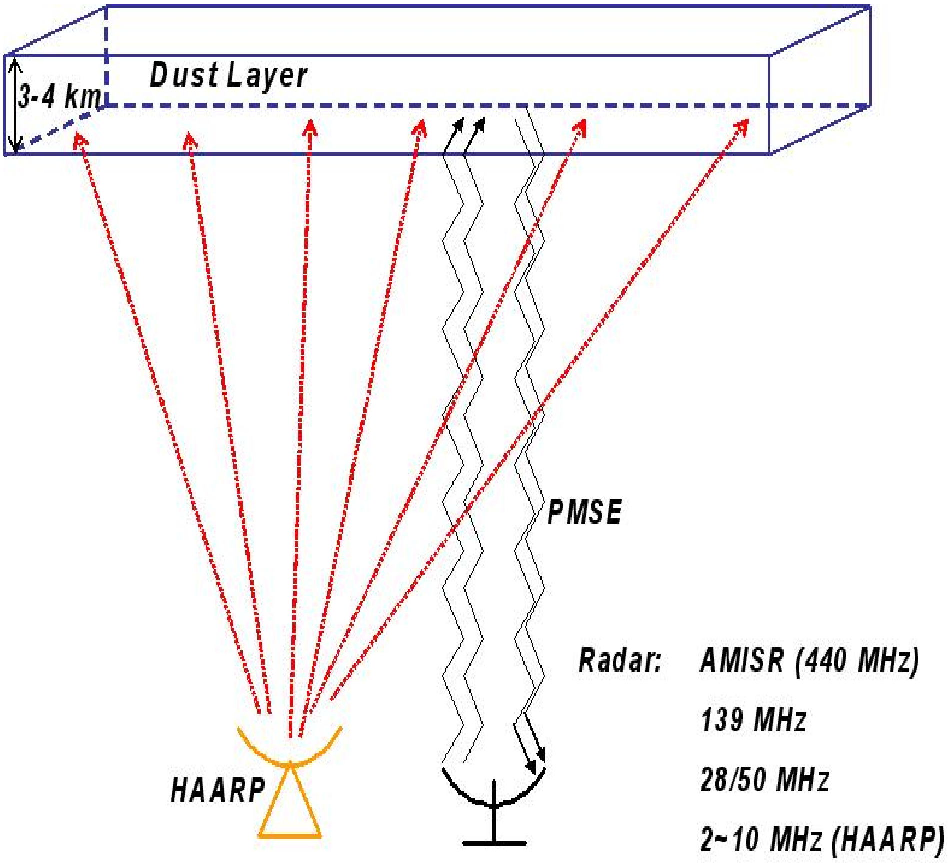

Figure 5.1: The PMSE heating experiment scenario

5.1 System Description

The HAARP (High Frequency Active Auroral Research Program) Gakona Ionospheric Observatory is located near Gakona, Alaska (62° 23.50'N, 145°8.80'W). The basic research element is an HF transmitter providing electronic phased-array beam steering, wide transmitter frequency coverage, and a large effective radiated power. The transmitter is capable of delivering up to 3.6 million Watts to an antenna system consisting of 180 crossed dipole antennas arranged as a rectangular, planar array. More details are covered at Chapter 2. The optimal observation for PMSE using HAARP as a HF transmitter is around 4 - 5 MHz. [*Kelley et al.*, 2002] Campaigns during the past two summers all employed 4.9 MHz for observation. Additional HAARP instrumentation included a permanent 446 MHz incoherent scatter radar system which has been in full operation on a campaign basis for both campaigns. In 2007 campaign, another 50 MHz coherent scatter Radar system were also available.

Partial HAARP antenna array is used as HF radar transmitter. A spiral antenna on HAARP site near the HAARP antenna array is employed as the receiver antenna. The receiver systems were illustrated in figure 5.2 and 5.3. Campaign 2006 used digital receiver shown as figure 5.2 and campaign 2007 employed analog receiver shown as figure 5.3. Both receivers work fine and successfully detected PMSE.

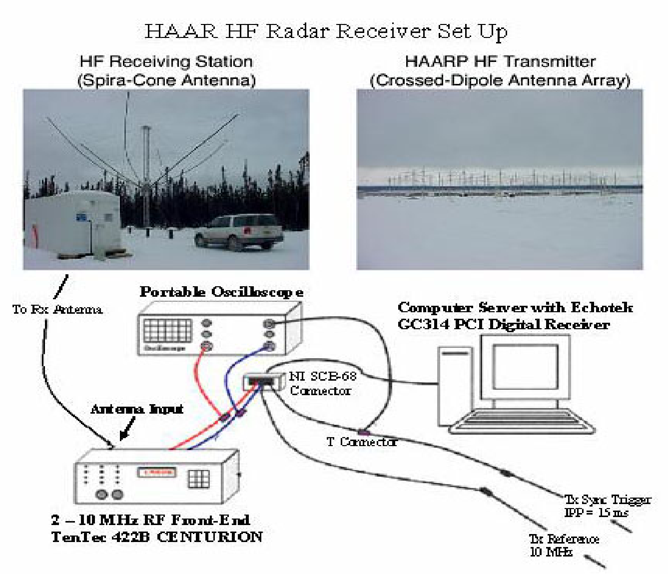

Figure 5.2: HAARP HF radar digital receiver set up.

Since the above two receiver systems are not design specifically for our mission, our group has design and constructed our own HF radar digital receiver. It is similar to

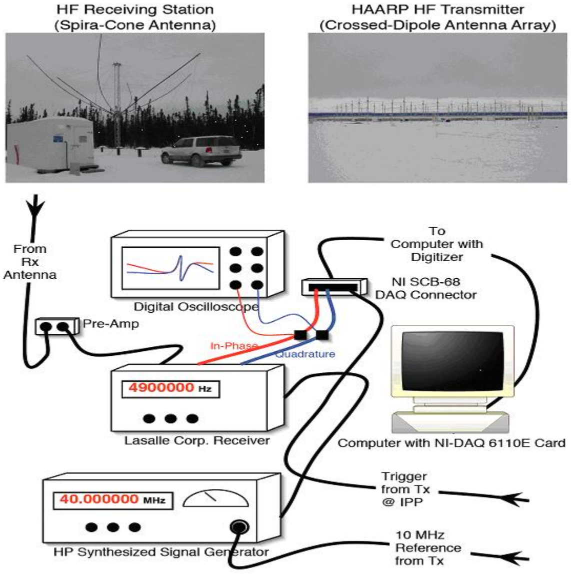

Figure 5.3: HAARP HF radar analog receiver set up.

the system shown in figure 5.2. This radar receiver consists of a 2 - 10 MHz RF front end, and a Echotek GC314-PCI/FS digital receiver. Echotek digital receiver has three A/D converters which is fast enough for direct conversion in HF band. Therefore, RF front end is constructed with only filters, amplifiers, attenuators and limiter. This simply designed RF front end will work efficiently for PMSE observation in HF band.

Echotek GC314-PCI/FS digital receiver is widely used in radar astronomy area. It has a 105 MHz A/D converter and provides 3 output channels. HAARP provides 10MHz GPS time signals and trigger time signals, which could used for GC314 card as reference time and trigger. The GC314 board has three A/D converters coherently sampling (IF) inputs with 14-bit resolution with SFDR $>$ 90 dB and 100 dB 2-tone. It has raw A/D data collection support and has 12 narrowband digital receiver channels with up to 2.5 MHz bandwidth each. Each Single wideband receiver channel has up to 42 MHz usable bandwidth. The data output is go via PCI interface (64 bits at 66 MHz). It could supports a wide variety of applications. More detail information could be found at Echotek website.

The operation system for this system is QNX real time operation system. QNX is a real time operating system designed for critical tasks. Its strengths are the development of software, control of industrial robots and embedded devices. This operation system is chosen to satisfy radar system's huge and fast data processing requirement.

The HAARP transmitter system has flexible operating characteristics, allowing us to perform multiple experiments with a delay of only 30 seconds. The transmitting antenna is a phased array and is designed to transmit a narrow beam of high power radio waves at frequency allocations between 2.8 to 10 MHz.We used frequencies of 3.16, 3.25, and 4.9 MHz in the experiment campaigns. For reference, when oriented in the vertical direction, the gains and solid angle of the beams are 14 dB (0.5 str), 18.5 dB (0.18 str), and 2.3 dB (0.073 str). The transmitted power is available in submultiples of 3.6 MW. The antenna can be tilted to a maximum of 30° from the vertical in all directions.

The receiving antenna was pointed strictly vertical with a gain of 11 dB and a solid angle beam width of 1.0 str. Since specular reflections may be dominant, we record the vertical transmitter gain and call it the Transmitter Gain (vertical).

5.2 Experiment Setup and experiment results

We anticipated two campaigns at HAARP, one in August 2006 and the other one operated at July 2007.

5.2.1 Campaign 2006

There are two main objectives for the experimental campaign. The first is to show that the turn-on overshoot behaves as predicted by the theoretical model shown in Figure 4.1. Figures 3.5 and Figure 4.1, show that this temporal behavior should exist for longer irregularity scale sizes and lower observing radar frequencies. From the possibilities of observing radar frequencies at the HAARP facility just described, the predictions of the preliminary model calculations show that the charging rate would be significant enough in comparison to the diffusion rates in this regime for existence of a prominent turn-on overshoot feature. All available radar frequencies will be used to study the variation in the temporal evolution of PMSE during modification to search for this feature. The second goal is to use the experimental data to make predictions of the dust radius with the dust radius diagnostic developed by using conditions for existence of the overshoot features such as equation 3.30. Any other possible independent predictions on the dust radius will be used to test the Time (minutes) Altitude (km) Time (minutes) Signal Power Level accuracy of this proposed diagnostic. As described earlier, this diagnostic will be refined to extend to a distribution of dust radii using the numerical model described in chapter 3 and chapter 4.

At year 2006, only 48 antennas were in use at HAARP and it only has 960 KW

Pulse Width	IPP (ms)	Freq-D (MHz)	Antenna Pointing Angle (Degrees)	Power (KW)	Pattern	Tx Gain (Vertical) (dB)	Rx Gain (Vertical) (dB)	Duration (Minutes)
10 μs	15	4.9	0	960	O	18.5	11	5 - 90 min

Table 5.1: Experiment Setup for PMSE detection.

capacity. The experiment was divided into two phases. We firstly used HAARP as radar to detect PMSE, once PMSE is detected, HAARP were operated as both heater and radar for the PMSE heating experiment as the second phase. Additionally, 446 MHz VHF MUIR radar has been in full operation on a campaign basis. However, due to the relatively small size of this radar and their modest peak power the PMSE echoes were relatively weak. Therefore, we only studied the data from the HF radar. The experiment was performed at August 7th 21:00 UT to 23:00 UT, which is 1:00 PM to 3:00 PM local time, since the noon time is the optimal observation time.

Firstly, we used HAARP as transmitter following the below modulation until we detected PMSE: Optical Emissions, F-region + MZ Pulsing (15.0/4.9) or (IPP/Radar Freq). Table 5.1 gives more details.

We used pulses with an IPP of 15 ms to ensure that we were not contaminating the collected signal with echoes from higher heights. The transmitting antenna is a phased array and is designed to transmit a narrow beam of high power radio waves at frequency of 4.9 MHz, when Radar were oriented in the vertical direction, the gains and solid angle of the beam is 18.5 dB (0.18 str). The receiver receiving antenna was pointed strictly vertical with a gain of 11 dB and a solid angle beam width of 1.0 string.

The PMSE detection operation lasted about 45 minutes. From figure 5.4,the existence of PMSE at 4.9 MHz is quite clear and indisputable. The radar signature located at 85 km away from the ground, when the transmitter stop transmitting at 41 minutes, the radar scatter gone as well. Therefore, we successfully observed PMSE at HF frequencies for the second time in Alaska. Then we went to the second step of the experiment.

The second step is the PMSE heating experiment, in this experiment, HAARP will be split into two parts. One part will be operated the same as the first step, HAARP will be continually used as a radar transmitter at 4.9 MHz, and the rest of HAARP will be operated using Continuous Wave (CW) mode. This CW mode EM wave will couple with the lower ionosphere, optimally at 80 90 km. According to the ionogram, (more details at http://137.229.36.30/cgi-bin/digisonde/latest.cgi), 3.16 MHz would

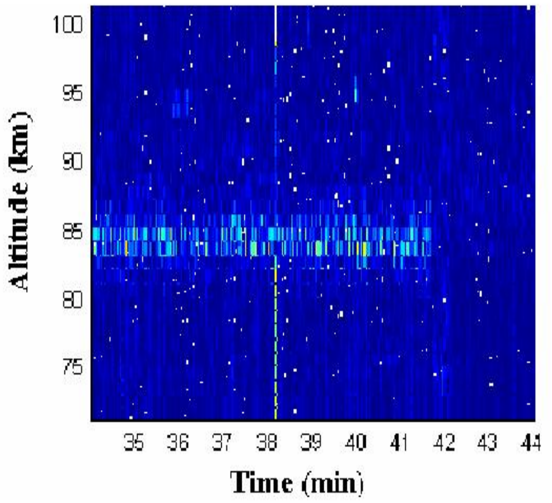

Figure 5.4: SNR versus time plot of HF PMSE detection at 4.9 MHz.

be the best absorbtion frequency for PMSE heating experiment.

The experiment schematics were stated in the following tables.

a) HAARP as heater. See table 5.2.
b) HAARP as radar. See table 5.3.

Different power consumption combination were tested. The best results were explored at 50% for heater and 50% for radar transmitter combination, which means, half of the array were used as transmitter and the rest were employed as heater.

Figure 5.5 showed one set of the results from the experiment, it is the first experiment ever done to explore the PMSE radar back scatter variation during heating at the HF frequency band. It is very clear, when the heater is on, the PMSE S/N is higher than when the heater is off. This is opposite to all the previous theories and experiments at much higher frequency range. It is noted that this figure shows similar profile as figure 3.3.

τ_r is the reduction time of the electron density due to the dust charging from electron flux. It could be represented in terms of τ_c as $\tau_r = \tau_c(n_e/n_d)$ during the turn-on. It is of the same order as the time of the radar backscatter power level increases to the maximum after the heater is turned on. The time of radar signal

Pulse Width	IPP (ms)	Freq-D (MHz)	Antenna Pointing Angle (Degrees)	Power (KW)	Pattern	Duration (Minutes)
CW/On	CW/On	3.16	0	680	O	3 min
CW/Off	CW/Off	3.16	0	680	O	3 min
CW/On	CW/On	3.16	0	580	O	3 min
CW/Off	CW/Off	3.16	0	580	O	3 min
CW/On	CW/On	3.16	0	480	O	3 min
CW/Off	CW/Off	3.16	0	480	O	3 min

Table 5.2: HAARP operated as heater at 3.16 MHz, heater will be turn on and turn off in sequences with different power consumptions. Note: Repeat this cycle as time allows.

Pulse Width	IPP (ms)	Freq-D (MHz)	Antenna Pointing Angle (Degrees)	Power (KW)	Pattern	Duration (Minutes)
10 μs	15	4.9	0	280	O	5 min
Change power to 360 KW						1 min
10 μs	15	4.9	0	380	O	5 min
Change power to 460 KW						1 min
10 μs	15	4.9	0	480	O	5 min

Table 5.3: HAARP operated as radar at 4.9 MHz, the radar transmitter will be operated in a sequences with different power consumptions. Note: Repeat this cycle as time allows.

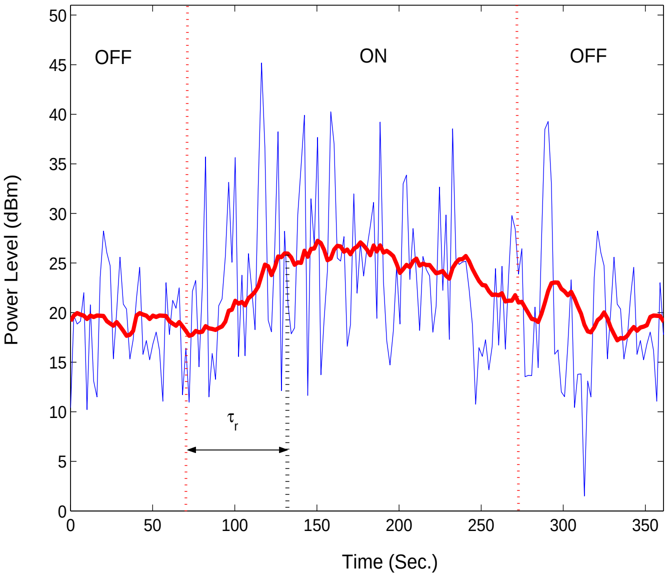

Figure 5.5: HF radar incoming signal power level during PMSE detection at 4.9 MHz

power level increases to maximum after turn on can be seen from figure 5.5 to be 50 seconds. From equation 4.47, the reduction time could be calculated as:

$$\tau_{\mathrm{r}} = \frac{1}{\sqrt{8\pi} r_{\mathrm{d}}^2 n_{\mathrm{d}} v_{\mathrm{te0}} \sqrt{r_{\mathrm{h}}} \exp(x/r_{\mathrm{h}})} \tag{5.1}$$

Therefore, the dust density could be represented as:

$$n_{\mathrm{d}} = \frac{1}{\tau_{\mathrm{r}} \sqrt{8\pi} r_{\mathrm{d}}^2 v_{\mathrm{te0}} \sqrt{r_{\mathrm{h}}} \exp(-4.1/r_{\mathrm{h}})} \tag{5.2}$$

Applying the same parameters used in Chapter 3.2, typical subvisible mesospheric dust $r_d = 10$ nm, electron thermal velocity v_{te0} 10^5 m/s, temperature enhancement ratio equal to 5, the dust density is calculated approximately to be 10^9 m^{-3}, which is about 10% of the background electron density. This is reasonably consistent with the previous sound rocket experimental observations.

This show promising results for exploiting existence of an overshoot in HF PMSE strength during the turn-on, and utilizing it for diagnostic tools of dust characteristics. However, due to the limitation of experiment time and experiment equipment at HAARP, I was unable to collect enough data for definitive conclusion. Therefore, another experimental campaigns were performed at summer 2007.

5.2.2 Campaign 2007

Followed by the experiences and results in campaign 2006, The primary objective of campaign 2007 is to observe the effects of ionospheric heating on HF PMSE since the physics is predicted to be significantly different that the effects on VHF PMSE which is the work of EISCAT. (The difference is of course the prediction of the turn-on overshoot effect which is directly due to the electron current charging onto the dust.)

The campaign was taken July 2007. The Air Force Research Lab Lasalle HF analogy radar receiver was used instead of the digital receiver. The radar system description is shown as Figure 5.3. Additionally, another 50 MHz VHF radar were operated the whole time during the HF heating experiment as a diagnostic.

At 2007, HAARP finalized their facility updating. We got the full transmitter capacity for the experiment. The 180 antenna array could provide 3.6 GW off the antenna power, and it is currently the world biggest transmitter. The experiment scenario is relatively simpler comparing with campaign 2006. We used 48 antennas as the HF transmitter and the rest 132 antenna as the heater. We kept the transmitter running the whole experiment, and turn on and turn off the heater 5 minutes each in a sequence. The experiment was taken at July 31th, 19:00 UT to 21:00 UT, which corresponding to 11:00 AM to 1:00 PM local time. The heater used 3.25 MHz frequency, which will give a higher absorbtion ratio at PMSE layer. Table 5.4 gave more details about the experiment setup.

a) HARRP as a radar transmitter at 4.9 MHz (see table 5.4):

b) HAARP as a heater at 3.25 MHz (See table 5.5):

Figure 5.6 shows the preliminary result of radar backscatter during the whole experiment time. The PMSE radar signature is clearly shown located at 85 to 90 km range. Since we turn on and off the heater sequentially, the PMSE power amplitude and the background noise varied simultaneously. There are some strip shown on the plots which saturated the incoming signals. This is the noise generated by the surrounding digisonde at HAARP.

Figure 5.7 showed signal versus time plot of the back scatter during the heating sequence. This plot did a integration of the incoming signal power from 70 to 100 km, which clearly indicated the transitions of the PMSE variation during the heater turn-on and turn-off. From the plot, incoming signal is stronger during the turn-on and weaker during turn-off, which verified figure 4.1. Also, it is obviously shown that

Pulse Width	IPP (ms)	Freq-D (MHz)	Antenna Pointing Angle (Degrees)	Power (KW)	Pattern	Antenna Array Size	Duration (Minutes)
10 μs	5	4.9	0	960	O	48	120 min

Table 5.4: HAARP operated as radar at 4.9 MHz for 2 hours during the experiment.

Pulse Width	IPP (ms)	Freq-D (MHz)	Antenna Pointing Angle (Degrees)	Power (KW)	Pattern	Antenna Array Size	Duration (Minutes)
CW/On	CW/On	3.25	0	2640	O	132	3 min
CW/Off	CW/Off	3.25	0	2640	O	132	3 min

Table 5.5: HAARP operated as heater at 3.25 MHz with 5 minutes on and 5 minutes off for 2 hours during the experiment.

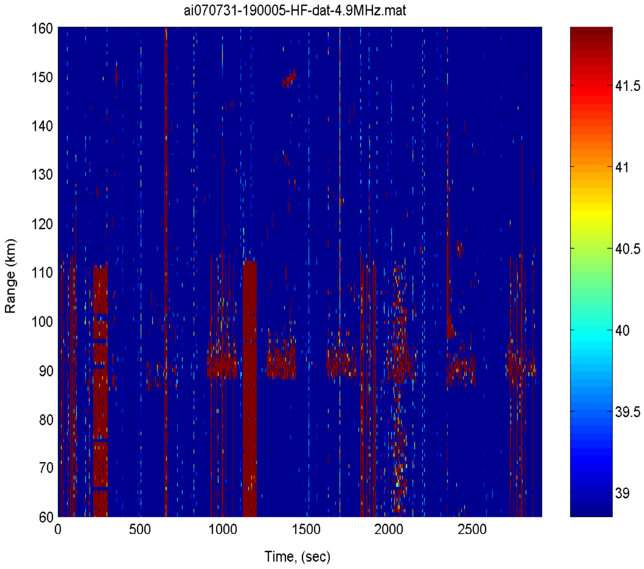

Figure 5.6: SNR versus time plot of HF PMSE heating observation at 4.9 MHz

turn-on overshoot exists.

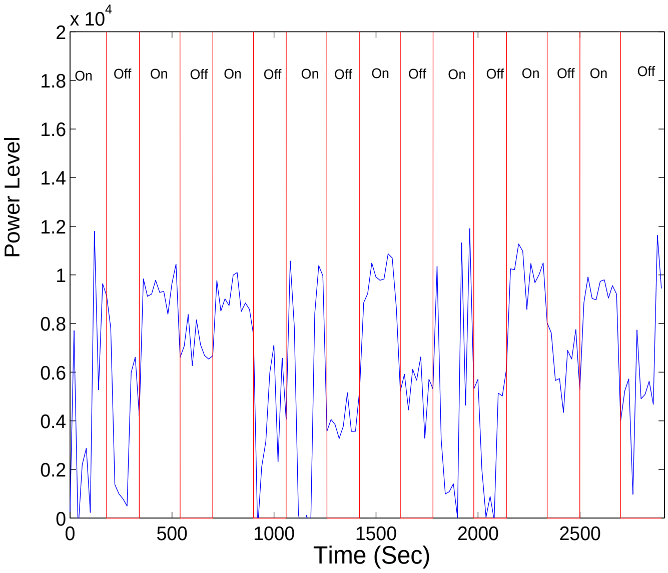

Figure 5.7: Signal power (dBm) of HF PMSE radar scatter during heatings at 4.9 MHz

Figure 5.8 is the normalized signal power plot of figure 5.7. The PMSE enhancement could seen clearly during the heating. However, comparing with figure 3.3, the transition of both increase during the turn-on and decrease after turn-off is quite fast in figure 5.8. This may caused by the heater noise since the heater frequency is very close to the transmitter frequency.

As it was mentioned, another 50 MHz radar was operated simultaneously as well. However, due to the relatively low transmitter power, we did not see any PMSE during the experiment time. The experiment results from this 50 MHz radar were plot in figure 5.9.

5.3 Conclusion

We successfully observed PMSE at HF frequencies during the artificial heating for the first time ever. The PMSE signal power level is higher during the heating, which satisfied our theory decried in chapter 3 and chapter 4. Comparing with previous experiments at EISCAT, e.g. figure 2.8 and figure 2.9, the experiment results described in this chapter show that the enhancement of electron density irregularities during

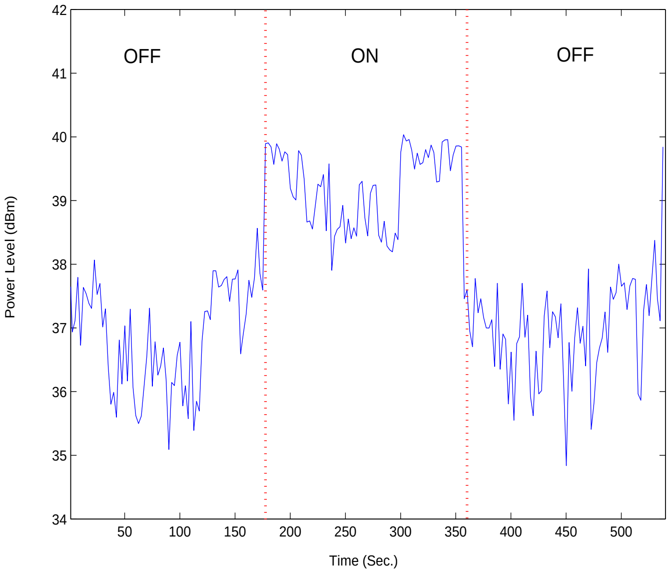

Figure 5.8: Normalized Signal power (dBm) of HF PMSE radar scatter during heatings at 4.9 MHz

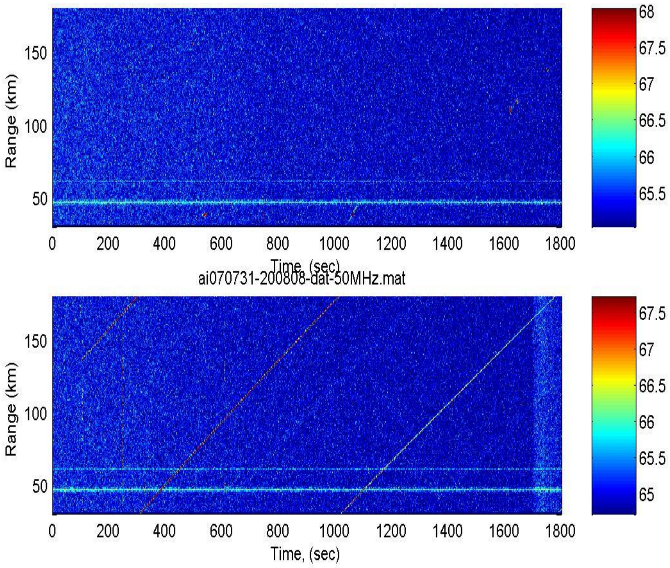

Figure 5.9: 50 MHz radar observation during the experiment

radio wave heating should exist for longer irregularity scale sizes and lower observing radar frequencies.

Current HAARP experiment results also look promising for the existence of PMSE turn-on overshoot. However, more careful experiments need to be done before firm conclusions can be drawn. The new designed Echotek digital receiver is ready for use now. It will be much superior to the experimental setup used for measurements in the previous campaign.Therefore, future experimental campaigns are planning next year to support the theoretical research.

Chapter 6

Conclusions and Future Work

6.1 Conclusions

Modification of PMSEs by radio wave heating is a relatively new and important area of investigation and more experimental and theoretical studies must be performed. As has been pointed out [*Dimant and Milikh,* 2004; *Havnes et al.,*2003; *Havnes,* 2004], tremendous potential exists for remote sensing of dust parameters in the mesosphere once accepted theoretical models have been developed. The work here has investigated the relative importance of dust charging and diffusion processes in temporal behavior during radio wave heating of electron irregularities that produce PMSEs. A "turn-on overshoot" has been predicted during PMSE modification here and the phenomenon should be more pronounced at lower observing radar frequencies (near or below 50 MHz) and/or for larger dust sizes. On the other hand, the "turn-off overshoot" which has been predicted and observed previously, should be more pronounced at higher observing radar frequencies and/or for smaller dust radii. Under certain conditions, the turn-on overshoot could be as prominent as the turn-off overshoot. Both overshoot phenomena are expected to provide useful information about the dust layer.

This work has provided both computational and analytical model for investigating the temporal behavior of the electron irregularities during radio wave heating, which includes both the effects of diffusion and dust charging. It has been shown that the relative rate of diffusion to charging provides a prediction of this temporal behavior. The rate of these two physical processes depends on both background plasma and dust parameters and may ultimately provide diagnostic information about the dust layer as described here. Overshoot in the electron irregularity amplitude during turn-on of the radio wave may occur when the rate of charging greatly exceeds the rate of diffusion. During turn-off of the radio wave, the overshoot in irregularity amplitude may occur if the diffusion rate greatly exceeds the charging rate. During the turn-on of the radio wave, the physics is primarily driven by the electron diffusion and charging behavior. During turn-off of the radio wave, the physics is primarily driven by the ion diffusion and charging behavior. The scale size of the irregularities (and therefore the observing radar frequency) is of course an important factor in determining the temporal behavior since the irregularity scale size is intimately related to the diffusion rate. For smaller-scale irregularities (higher radar frequencies), diffusion effects are dominant over charging. For larger-scale irregularities (lower radar frequencies) charging is dominant over diffusion effects. Therefore higher frequency observations may provide important information about diffusion properties in the dust cloud and lower-frequency observations may provide information about charging. As described earlier, for irregularities sufficiently large for diffusion to not be important on the heating timescales, charging is completely dominant. Therefore the temporal evolution of the electron irregularities during radio wave heating may allow opportunity for more efficient testing of dust charging models in this case. More detailed comparisons with a broader spectrum of experiments over a wider observing radar frequency range must be done to test the predictions of the present model and before definitive conclusions can be drawn.

Two scientific campaign were performed during the passing two summers. The radar system successfully detected PMSE at 4.9 MHz HF frequency. The first ever HF radar observation of PMSE heating experiment was also performed and showed very promising results. New designed digital receiver is finished for future observations. This receiver is designed and utilized specifically for this project and will be much superior to the previous experimental setup.

It should be noted that the present study has primarily considered possible conditions for the existence of overshoot phenomenon during modification of PMSEs. It has not addressed in detail or provided a detailed parametric study of how the absolute amplitude or strength of the overshoot features vary with important dust and plasma parameters. For instance, most of the results presented here utilize an electron temperature enhancement of Te/Te0 = 10. Maximum turn-off overshoot radar enhancements, which are proportional to dne^2, are predicted to be in the range of $25-30$ in this case. The first experimental observations [*Havnes et al.,* 2003] show enhancements of $5-6$. Radar enhancements in this range are more consistent with a reduced factor of $Te/Te0 < 4$ (e.g., Figure 4.11) which underscores the importance of performing a thorough study of the radar echo strength variation with dust layer and plasma parameters. It is believed the results presented here will provide insight for such a detailed study which will clearly allow useful diagnostic information to be obtained when compared to experimental observations. The present model should be useful for such a purpose and this is planned for future investigation.

6.2 Future Works

6.2.1 Theoretical Modelling improvement

As described in the previous chapters, initial development of a new model to investigate modification of PMSE by radio wave heating is progressing. Several important preliminary predictions show significant promise and should be investigated in more detail. The first important new prediction is the existence of an overshoot in HF PMSE strength during the turn-on of the heating radio wave as shown in Figure 2. It is clear that such an overshoot will provide critical information on the charged dust layer just as does the overshoot observed during turn-off that is currently being vigorously studied for the case of VHF PMSE [*Havnes et al.,* 2003; 2004; *Biebricher et al.,* 2005]. The fundamental physical importance of the turn-on overshoot is that it is predicted to be a direct consequence of dust charging in the PMSE layer by the radio wave heating as compared to the turn-off overshoot which may be considered an indirect consequence of the dust charging by the radio wave heating. Both overshoot features are expected to lead to crucial diagnostics for the dust layer once a firm theoretical foundation of the physics of the overshoot features is obtained. The starting point for this theoretical foundation is clearly a basic understanding of the physical conditions necessary for the existence of the overshoot features in terms of the dust layer and heating parameters. Possible theoretical conditions have been stated earlier from the work of [*Chen and Scales,* 2005] which are, $\tau_{dif}/\tau_{chg} >> 1$ for the turn-on overshoot and $\tau_{dif}/\tau_{chg} << 1$ for the turn-off overshoot. Unfortunately, this past work was limited to a narrow parameter regime.

The first task in the theoretical component of the proposed research plan is a more thorough and complete investigation of the parameter regimes in which the PMSE overshoot features may exist. The numerical model of [*Chen and Scales,* 2005] will be used to study a broader range of charged dust densities nd, charged dust radii rd, dust mass distributions, electron temperature enhancements, and observing radar frequencies to access the conditions for the existence of PMSE overshoot features more thoroughly. This study will provide more predictive and diagnostic capability for future experimental design. A closely related issue that will also be undertaken during this component of the research plan is a study of the variation of the relative strength of the two PMSE overshoot features with the variation of all parameters just stated. Scaling laws will be obtained for the variation of the relative strength of the PMSE overshoot features with these parameters. This will clearly provide further diagnostic information on the dust layer.

The second task in the theoretical component of the research plan involves investigation of the effects of dust charging physics on the model of [*Chen and Scales,* 2005] . This is a critical issue, since both overshoot features are ultimately produced by dust charging in the PMSE layer and an accurate dust charging model must be utilized.

The model of [Chen, 2005] as well as the model of [*Havnes,* 2004] utilized continuous Orbit Motion Limited OML dust charging [*Shukla and Manun,* 2002]. It may be argued that in the mesosphere, the charged dust particles only carry several elementary charges since they are typically of the size of 1-10 nm, discrete charging using appropriate rate coefficients [*Dimant and Milikh*, 2004] is more appropriate. Such discrete charging (with fixed dust mass) has been used in recent work on modelling the behavior of PMSE during radio wave heating [*Biebricher et al.,* 2005] as well as modelling of the steady-state behavior of electron irregularities thought to produce PMSE in the presence of charged dust [*Lie-Svenson et al.,* 2003]. A more accurate charging model will utilize a variable dust mass distribution (as allowed by the model of [*Chen and Scales,* 2005]) and a statistical approach to attach an appropriate number of discrete charge states to the individual dust particles [*Scales et al.,* 1997, *Chen and Scales*, 2007]. The later is the approach that will be utilized in this component of the research plan. Comparisons will be made between the continuous OML model and the discrete charging models using the statistical approach. Additionally, it is useful to consider other possible expressions for the ion and electron attachment rates [e.g. *Natanson*, 1960. *Drain et al.,* 1987]. This will allow for the most accurate possibilities for dust layer diagnostics as well as assessment of various charging models when comparisons are made between numerical models and experimental observations.

The third task will utilize a new electron temperature T_e evolution model during heating. The previous physical model of [*Chen and Scales*,2005] assumed a constant electron temperature, after the first sudden rise when the heater is switched on. This assumption may be valid for low values of the ratio between charge density of dust and electron charge density, throughout the PMSE layer, since the dust has little effect on the electron density. However, when this ratio is not small compared to 1, there may be an electron bite-out, as the increased electron temperature and collision rate of electrons and dust particles, can now lead to a significant reduction in the electron density. A new temperature evolution model will be developed to explore the validation of this diagnostic prediction.

The final task in this section of the research plan will be development of simple analytical expressions for dust layer diagnostics based on the physics of the interaction of the heating radio wave and the PMSE associated dust layer. Preliminary work has been done. [*Scales and Chen 2007a, 2007b*] and details has been covered in Chapter 4. Extensive experiments are required at lower observing radar frequencies to effectively exploit all of the diagnostic information available during the turn-on and turn-off of the radio wave heating.

6.2.2 Numerical Model Improvement

In the current numerical model, the explicit method is used to solve the model and calculate the electrical field.

Numerical solution schemes are often referred to as being explicit or implicit. When a direct computation of the dependent variables can be made in terms of known quantities, the computation is said to be explicit. In contrast, when the dependent variables are defined by coupled sets of equations, and either a matrix or iterative technique is needed to obtain the solution, the numerical method is said to be implicit. Normally, the implicit method is more accurate and more stable.

The continuity equation is stated in the previous chapter, see Equation 3.1. This is a very complex partial differential equations. And we want to solve it implicitly. Simplify the equation in the following form:

$$\frac{\partial n_{\mathrm{i}}}{\partial t}+\frac{\partial F_{\mathrm{i}}}{\partial x}=S_{\mathrm{i}} \tag{6.1}$$

Using FDM, numerically, we get:

I. Explicit Method:

$$\frac{n_{\mathrm{ix}}^{t+\Delta t}-n_{\mathrm{ix}}^{t-\Delta t}}{2\Delta t}=-\frac{F_{\mathrm{ix+\Delta x}}^{t}-F_{\mathrm{ix-\Delta x}}^{t}}{2\Delta x}+S_{\mathrm{ix}}^{t} \tag{6.2}$$

$$n_{\mathrm{ix}}^{t+\Delta t}=n_{\mathrm{ix}}^{t-\Delta t}-2\Delta t(\frac{F_{\mathrm{ix+\Delta x}}^{t}-F_{\mathrm{ix-\Delta x}}^{t}}{2\Delta x})+2\Delta t S_{\mathrm{ix}}^{t} \tag{6.3}$$

II. Implicit Method

$$\frac{n_{\mathrm{ix}}^{t+\Delta t}-n_{\mathrm{ix}}^{t-\Delta t}}{\Delta t}=-\frac{1}{2}(\frac{F_{\mathrm{ix+\Delta x}}^{t+\Delta t}-F_{\mathrm{ix-\Delta x}}^{t+\Delta t}}{2\Delta x}-\frac{F_{\mathrm{ix+\Delta x}}^{t}-F_{\mathrm{ix-\Delta x}}^{t}}{2\Delta x})+\frac{1}{2}(S_{\mathrm{ix}}^{t+\Delta t}+S_{\mathrm{ix}}^{t}) \tag{6.4}$$

The system of nonlinear equations represented above in 5.18 has a block tri-diagonal structure. The equations are solved using Newton-Raphson iteration between time steps in the manner described by Hastings and Roble [*Hastings and Roble*, 1977]. Typically, only three iterations are required to yield a relative error o f 10^{-4} or less.

To retain accuracy, the time step Δt is adjusted adaptively according to charging and diffusion reaction time constants. Both initial conditions ($n_{\mathrm{ik}}(t=0)$) and boundary conditions ($n_{\mathrm{io}}(t)$) and ($n_{\mathrm{iK}}(t)$) must be specified for each species to permit solution of the equation. Periodic boundary conditions are used so that ($n_{\mathrm{io}}(t)$) = ($n_{\mathrm{iK}}(t)$). This condition does affect the solution because the grid spacing is increased if the density perturbations approach the boundary.

6.2.3 Experimental Observation Improvement

Experimental study of PMSE modification is a significant undertaking and currently many opportunities exist for ground breaking contributions to this new and what is expected to be a rapidly growing area of research. Past experimental work has primarily concentrated on modification of PMSE in the VHF range. The predictions of the modeling work described in the previous chapters (e.g. Figure 4.1) show, however, that important new physics is expected to be observed when modifying PMSE in the HF range. This new physics (the turn-on overshoot) is of fundamental importance because it is evidence of direct charging of dust in the PMSE source region by the heater wave which has not been studied or observed before. The goals of the experimental research plan are to study modification of PMSE in the HF frequency range to look for this new phenomenon.

The future observations will take place approximately between 11AM and 3PM local time. All appropriate available diagnostics will be run during the campaign to monitor important parameters such as riometer absorption. The HAARP facility allows for half of the antenna array to be used for radio wave heating and half for the diagnostic radar transmitter. A synchronized external radio receiver must be used under this circumstance. Such an experimental setup currently exists at HAARP and has been used to make measurements of HF PMSE at 4.9 MHz. The new designed Echotek digital receiver system will employed for more accurate measurement.

There are two objectives of the experimental work proposed here. The first is to show that the turn-on overshoot behaves as predicted by the theoretical model shown in Figure 3.4. Figures 3.4, and 3.5, show that this temporal behavior should exist for longer irregularity scale sizes and lower observing radar frequencies. From the possibilities of observing radar frequencies at the HAARP facility just described, the predictions of the preliminary model calculations show that the charging rate would be significant enough in comparison to the diffusion rates in this regime for existence of a prominent turn-on overshoot feature. All available radar frequencies will be used to study the variation in the temporal evolution of PMSE during modification to search for this feature. The second goal is to use the experimental data to make predictions of the dust radius with the dust radius diagnostic developed by using conditions for existence of the overshoot features such as equations (3.32) and (3.36).

Any other possible independent predictions on the dust radius will be used to test the Time (minutes) Altitude (km) Time (minutes) Signal Power Level accuracy of this proposed diagnostic.

6.2.4 Collaboration with AIM Satellite Mission and CARE Experiment

The Aeronomy of Ice in the Mesosphere (AIM) satellite, which is scheduled to lunch on March 29th, 2007, will explore the formation and variation of Polar Mesosphere Clouds (PMC) using optical instruments. The overall goal of the AIM mission is to explore noctilucent clouds, to find out why they form and why they vary. By measuring PMCs and the thermal, chemical and dynamical environment in which they form, AIM will quantify the connection between these clouds and the meteorology of the polar mesosphere. In the end, this will provide the basis for study of long term variability in the mesospheric climate and its relationship to global change. The comparison of AIM mission science data and PMSE heating experiment results provide information about the microaeronomy of dust clouds in polar mesosphere, and eventually help to understand the formation of polar mesosphere clouds and the generation of PMSE.

The physics of radar scatter from charged particulates in the upper atmosphere will be studied with the Charged Aerosol Release Experiment (CARE). In 2008, two rocket payloads are being designed for launch North America. The purpose of the CARE program is to identify the mechanisms for radar scatter from polar mesospheric clouds. Some fundamental questions that remain about the scatting process are: (1) What is the relative importance of turbulent scatter versus incoherent (i.e., Thompson) scatter from individual electrons? (2) What produces the inhomogeneous electron/dust plasma? (3) How is the radar scatter influenced by the density of background electrons, plasma instabilities and turbulence, and photo detachment of electrons from the particulates? These questions will be addressed when the CARE program releases 50 kg of dust particles in an expanding shell at about 300 km altitude. The dust will be manufactured by the chemical release payload to provide particulate sizes in the 10 to 1000 nm range. The expanding dust shell will collect electrons making dense, heavy particles the move the negative charges across magnetic field lines. Plasma turbulence and electron acceleration will be formed from the charge separation between the magnetized oxygen ions in the background ionosphere and the streaming negatively charged dust. Future theocratical and computation model could be used to estimate the plasma structure which can scatter radar. The radar scatter form this artificial layer will be compared with natural PMSE observations.

Appendix A

Appendix A: Numerical Methods

In chapter 3, the physical model was introduced. Here in this section, numerical techniques will be discussed. In this numerical model, electrons and ions are treated as a fluid, and dust is treated as particle. Methods for both particles and fluid will be described respectively.

A.1 Method for particles

The Particle In Cell method is used in this work for the calculations of dust particles. The PIC technique is an efficient and conceptually simple method of solving a wide variety of complex problems involving a large number of particles moving under the action of self-generated and externally imposed forces. It has been used for over several decades in many fields and in particular in plasma physics. The defining characteristic of PIC simulations is the method of calculating the force acting on each particle. The simulation region is divided into a number of cells and the resulting grid is used in the solution of a field equation from which the force on each particle can then be determined. The relevant field equation is then Poisson's equation or current closure equation in one dimension. The complete algorithm involves four basic steps:

- Calculate the charge density on the grid from the present particle positions.
- Calculate the electrostatic potential and electrostatic field.
- Interpolate the electric field from the grid points to the individual particle positions.
- Integrate the equation of motion for each particle to obtain the new position and velocity.

The method of charge assignment is important in determining the computational speed and the accuracy. In our simulation we assign part of the charge to each of the two nearest grid points so that the particles are effectively finite-width sheets of charge. This scheme improves accuracy by smoothing the charge density and thus reducing fluctuations that arise from the discrete nature of the simulation. The interpolation of the electric field is symmetric with the charge assignment (i.e., linear interpolation from the two nearest values) so that problems due to particle self-force are avoided.

The dust position $\vec{x}_{\mathrm{j}}$ and velocity $\vec{v}_{\mathrm{j}}$ are advanced as follows

$$\frac{d\vec{v}_{\mathrm{j}}}{dt} = \frac{Q_{\mathrm{j}}(t)}{m_{\mathrm{j}}}\vec{E}, \tag{A.1}$$

$$\frac{d\vec{x}_{\mathrm{j}}}{dt} = \vec{v}_{\mathrm{j}}, \tag{A.2}$$

where m_{j} is the mass and $Q_{\mathrm{j}}(t)$ is the time dependent charge for the j^{th} dust grain. Note that dust motion dynamics are included in this model. The standard dust charging model is used. For the j^{th} dust grain this becomes:

$$\frac{dQ_{\mathrm{j}}}{dt} = I_{\mathrm{e}j} + I_{\mathrm{i}j}, \tag{A.3}$$

where $I_{\mathrm{e}j}$, $I_{\mathrm{i}j}$ are electron and ion currents collected by the dust grains. The electron and ion currents on the j^{th} dust grain are given by

$$I_{\mathrm{e}j} = \pi {r_d}^2 \left(\frac{8}{\pi}\right)^{1/2} q_{\mathrm{e}} n_{\mathrm{e}} v_{\mathrm{te}} \exp\left[\frac{e\phi_{\mathrm{fj}}}{kT_{\mathrm{e}}}\right], \tag{A.4}$$

$$I_{\mathrm{i}j} = \pi {r_d}^2 \left(\frac{8}{\pi}\right)^{1/2} q_{\mathrm{i}} n_{\mathrm{i}} v_{\mathrm{ti}} \left[1 - \frac{e\phi_{\mathrm{fj}}}{kT_{\mathrm{i}}}\right], \tag{A.5}$$

where r_d is the grain radius, $n_{\mathrm{e,i}}$ are electron and ion densities at the dust grain location, $v_{\mathrm{te,i}}$ are the electron and ion thermal velocity, $T_{\mathrm{e,i}}$ are the electron and ion temperatures, and ϕ_{fj} is the floating potential on the dust grain given by

$$\phi_{\mathrm{fj}} = \frac{Q_{\mathrm{j}}(t)}{C} = \frac{Q_{\mathrm{j}}(t)}{4\pi\epsilon_0 r_d}, \tag{A.6}$$

where C is the grain capacitance. Since for the case of interest, the electron gyroradius is assumed larger than the dust grain size, the standard dust charging model, which does not include magnetic field effects, is valid.

The equation of motion is integrated using the leapfrog method

$$v_{\mathrm{t}+(1/2)} = v_{\mathrm{t}-(1/2)} + \frac{e_{\mathrm{s}}}{m_{\mathrm{s}}} E_{\mathrm{t}} dt \tag{A.7}$$

$$x_{\mathrm{t}+1} = x_{\mathrm{t}} + v_{\mathrm{t}+(1/2)} dt \tag{A.8}$$

where x and v, are the particle position and velocity and E_{t} is the field at time t, so that velocity and position are determined at alternate half-integral time steps.

Charging equation 8.3 is solved using the predictor-corrector method (Section A.2) as below:

$$step1 : Q^{\dagger} = Q^{t} + \ dt \cdot (I_{\mathrm{i}}^{t} + I_{\mathrm{e}}^{t}) \tag{A.9}$$

$$step2 : I_{\mathrm{i}}^{t+\frac{dt}{2}} + I_{\mathrm{e}}^{t+\frac{dt}{2}} = \frac{1}{2}((I_{\mathrm{i}}^{t} + I_{\mathrm{e}}^{t}) + (I_{\mathrm{i}}^{\dagger} + I_{\mathrm{e}}^{\dagger})) \tag{A.10}$$

$$step3 : Q^{t+dt} = Q^{t} + \ dt \cdot (I_{\mathrm{i}}^{t+\frac{dt}{2}} + I_{\mathrm{e}}^{t+\frac{dt}{2}}) \tag{A.11}$$

A.2 Method for fluid

Typically, electrical field is derived from electrical potential, which will be solved by Poisson's equation [*Birdshall and Langdon,* 1991]. However, in this work, the electrostatic filed is calculated simply from the current closure equation:

$$\bigtriangledown \cdot \vec{J} = 0, \tag{A.12}$$

In one dimensional model, this could be simplified as:

$$\frac{dJ}{dx} = 0, \tag{A.13}$$

using the assumption of $m_{\mathrm{d}} \gg m_{\mathrm{i}} \gg m_{\mathrm{e}}$, A.14 could be expressed as:

$$J_{\mathrm{T}} = q_{\mathrm{e}} n_{\mathrm{e}} \mathbf{v}_{\mathrm{e}} + q_{\mathrm{i}} n_{\mathrm{i}} \mathbf{v}_{\mathrm{i}} + J_{\mathrm{d}} = 0 \tag{A.14}$$

This method is often used in ionospheric plasmas. [*Hill*, 1978], where J_{T} is the total current density of ions, electrons and dust, where J_{d} is the dust current density calculated from the simulation dust particles. Substituting the previous expressions for the electron and ion velocities into equation (3.11), the electrostatic field can be calculated as

$$E = \frac{\left(\frac{q_{\mathrm{e}} K T_{\mathrm{e}}}{m_{\mathrm{e}} \nu_{\mathrm{en}}} \frac{\partial n_{\mathrm{e}}}{\partial x} + \frac{q_{\mathrm{i}} K T_{\mathrm{i}}}{m_{\mathrm{i}} \nu_{\mathrm{in}}} \frac{\partial n_{\mathrm{i}}}{\partial x} - J_{\mathrm{d}}\right)}{\left(\frac{q_{\mathrm{e}}^2}{m_{\mathrm{e}} \nu_{\mathrm{en}}} n_{\mathrm{e}} + \frac{q_{\mathrm{i}}^2}{m_{\mathrm{i}} \nu_{\mathrm{in}}} n_{\mathrm{i}}\right)}. \tag{A.15}$$

Applying finite difference method to A.15, the electrical field at each point could be calculated as:

$$E_k = \frac{\left(\frac{q_{\mathrm{e}} K T_{\mathrm{e}}}{m_{\mathrm{e}} \nu_{\mathrm{en}}} \frac{n_{\mathrm{ek}+1} - n_{\mathrm{ek}-1}}{2dx} + \frac{q_{\mathrm{i}} K T_{\mathrm{i}}}{m_{\mathrm{i}} \nu_{\mathrm{in}}} \frac{n_{\mathrm{ik}+1} - n_{\mathrm{ik}-1}}{2dx} - J_{\mathrm{dk}}\right)}{\left(\frac{q_{\mathrm{e}}^2}{m_{\mathrm{e}} \nu_{\mathrm{en}}} n_{\mathrm{ek}} + \frac{q_{\mathrm{i}}^2}{m_{\mathrm{i}} \nu_{\mathrm{in}}} n_{\mathrm{ik}}\right)}. \tag{A.16}$$

Practical simulations must be scaled to eliminate unnecessary arithmetic operations and, most importantly, to reduce the number of particles in the simulation. The scaling is completely internal to our simulation and all output is in SI units.

In this work, the predictor-corrector method [*Shampine, 1994*]is used to solve the temporal dependent of our theoretical fluid model. A Predictor-corrector method is a combination of an explicit predictor formula and an implicit corrector formula. Predictor-corrector methods store the solution along the way, and use those results to extrapolate the solution one step advanced. They then correct the extrapolation using derivative information at the new point. Predictor-corrector methods have good stability properties and are best for smooth functions. Consider the following ODE

$$\frac{dn}{dt} = f(n, t) \tag{A.17}$$

where $f(n, t)$ is represented in the spectral domain. The predictor-corrector method is as follows

$$step1 : n^{\dagger} = n^t + \ dt \cdot f(n^t, t) \tag{A.18}$$

$$step2 : f(n^*, t + \frac{dt}{2}) = \frac{1}{2}(f(n^t, t) + f(n^{\dagger}, t + dt)) \tag{A.19}$$

$$step3 : n^{t+dt} = n^t + \ dt \cdot f(n^*, t + \frac{dt}{2}) \tag{A.20}$$

where † is the estimate of any quantity at $t + dt$ and dt is the time step.

Therefore, recall $n_i = n_e$ for the quasi-neutrality, the continuity equation for ions could be solved using this method.

$$\frac{\partial n_{\mathrm{i}}}{\partial t} + \frac{\partial F_{\mathrm{i}}}{\partial x} = S \tag{A.21}$$

here, $S = P_{\mathrm{i}} + L_{\mathrm{i}} + \frac{\mathrm{d}n_{\mathrm{i}}}{\mathrm{dt}}|_{\mathrm{charging}}$ means the source of ion charge fluctuation. $F_i = n_i v_i$ is the ion flux, and v_i (Equation 3.2) is the ion velocity. Applying simple finite difference method, the ion flux at point k will be expressed as:

$$F_{ik} = \frac{n_{ik}}{\nu_{in}} \left(\frac{q_i}{m_i} E_k - \frac{KT_i}{m_i} \frac{\log\left(n_{ik+1}\right) - \log\left(n_{ik-1}\right)}{2dx} \right) \tag{A.22}$$

Following the algorithm described above, the predictor-corrector method could be achieve as:

step 1 :

$$n_{ik}^{\dagger} = n_{ik}^{t} + \ dt \cdot ((\frac{F_{ik+1}^{t} - F_{ik-1}^{t}}{2dx}) + S_{ik}^{t}) \tag{A.23}$$

step 2 :

$$(\frac{F_{ik+1}}{t + \frac{dt}{2} - F_{ik-1}^{t+\frac{dt}{2}}} 2dx) + S_{ik}^{t+\frac{dt}{2}}) = \frac{1}{2}(((\frac{F_{ik+1}^{t} - F_{ik-1}^{t}}{2dx}) + S_{ik}^{t}) + ((\frac{F_{ik+1}^{\dagger} - F_{ik-1}^{\dagger}}{2dx}) + S_{ik}^{\dagger}))\tag{A.24}$$

step 3 :

$$n^{t+dt} = n^{t} + \ dt \cdot ((\frac{F_{ik+1}^{t+\frac{dt}{2}} - F_{ik-1}^{t+\frac{dt}{2}}}{2dx}) + S_{ik}^{t+\frac{dt}{2}}) \tag{A.25}$$

Appendix B

Appendix B: Charging Models Comparison

When a dust particle is immersed in a plasma, it will be gradually charged up by collecting electron and ion currents. In previous works [*Chen and Scales* 2005; *Scales,* 2004], the dust charge is determined from the standard continuous charging model which is given by [*Shukla and Manun,* 2002]

$$\frac{dQ_{\mathrm{d}}}{dt} = I_{\mathrm{e}} + I_{\mathrm{i}} \tag{B.1}$$

where I_{e} and I_{i} are the currents onto each individual dust particle by electron and ion flux. Note photoemission and other charging currents have been neglected [*Havnes et al.,* 2003].

In chapter 3, the discrete charging model was introduced. In that model, the traditional OML charging model is applied. Here in this section, another two charging models will be presented and compared with OML charging model.

B.1 OML Charging Model

We start from the standard OML charging model [*Bernstein and Rabinowitz,* 1959]. The temporal evolution of the charge $Q_{\mathrm{d}}(t)$ can be found by integrating (8.23), using suitable expressions for the currents I_α, where $\alpha = e$ or i. For negatively charged dust, which will primarily be considered, these currents are given by

$$I_{\mathrm{e}} = \sqrt{8\pi} r_{\mathrm{d}}^2 q_{\mathrm{e}} n_{\mathrm{e}} v_{\mathrm{te}} \exp(-q_{\mathrm{e}}\phi_{\mathrm{d}}/KT_{\mathrm{e}}) \tag{B.2}$$

$$I_{\mathrm{i}} = \sqrt{8\pi} r_{\mathrm{d}}^2 q_{\mathrm{i}} n_{\mathrm{i}} v_{\mathrm{ti}} (1 - q_{\mathrm{i}}\phi_{\mathrm{d}}/KT_{\mathrm{i}}). \tag{B.3}$$

It should be noted that the model here represents the simplest model for dust charging and it has been extensively used in the past to study waves and instabilities in dusty plasmas. More sophisticated models exist and currently charging is a topic of considerable interest in dusty plasma physics. It has recently been shown that the standard model does not provide the most accurate description of dust charging in the regime $d \leq \lambda_{\mathrm{D}}$. This is the regime in which the collective effects discussed here occur. However, we believe the standard model will provide a reasonable description for the physical processes investigated in this study.

B.2 Drain and Sutin Collisional Charging Model

The second charging model comes from [*Drain and Sutin,* 1987]. Let I_α be the charging current with density n_α, charge q_α, mass m_α, and sticking coefficient s_α at the grain surface, where α = e or i. And define r_d as the dust radii, Z_d as the charge number on the dust. If the charged particles have a Maxwellian distribution at infinity, then

$$I_\alpha = n_\alpha s_\alpha (\frac{8kT}{\pi m_\alpha})^{1/2} \pi {r_d}^2 \tilde{I}(\tilde{T}, Z_d) \tag{B.4}$$

where $\tilde{T}$ is the 'reduced temperature':

$$\tilde{T} = r_d kT/{q_i}^2 \tag{B.5}$$

Also,

$$\tilde{I}(\tilde{T}, Z_d) = \int_0^\infty x e^{-x} \tilde{\sigma} dx \tag{B.6}$$

here, $\tilde{\sigma}$ is the cross section. For the spacial case, $Z_d = 0$ (i.e, neutral grain), it yields the simple result:

$$\tilde{I}(\tilde{T}, Z_d = 0) = 1 + (\frac{\pi}{2\tilde{T}})^{1/2} \tag{B.7}$$

For the case of $Z_d < 0$ (attractive Coulomb potential at large distances), the form could be simplified as:

$$\tilde{I}(\tilde{T}, Z_d < 0) \approx [1 - \frac{Z_d}{\tilde{T}}][1 + (\frac{2}{\tilde{T} - 2Z_d})^{1/2}] \tag{B.8}$$

For $Z_d > 0$ (repulsive long-range Coulomb interaction), a simple formula for $\tilde{I}$ is:

$$\tilde{I}(\tilde{T}, Z_d > 0) \approx [1 + (4\tilde{T} + 3Z_d)^{-1/2}]^2 \exp(-\theta_Z/\tilde{T}) \tag{B.9}$$

where θ_Z is a dimensionless measure of the value of the potential maximum. It equals to 0 for $Z_d \leq 0$, and $\theta_Z \approx \frac{Z_d}{1+Z_d^{-1/2}}$ otherwise. This formula is accurate within 0.7% for $1 \leq Z_d < \infty$.

B.3 Natanson Charging Model

The third charging model is derived from [*Natanson*, 1960] (see also Lie-Svendsen, 2003).

Firstly, the reaction rates for capturing electrons and ions by dust particles could be represented as follows:

$$\psi_{e,0} = \pi {r_d}^2 c_e (1 + \sqrt{\frac{e^2}{8\epsilon_0 kTr_d}}) \tag{B.10}$$

$$\psi_{i,0} = \pi {r_d}^2 c_i (1 + \sqrt{\frac{e^2}{8\epsilon_0 kTr_d}}) \tag{B.11}$$

$$\psi_{e,q>0} = \pi {r_d}^2 c_e (1 + \frac{qe^2}{4\pi\epsilon_0 kTr_d}) \tag{B.12}$$

$$\psi_{e,q<0} = \pi {r_d}^2 c_e \exp\,[-\frac{|q|e^2}{4\pi\epsilon_0 kTr_d\gamma}(1 - \frac{1}{2\gamma(\gamma^2-1)|q|})] \tag{B.13}$$

$$\psi_{i,q<0} = \pi {r_d}^2 c_i (1 + \frac{qe^2}{4\pi\epsilon_0 kTr_d}) \tag{B.14}$$

Here k and ϵ_0 denote Boltzmann's constant and the permittivity of vacuum. The dust charge in units of the elementary charge e is denoted by q, the two subscripts denotes electrons and ions which is being attached to the dust particles. Therefore, $\psi_{e,0}$ is the rate for capture of electrons by neutral particles, $\psi_{e,q<0}$ is the rate for capture of ions by a particle with negative charge $q = -|q|$ etc. Furthermore, r_d is the dust particle radius; $c_{i,e} \equiv \sqrt{8kT/(\pi m_{i,e})}$ is the mean thermal speed of ions or electrons; and γr_d is the critical distance at which the induced attractive (dipole) force is stronger than the Coulomb repulsive force of the dust particle. The relation between a negative dust charge $q = -|q|$ and γ is given by [*Natanson*, 1960]

$$-q = \frac{2\gamma^2 - 1}{\gamma(\gamma^2-1)^2} \tag{B.15}$$

with the numerical solution raging from $\gamma = 1.62$ for $q = -1$ to $\gamma = 1.22$ for the highest charge state of the model, $q = -q_{max} = -7$.

For dust particles with charge $-q_{max} < q < 1$, the charging current is (α = i or e):

$$I_\alpha = \psi_{e,q+1} n_e n_{\alpha,q+1} + \psi_{e,q-1} n_e n_{\alpha,q-1} \tag{B.16}$$

for positively charged dust particles, the current is:

$$I_\alpha = \psi_{i,0} n_i n_{\alpha,0} \tag{B.17}$$

and for dust particles with the maximum charge, $q = -q_max$,

$$I_\alpha = \psi_{e,q+1} n_e n_{\alpha,q+1} \tag{B.18}$$

B.4 Charging Model Comparison

These three different charging models have their own advantages but also the limitations. Figure B.1 shows the charging rate comparison of all three models. The charging rate is defined as:

$$f_c = 1/\tau_c = (I_e + I_i)/e \tag{B.19}$$

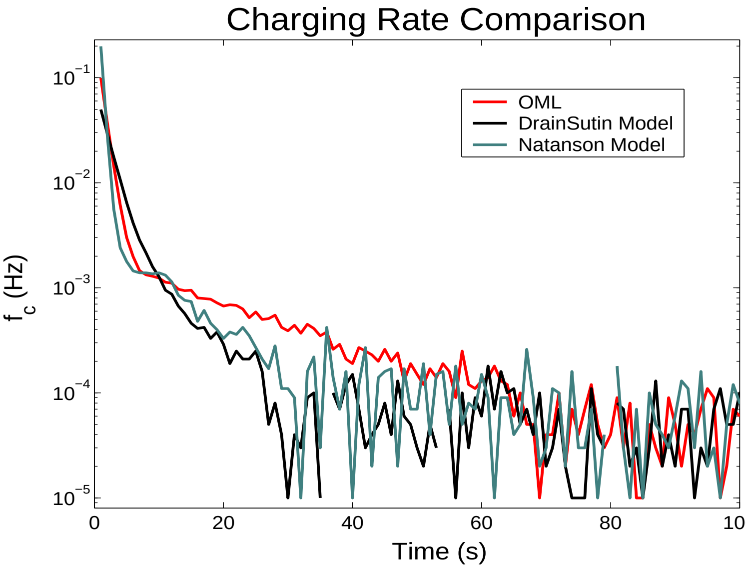

Figure B.1: The charging rate comparison of three different charging models.

In this case, the dust density is 1% of the initial plasma density, i.e., $n_{d0}/n_0 = 0.01$ and the wavelength is $\lambda = 4$ m ($f = 30$ MHz), dust radius $r_d = 10$ nm. The simulation runs for 100 seconds to guarantee that the electron and ion densities reach equilibrium. It is noted that this charging rate is proportional to the charging current which is described in the previous sections. From the curves, the three models are reasonably close to each other. The OML model decreased slightly faster comparing with the other two models. All three models reach a close agreement at the equilibrium.

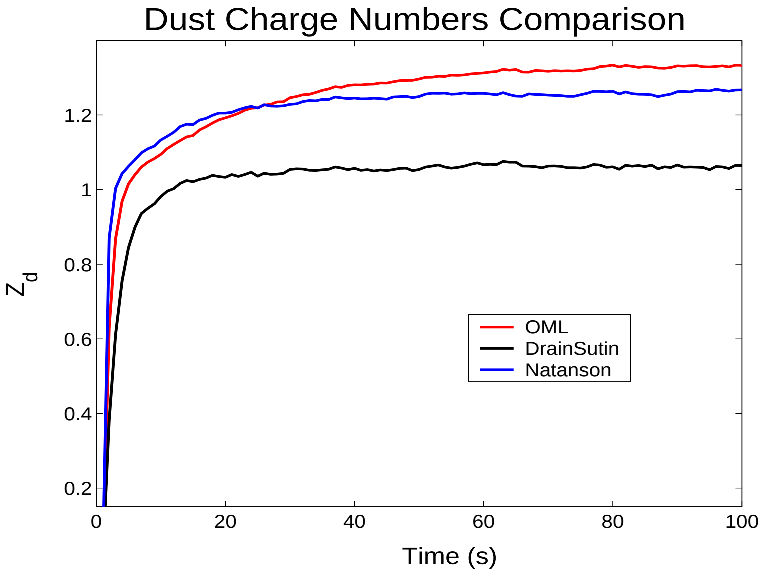

Figure B.2: The comparison of average charge numbers on dust particles.

Figure 8.2 shows the average charge numbers on each dust particles using the same physical parameters in figure 8.1. The results are slightly different from each other. At equilibrium, OML charging model has averagely about 1.3 electrons on each dust particles; while 1.2 and 1 electrons for Natanson model and DrainSutin model respectively. Figure 8.3 shows the temporal evolution of the electron irregularity amplitude for each model. All three show relatively close profiles during the whole simulation. They all reached similar values at the equilibrium.

From all above, these three charging models show very similar behavior for the single dust particle charging process. They are supplementary to each other in different physical conditions. The purpose of this comparison is find a more accurate charging model for the PMSE research. Extensive experimental observation should be operated to provide sufficient results for further conclusion.

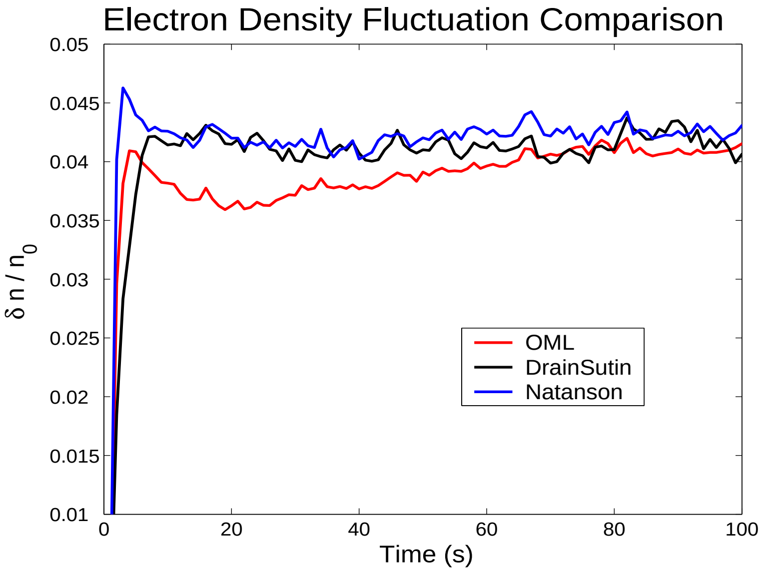

Figure B.3: Time evolution of electron density irregularities with different charging models.

Reference

Banks, P.M., and Kockarts, G., *Aeronomy*, Academic Press, New York, 1973.

Belova, E., P.B. Chilson, M. Rapp, and M.T. Rietveld, The response time of PMSE to ionospheric heating, *Journal of Geophysic Research* 108 (D8), 8446, 2003.

Bernstein, I.B. and I.N. Rabinowitz, Theory of electrostatic probes in a low density plasma, *Phys. Fluids, 2*, 112-121, 1959.

A. Biebricher, O. Havnes, T.W. Hartquist and C. LaHoz, On the influence of plasma absorption by dust on the PMSE overshoot effect, *Advances in Space Research,* Volume 38, Issue 11, p. 2541-2550, 2005

Birdsall C.K. and A.B. Langdon, *P*lasma Physics via Computer Simulation, New York, McGraw-Hill, 1991.

Chen, C., Scales, W.A. Electron temperature enhancement effects on plasma irregularities associated with charged dust in the Earth's mesosphere, J. Geophys. Res., 110, doi:10.1029/2005JA011341, 2005.

Chen, C., Scales, W.A. Active perturbation of dust associated electron irregularities in the Earth's mesosphere: Discrete charging effects, IEEE Trans. Plasma Sci., 35, 731-735, doi:10.1109/TPS.2007.895228, 2007.

Chen, F.F., Introduction to Plasma Physics and Controlled Fusioin, Plenum Press, New York, 1985.

Chilson, P.B., E. Belova, M.T. Rietveld, S. Kirkwood, and U. Hoppe, First artificially induced modulation of PMSE using the EISCAT heating facility, *Geophysic Research Letter*,27, 3801-3804, 2000.

Cho, J.Y.N., T.M. Hall, and M.C. Kelley, On the role of charged aerosols in polar mesospheric summer echoes, *Journal of Geophysic Research*, 97, 875-886, 1992.

Cho, J.Y.N and M.C. Kelley, Polar mesospheric summer radar echoes: Observations and current theories, *R*eviews of Geophysics, 31, 243-265, 1993.

Cho, J.Y.N and J. Rottger, An updated review of polar mesospheric summer echoes; Observation, theory, and their relationship to noctilucent clouds and subvisible aerosols, *Journal of Geophysic Research*, 102, 2001-2020, 1997.

Cui, C. and J. Goree, Fluctuations of the charge on a dust grain in a plasma, *IEEE Trans. Plasma Sci., 22*, 151-158, 1994.

D'Angelo, N., Ion and Dust Acoustic Waves in Polar Mesospheric Summer Echoes, *Physics Letters A.*, in press 2005

Dimant, Y.S. and G. M. Milikh, Effect of radio wave heating on polar mesospheric clouds, *A*dv. Space Res. 2003.

Draine, B. T., and Sutin, B. Collisional charging of interstellar grains, *Astrophys. J., 320*, 803-817, 1987.

Eklund, W.L. and B.B. Balsley, Long-term observations of the Artic mesophere with MST radar at Poker Flat, Alaska, *Journal of Geophysic Research*, *8t,* 7775, 1981.

Gadsden, A secular change in noctilucent cloud occurrence *Journal of Atmospheric and Terrestrial Physics*, vol 52, p247, 1990

Gurevich, A.V., Nonlinear Phenomena in the Ionosphere, New York, Springer-Verlag, 1978.

Hastings, J. T. and Roble, R. G., An automatic technique for solving coupled vector systems of non-linear parabolic partial differential equations in one space dimension, /it Planetary and Space Science, Volume 25, Issue 3, p. 209-215

Havnes, O., G.E. Morfill, and C.K. Goertz, Plasma potential and grain charges in a dust cloud embedded in a plasma, *Journal of Geophysic Research* 89, 10999-11003, 1984.

Havnes, O., T.K. Aanesen, and F. Melandso, On dust charges and plasma potentials in a dusty plasma with dust size distribution, *Journal of Geophysic Research*, 95, 6581-6585, 1990.

Havnes, O., J. Troim, T. Blix, W. Mortensen, L.I Naesheim, E. Thrane, and T. Tonnesen, First detection of charged dust particles in the earth's mesosphere, *Journal of Geophysic Research*, 101, 10839-10847, 1996.

Havnes, O., C. La Hoz, and L.L. Naesheim, First Observations of the PMSE overshoot effect and its use for investigating the conditions in the summer mesosphere, *Geophysic Research Letter*, 30, NO.23,2229, 2003.

Havnes, O., Polar mesospheric Summer Echoes(PMSE) overshoot effect due to cycling of artificial electron heating, *Journal of Geophysic Research*, 109, A02309, 2004.

Hill, R. J., Nonneutral and quasi-neutral diffusion of weakly ionized multiconstituent plasma, *Journal of Geophysic Research*, 83, 989-998, 1978.

Hocking, W. K., Radar studies of small scale structure in the upper middle atmosphere and lower ionosphere, *Adv. Space Res.*, 7(10), 327-338, 1987.

Houpis,H.L., and Whipple, E.C., Electrostatic charge on a dust size distribution in a plasma, *Journal of Geophysic Research*, 92, 12,057-12,068, 1987

Karashtin, A. N., Y. V. Shlyugaev, V. I. Abramov, I. F. Belov, I. V. Berezin, V. V. Bychkov, E. B. Eryshev, and G. P. Komrakov, First HF radar measurements of summer mesopause echoes at SURA, *Ann. Geophys.,* 15, 935C 941, 1997

Kelley, M.C., Huaman, M., Chen, C., Ramos, C., Djuth, F., Kennedy, E., Polar mesosphere summer echo observations at HF frequencies using the HAARP Gakona Ionospheric Observatory, *Geophysical Research Lett.*, VOL. 29, NO. 12, 1603, 10.1029/2001GL013411, 2002

Kelley, M., and J. Ulwick, Large- and small-scale organization of electrons in the highlatitude mesosphere: Implications of the STATE data, *J. Geophys. Res.,* 93, 7001-7008, 1988.

Lee, C. C., J. Y. Liu, C. J. Pan, and C. H. Liu, Doppler velocities obtained by the EISCAT VHF radar and the dynasonde during the PMSE95 campaign, *J. Atmos. Solar-Terr. Phys.,* 63(2C 3), 193C199, 2001

Lie-Svenson, O., T.A. Blix, and U.P. Hoppe, Modeling the plasma response to small-scale aerosol particle perturbations in the mesopause region, *Journal of Geophysic Research*, 108, 2753-2777, 2003.

Milikh, G. M., M. J. Freeman, and L.M. Duncan, First estimates of HF-induced modifications of the D region by the HF active auroral research program facility, *Radio Science, 29*, 1355-1362, 1994.

Natanson, G.L., On the theory of the charging of amicroscopic aerosol particles as a result of the capture of gas ions, *Sov. Phys. Tech. Phys. Engl. Transl., 5*, 538-551, 1960.

Rapp, M. and F.-J. Lubken, Electron temperature control of PMSE, *Geophysic Research Letter*, 27, 3285-3288, 2000.

Rapp, M. and F.-J. Lubken, Modelling of particle charging in the polar summer mesosphere: Part 1 - General results, J. Atmos. Terr. Phys., 63, 759-770, 2001.

Rapp, M., J.-F. Lubken, On the nature of PMSE:, Electron diffusion in the vicinity of charged paricles revisited, *Journal of Geophysic Research*, 108, 2857-2870, 2003.

Rottger, J., C. La Hoz, M. C. Kelley, U. P. Hoppe, and C. Hall, The structure and dynamics of polar mesosphere summer echoes observed with the EISCAT 224-MHz radar, *Geophys. Res. Lett.,* 15, 1353C 1356, 1988.

Rottger, J., M. T. Rietveld, C. La Hoz, T. Hall, M. C. Kelley, and W. E. Swartz, Polar mesosphere summer echoes observed with the EISCAT 933-MHz radar and the CUPRI 46.9-MHz radar, their similarity to 224-MHz radar echoes and their relationship to turbulence and electron density profiles, *Radio Sci.,* 25, 671C 687, 1990.

Royrvik, O. and L.G. Smith, Comparison of mesospheric VHF radar echoes and rocket probe electron concentration measurements, *Journal of Geophysic Research*, 89, 9014, 1984.

Shukla, P.K. and A.A. Mamun, *Introduction to Dusty Plasma Physics*, Philadelphia, Institute of Physics, 2002.

Scales, W.A, Myers, T.J., Bernhardt, P.A, and Ganguli, G. Attachement rate effects during electron attachment chemical releases, *Journal of Geophysic Research*, 102, 9767-9771, 1997.

Scales, W. and C. Chen, On the initial perturbation of mesospheric dust associated irregularities by high power radio waves, *Adv. Space Res.*, doi:10.1016/ j.asr.2007.08.009, 2007(a).

Scales, W. and C. Chen, On the initial enhancement of mesospheric dust associated irregularities subsequent to radio wave heating, *Annales Geophysicase.*, 2007(b).

Scales, W. Electron Temperature effects on Small-Scale Plasma Irregularities Associated With Charged Dust in the earth's Mesosphere, *IEEE Trans. Plamsa Sci., 32*,724, 2004.

Ulwick J. C., Baker K., Kelley M. C., Balsley B., and W. Ecklund, Comparison of simultaneous MST radar and electron density probe measurements during STATE, *J. Geophys. Res.,* 93, 6989-7000, 1988. D

Winske, D. and M. Rosenberg, Nonlinear development of the dust acoustic instability in a collisional dusty plasma, *IEEE Trans. Plasma Sci., 26*, 92, 1998.

VITA

Chen Chen was born in Chengdu, Sichuan, P.R.China in 1979. His father, Bi Chen, is a historian and his mother, Xiaofen Wang, was a government officer. Chen is the only child in his family.

Chen spent most of his childhood and youth in Chengdu. After graduated from University of Electronic Science and Technology of China, where he studied electrical engineering and computer engineering, he moved to Singapore, to attend a joint program between MIT and National University of Singapore. He graduated 2003 with a master in computational engineering.

In August 2003, Chen moved to Blacksburg, Virginia, entered Virginia Tech as a graduate student. There he met an intelligent and vivacious young woman, Wei Jin. After four and a half years and many trials and tribulations, he graduated with a Ph.D in dusty plasma physics.

Chen is planning moving to Greensboro, NC as a senior system verification engineer at RFMD Inc.. In the meanwhile, Chen will keep doing his space science research as a hobby.